HIGH VELOCITY INTERCEPTOR INVESTIGATIONS

FINAL REPORT

HARTMUT H. LEGNER, ALAN H. GELB, DAVID I. ROSEN,
AND GEORGE E. CALEDONIA

SEPTEMBER 1998

U.S. ARMY RESEARCH OFFICE
P.O. BOX 12211
RESEARCH TRIANGLE PARK, NC 27709

DAAH04-95-C-0056

PHYSICAL SCIENCES
20 NEW ENGLAND BUSINESS CENTER
ANDOVER, MA 01810

APPROVED FOR PUBLIC RELEASE

DISTRIBUTION UNLIMITED

19981222 066

PSI

PHYSICAL SCIENCES INC.

REPORT DOCUMENTATION PAGE

Form Approved
OMB No. 0704-0188

1. AGENCY USE ONLY (Leave blank)	2. REPORT DATE September 1998	3. REPORT TYPE AND DATES COVERED Final Report, 1 Aug. 95 - 31 July 98

4. TITLE AND SUBTITLE

High Velocity Interceptor Investigations

5. FUNDING NUMBERS

DAAH04-95-C-0056

6. AUTHOR(S)

Hartmut H. Legner, Alan H. Gelb, David I. Rosen, and George E. Caledonia

7. PERFORMING ORGANIZATION NAME(S) AND ADDRESS(ES)

Physical Sciences Inc.
20 New England Business Center
Andover, MA 01810

8. PERFORMING ORGANIZATION REPORT NUMBER

PSI-1239/TR-1573

9. SPONSORING/MONITORING AGENCY NAME(S) AND ADDRESS(ES)

U.S. Army Research Office
P.O. Box 12211
Research Triangle Park, NC 27709-2211

10. SPONSORING/MONITORING AGENCY REPORT NUMBER

ARO 34826.1-EG-SDI

11. SUPPLEMENTARY NOTES

This material is based upon work supported by the U.S. Army Research Office under Contract DAAH04-95-C-0056. Any opinions, findings, and conclusions or recommendations expressed in this material are those of the author(s) and do not necessarily reflect the views of the U.S. Army Research Office.

12a. DISTRIBUTION/AVAILABILITY STATEMENT

Approved for public release; distribution unlimited

12b. DISTRIBUTION CODE

13. ABSTRACT (Maximum 200 words)

High velocity interceptors operating at low altitudes in the range from ~20 to 30 km will experience a stressing aerothermal environment which can impact performance of the infrared sensor/designator system. This report addresses primarily two aspects of high velocity interceptors: a novel passively cooled window concept and the control of boundary layer transition to turbulence. A totally new concept for maintaining the IR transmitting window of an interceptor at low temperature so as to minimize background interferences introduced by aerodynamic heating effects is described. The concept involves immersing a nest of fiber optics or bore-holes within a matrix of a low temperature pyrolysis material, a transition metal hydride. These hydrides have the ability to absorb heat at

14. SUBJECT TERMS

15. NUMBER OF PAGES

102

16. PRICE CODE

17. SECURITY CLASSIFICATION OF REPORT Unclassified	18. SECURITY CLASSIFICATION OF THIS PAGE Unclassified	19. SECURITY CLASSIFICATION OF ABSTRACT Unclassified	20. LIMITATION OF ABSTRACT Unlimited

CLASSIFIED BY:

DECLASSIFY ON:

13. ABSTRACT (Continued)

low temperatures through the desorption of H_2 molecules and thus behave like low temperature, high energy ablators. Thermal response calculations show that our window concept is viable.

The modeling of boundary-layer transition control over seeker windows under situations when the surface of the interceptor remains very cool during atmospheric flight is described. This occurs naturally for our "passive cool window" approach which employs a transition metal hydride to maintain window temperatures near 300 K at typical interceptor heating levels of several hundred watts per square centimeter. Such low surface temperatures provide a passive means of preventing boundary-layer transition from laminar to turbulent flow. A three-dimensional stability code was utilized to demonstrate that high-speed (Mach 15) boundary layers on typical seeker head geometries are stabilized by extreme wall cooling.

TABLE OF CONTENTS

TABLE OF CONTENTS (Continued)

LIST OF FIGURES

LIST OF FIGURES (Continued)

LIST OF FIGURES (Continued)

LIST OF FIGURES (Continued)

LIST OF FIGURES (Continued)

LIST OF TABLES

x

1. INTRODUCTION

High velocity interceptors operating at low altitudes in the range from ~20 to 30 km will experience a stressing aerothermal environment which can impact performance of the infrared sensor/designator system. This environment includes: high levels of aerothermal heating which can cause pyrolysis/ablation of nosecone/heatshield materials and affect window performance through undesirable temperature rise; flowfield IR background radiation produced by heated air and ablation species; and a turbulent flowfield which can provide optical distortions affecting the end-game target analysis.

Recently, there has also been a focus in the interceptor community to engage targets at even lower altitudes due to the proliferation of cruise missile and maneuvering threats. These engagement scenarios provide aerothermal environments that are even more severe than alluded to above. New window material technology and lightweight thermal protection material are required for these very low altitude interceptors. Furthermore, there is also current interest in developing passive seeker windows that do not require an external cooling flow to maintain satisfactory operating window temperatures.

This report addresses primarily two aspects of high velocity interceptors: a novel passively cooled window concept and the control of boundary layer transition to turbulence. In Section 2, a totally new concept for maintaining the IR transmitting window of an interceptor at low temperature so as to minimize background interferences introduced by aerodynamic heating effects is described. The concept involves immersing a nest of fiber optics within a matrix of a low temperature pyrolysis material, a transition metal hydride. These hydrides have the ability to absorb heat at low temperatures through the desorption of H_2 molecules, i.e.,

$$A_xB_{1-x} Hy \xrightarrow{heat} A_xB_{1-x} + v/2\ H_2$$
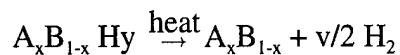
and thus behave like low temperature, high energy ablators. In addition, thermal response calculation of candidate hydride/thermal conductor material designs, scoping calculations for potential fiber temperatures and ablation rates for realistic aerodynamic heating rates and material properties are shown. These calculations show that our window concept is viable. In addition, a preliminary metal-hydride-bed window design using viewing parameters defined in the Atmospheric Interceptor Technology program was developed. We conclude that our optical train will have to be more complex than simple fiber optics in order to meet system field of view requirements.

In Section 3, our modeling of boundary-layer transition control over seeker windows under situations when the surface of the interceptor remains very cool during atmospheric flight is described. This situation occurs naturally for our "passive cool window" approach which employs a transition metal hydride to maintain window temperatures near 300 K at typical interceptor heating levels of several hundred watts per square centimeter. Such low surface temperatures provide a passive means of preventing boundary-layer transition from laminar to turbulent flow, but the synergistic solution is not universal since it depends critically on the local flow Mach number over the window. A three-dimensional stability code was utilized to

1

demonstrate that high-speed (Mach 15) boundary layers on typical seeker head geometries are stabilized by extreme wall cooling. The detailed laminar flow field computation over the wedge-like geometry for an advanced interceptor at 20 km was used as input into the stability code.

2. PASSIVE WINDOW COOLING TECHNIQUES

2.1 Background

An innovative passive window cooling technique using transition metal hydrides was studied. Our window cooling concept is defined by the use of the endothermic heat of decomposition of transition metal hydrides to remove aerodynamic heat loads.

Transition metal hydrides of the form $A_xB_{1-x}H_y$ are characterized by their rapid absorption and release of hydrogen via the equation:

$$A_xB_{1-x}H_y = A_xB_{1-x} + y/2H_2 \tag{1}$$
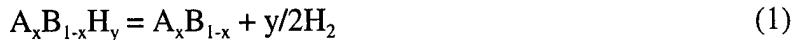
The release of hydrogen from these compounds has a high positive (exothermic) heat of reaction. Two examples of these reactions are:

$$LaNi_5H_6 \rightarrow LaNi_5 + 3 H_2 \qquad (\Delta H = 15.1 kJ/gmH_2) \tag{2}$$

$$(V_{0.89}Ti_{0.11})_{.95}Fe_{0.05}H_2 \rightarrow (V_{0.89}Ti_{0.11})_{.95}Fe_{0.05}H + 1/2H_2 \qquad (\Delta H = 21.5 \ kJ/gmH_2) \tag{3}$$
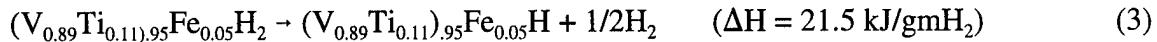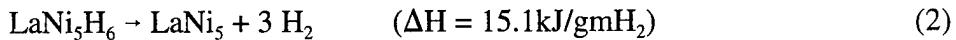
For these two compounds, the hydrogen pressure is greater than 1 atm at room temperature. Hence these compounds are quite unique in that they are low temperature, high energy ablators.

A schematic of the window cooling concept is presented in Figure 1. A porous bed of metal hydride surrounds optical fibers. The optical fibers provide optical access to detectors within the vehicle. Heat from aerodynamic heating is balanced by the heat of the metal hydride decomposition reaction. The decomposition reaction releases hydrogen into the boundary layer. The amount of hydrogen gas release from hydride is quite small because of the high endothermicity of the reaction. For example, for $(V_{0.89}T_{0.11})_{0.95}Fe_{0.05} H_2$, a 100 W/cm^2 aerodynamic heat load is balanced by a hydrogen production rate of 4.7 x 10^{-3} gm/cm^2/s.
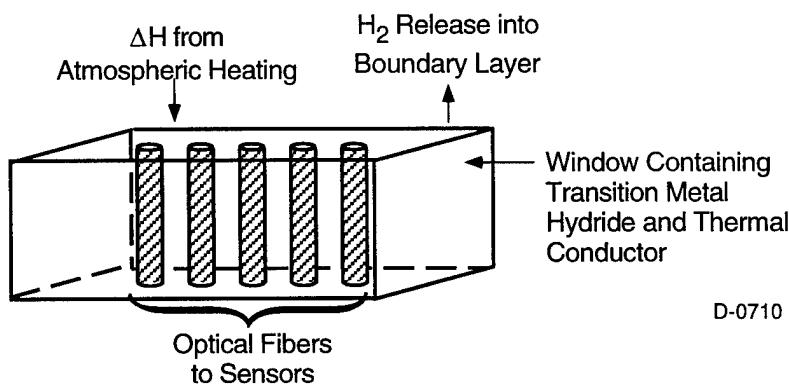
Figure 1. Schematic of Window Cooling Concept

We report here the results of a modeling effort to verify the feasibility of the transition metal hydride window cooling concept.

2.2 Aerothermal Environment and General Considerations

Figure 2 shows aerodynamic heat loads as a function of altitude for vehicle velocities between 3 and 5 km/s for a window placed on the vehicle.

The heating rates over the optical window are very high at low altitudes where turbulent flow prevails. As the altitude increases, the flow over the window becomes laminar and the heating rates decrease. This figure was obtained by taking the heating rate at 25 km and 4 km/s (see Ref. 2 in Section 3) and scaling it with $\rho_\infty V_\infty^3$ to the other conditions. Even though this approach is approximate, the results are representative of the local heating rates for a typical interceptor. Calculations for a different configuration provided similar heating levels as noted in Section 3. From the figure we can conclude that heating rates of 100 to 200 W/cm^2 are appropriate for the present interceptor application. Although these heating rates have been used as a guide for the assessment of passive window cooling problems, the window is capable of cooling effectively at higher heating loads as shown in subsequent calculations.

Figure 2. Heating rate, Q, versus Altitude, H, for Several Vehicle Velocities. Vehicle nose radius is 0.2 in. and cone angle is 15 deg.

The required depth, δ, of the hydride bed can be computed from energetic considerations. For an areal heating rate, Q (W/cm^2), over a period T, the bed depth required to balance the aerodynamic heat is

$$\delta = QT \left(\frac{MW}{\rho} \right)_{hydride} \frac{1}{\Delta H} \qquad (4)$$

where MW denotes the hydride molecular weight, ρ its density and ΔH is the enthalpy of the decomposition reaction. For a T=10 s and Q=100 W/cm^2, the respective bed depths for $LaNi_5H_6$ and $(V_{0.89}Ti_{0.11})_{.95}Fe_{0.05}H_2$ are 0.78 and 0.45 cm. The critical aspect of this quantity is that for the bed to effectively cool the outside surface, the aerodynamic heat flux must be transported the distance δ without significantly raising the surface temperature. The heat flux balance can be written as

4

$$Q = K \frac{T_s - T_d}{\delta} = K \frac{\Delta T}{\delta} \qquad (5)$$

where K is the bed thermal conductivity, T_s is the window surface temperature and T_d is a characteristic temperature for the hydride. Metal hydrides and the residual metals are not good thermal conductors. For illustrative purposes, we assume K = 0.1 to 0.5 W/cmK. For LaNi$_5$H$_6$ the predicted value of ΔT is in the range 156 to 780 deg. It is obviously desirable to reduce ΔT to as small a value as possible. Two strategies are obvious.

First, metal hydrides can be chosen with low values of $T_d \sim$ 200 to 250K. This implies that the window must be a pressurized vessel since the room temperature H$_2$ vapor pressure will be several atmospheres. Both LaNi$_5$H$_6$ and $(V_{0.89}Ti_{0.11})_{0.95}F_{0.05}H_2$ satisfy this criterion. Secondly, the hydride can be mixed with a high thermal conductor such as Cu or SiC to increase the bed conductivity. For example a 50/50 mixture Cu/LaNi$_5$H$_6$ with a thermal conductivity of approximately 2W/Kcm will have a value of $\Delta T = 39°C$ and a predicted surface temperature of about 280°C after 10 s of aerodynamic heating at 100 W/cm^2. Note that these calculations are quite conservative in that the evolved hydrogen enthalpy is neglected.

The dilution of the metal hydride bed leads to a trade off between the bed capacity and the thermal conductivity. Increased bed dilution decreases bed capacity and therefore increases the required thermal penetration depth δ. The optimization of materials constituents will be major consideration in the design of a robust optical window. In this study, we consider two metal hydrides: LaNi$_5$H$_6$ and $(V_{0.89}Ti_{0.11})_{0.95}Fe_{0.05}H_2$. Simulations were performed for mixtures of these hydrides with Cu metal to assess their response under realistic heating conditions.

2.3   Simple Kinetic Model for Hydrogen Production

We assume that the hydrogen pressure above the metal hydride is in equilibrium so that the hydrogen pressure is only a function of the local temperature in the bed. The transport of hydrogen through the bed is described by simple pipe flow, i.e. the flow rate, Q_{H_2}, is given by

$$Q_{H_2} = N_p \frac{\pi r_0^4}{8\ell\mu} \Delta p \qquad (6)$$

where N_p is the number of pipes, r_0 is the pipe radius, ℓ is the pipe length, μ is the viscosity of hydrogen and Δp is the pressure drop along the pipe and is assumed to be equal to the hydride hydrogen pressure. For the simulations presented we take

$$r_0 = 100 \ \mu m \qquad (7)$$

and

$$\ell = 10 \ cm$$

5

The number of pipes is calculated from the areal porosity, α, and given by

$$N_p = \frac{1-\alpha}{\pi r_0^2} \qquad (8)$$

In all calculations α was set equal to 0.1.

The behavior of the system is quite insensitive to the choice of these parameters because of the low gas flows required to balance heat fluxes. Gas flows required to balance varying heating rates are shown in Figure 3 for $LaNi_5H_6$. Approximately 70 sccm/cm²s of hydrogen flow balance 100 W/cm² heating. Using the above expression for Q_{H_2} and assuming a pressure drop of 1 atm, the value of Q_{H_2} is equal to 1.389 x 10⁵ sccm/cm²s. If the effective pipe radius is reduced to 10μm and the effective pipe length increased to 20 cm, the value of Q_{H_2} is reduced to 695 sccm/cm²s. The implication is that the flow rate will not be limited by bed characteristics but by the local temperature.
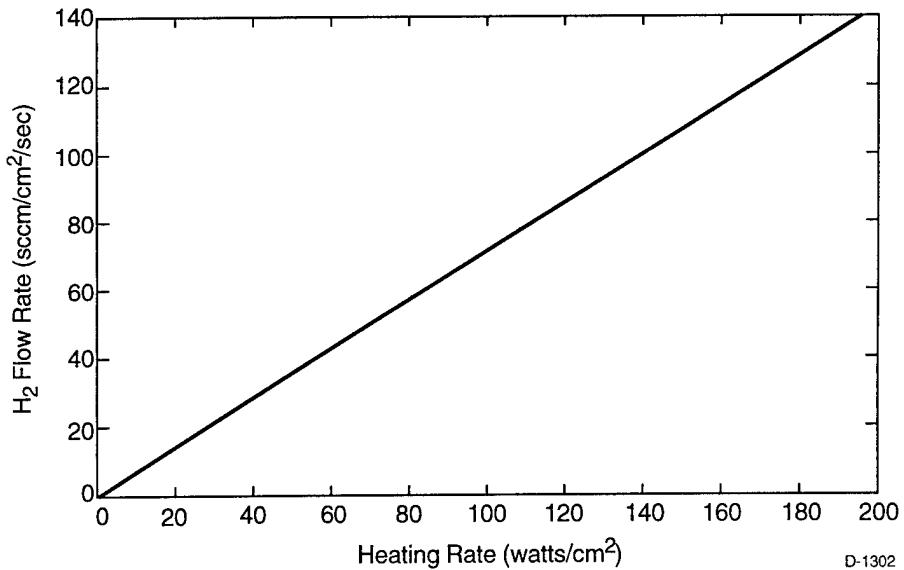
Figure 3. H_2 Flow as a Function of Heating Rate for $LaNi_5H_x$

The experimental hydrogen pressures, P_{H_2}, above $LaNi_5H_6$ and $(V_{0.89}Ti_{0.11})_{.95}Fe_{0.05}H_2$ have been fitted to expressions of the form

$$P_{H_2} = \exp(-\Delta H/RT + \Delta S/R) \qquad (9)$$

Values for these two materials are listed in Table 1 from Libowitz.[1]

The hydrogen vapor pressures above $LaNi_5H_6$ and $(V_{0.89}Ti_{0.11})_{0.95}Fe_{0.05}H_2$ are shown as a function of temperature in Figure 4. Both materials have vapor pressure above 1 atm at 300 K.

6

Table 1. Vapor Pressure Parameters

	ΔH (kcal/mol)	ΔS (cal/deg mol)
$LaNi_5H_6$	- 7.4	-35.5
$(V_{0.89}Ti_{0.11})_{0.95}Fe_{0.05}H_2$	-10.3	-25.8
(from Ref. 1 Libowitz, G. G., Electrochem, Soc. Proc. Vol 92-5,3 (1992)		
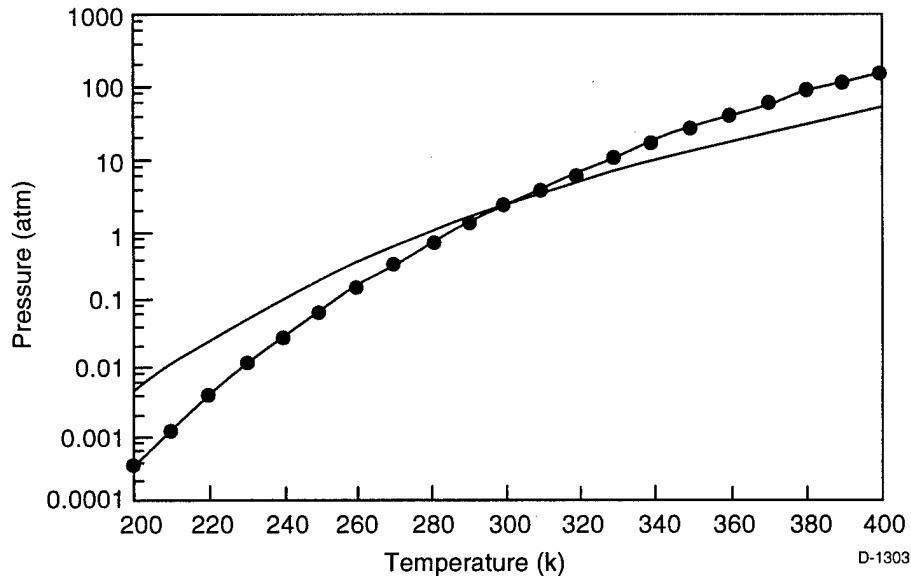
Figure 4. H_2 pressure Above $LaNi_5H_x$ (solid line) and $(V_{0.89}Ti_{0.11})_{0.95}Fe_{0.05}H_x$ (dot-solid line) as a Function of Temperature

This will require the use of a pressure tight bed. It will also result in the initial cooling of the window surface below ambient when the window is opened. This effect is seen in the simulations discussed below.

2.4   Initial Thermal Response Simulations

Calculations were performed using the PSI composite materials thermal response code. The code simulates the response of a multicomponent system with one ablating species and heat transfer by conduction and ablation. The thermal profile for a non-ablating material heated at 100 W/cm^2 is shown in Figure 5. The curves display the temperature at the surface and depths into the material. The thermal conductivity of the material is taken as 1.97 W/cmK. This value corresponds to an equimolar mixture of $LaNi_5H_6/Cu$. Figures 6 and 7 show thermal responses for non-ablating materials with thermal conductivity equal to 1.0 and 0.25 W/cmK.

The computed surface temperature depends strongly on the thermal conductivity, K. The surface temperature reaches 540, 630 and 970 K after 10 s heating for thermal conductivities

7
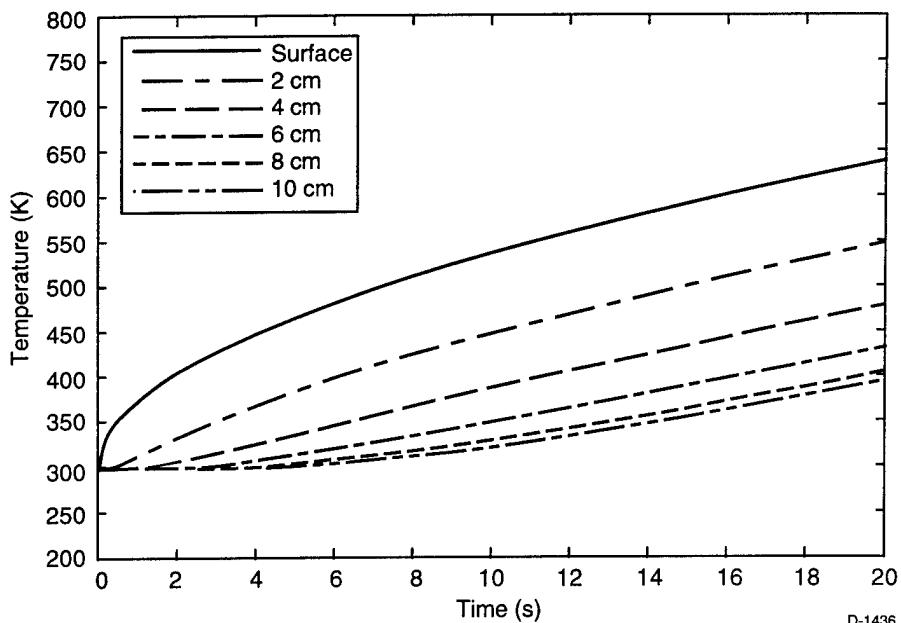
Figure 5. Thermal Response of Reference Material (No Pyrolysis) 100 W/cm^2, K = 1.97W/cmK
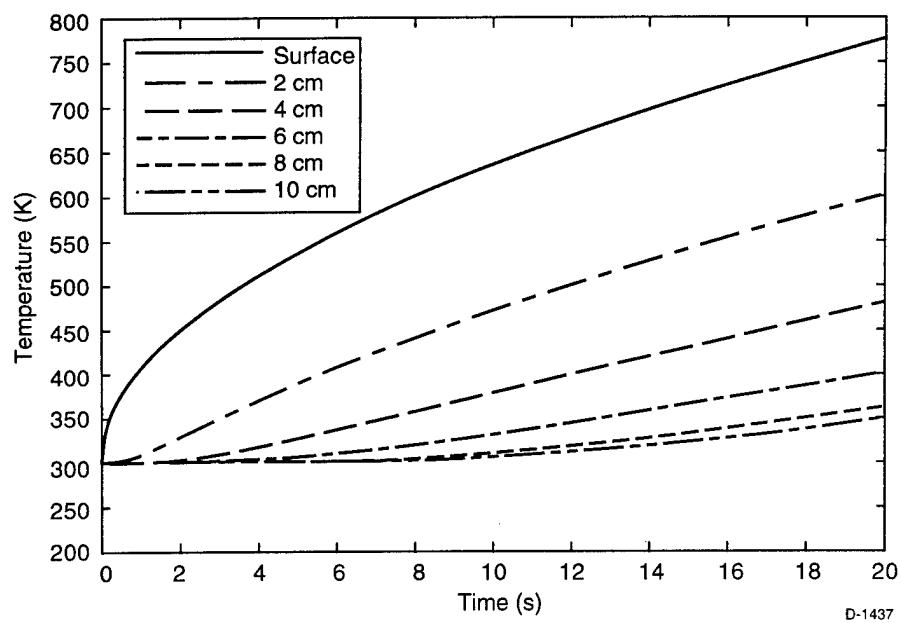
Figure 6. Thermal Response of Reference Material (No Pyrolysis) 100 W/cm^2, K = 1.0 W/cmK

of 1.97, 1.0 and 0.25 W/cmK. Note also that the distance that the thermal wave reaches decreases as the thermal conductivity decreases. For K = 0.25 W/cmK, the thermal wave barely reaches 4 cm below the surface at 10 seconds. This will also be true for a hydride containing bed. Therefore, in order to efficiently access the hydride, the bed thermal conductivity should be maximized. It should also be noted that 10 seconds is only a characteristic interception time for
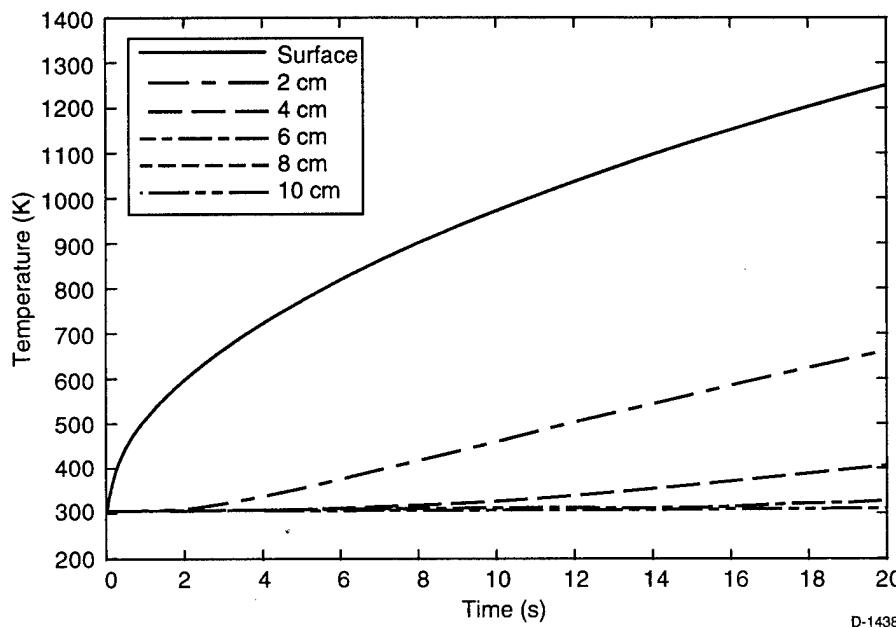
8

Figure 7. Thermal Response of Reference Material (No Pryolysis) 100 W/cm², K = 0.25 W/cmK

window exposure to the aerothermal environment. Some systems require one half the time to seek and impact threatening targets.

Figures 8 through 10 display the thermal history of a LaNi$_5$H$_6$ hydride bed heated at 100 W/cm². Figure 8 corresponds to a 50/50 LaNi$_5$H$_6$/Cu mixture with k = 1.97 W/cmK. The thermal response is markedly different than that of the non-hydride case shown in Figure 5.
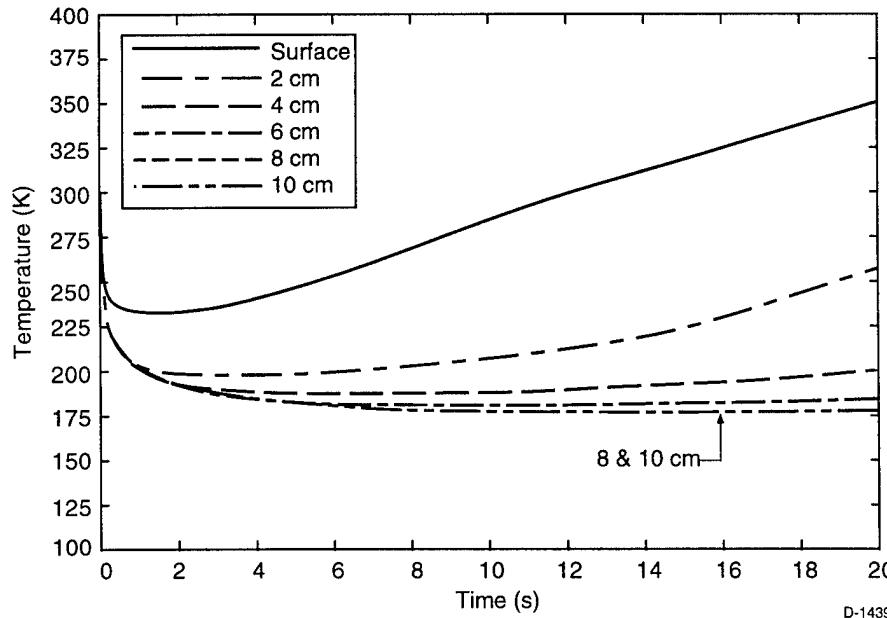
Figure 8. Thermal Response of LaNi$_5$H$_6$/Cu to 100 W/cm² Heating; K = 1.97 W/cmK

9
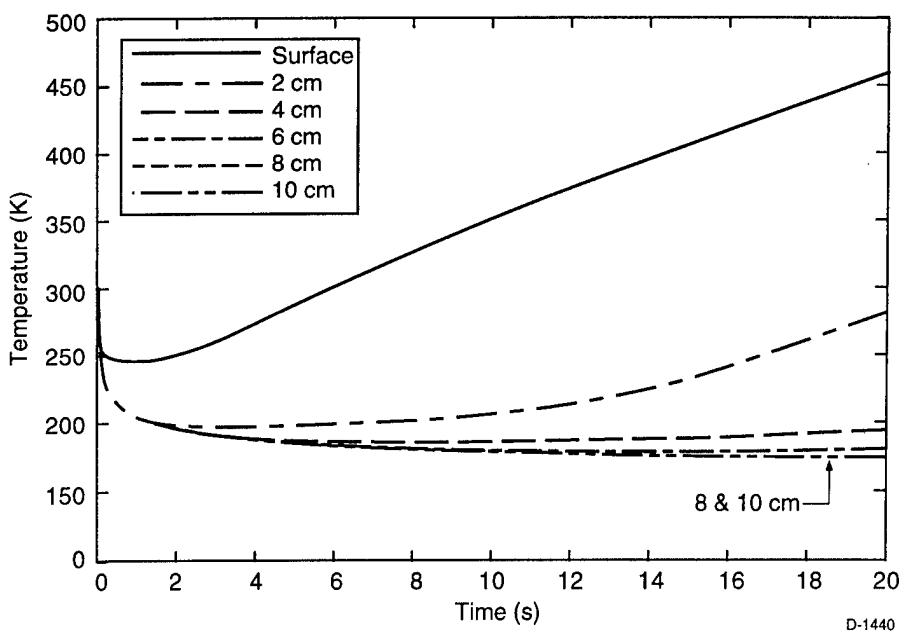
Figure 9. Thermal Response of $LaNi_5H_6/Cu$ to 100 W/cm^2 Heating; K = 1.0 W/cmk
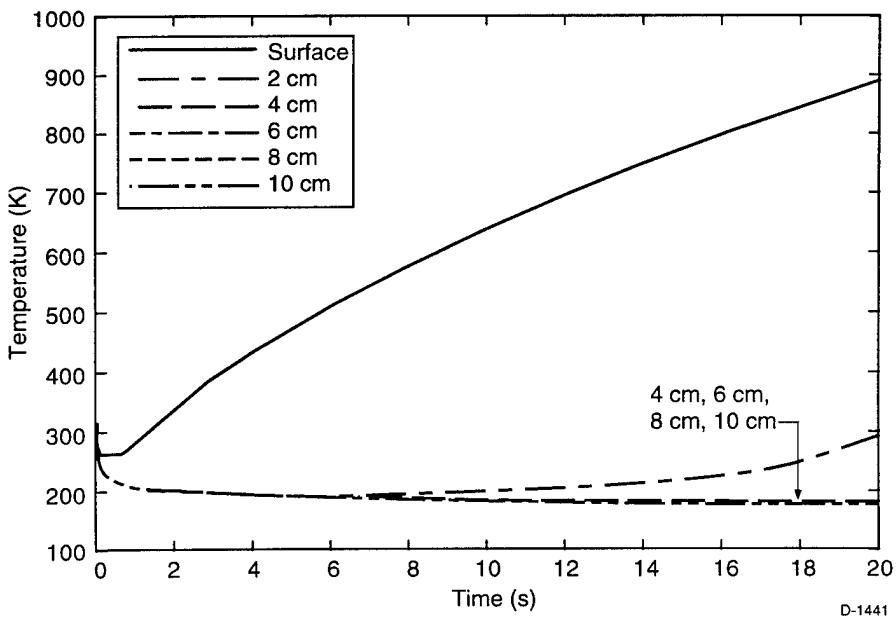
Figure 10. Thermal Response of $LaNi_5H_6/Cu$ to 100 W/cm^2 Heating; K = 0.25 W/cmK

Initially, the bed temperature drops from the 300 K to about 250 K. We assume that the window is opened at t = 0. Upon opening, hydrogen is released causing the window to cool. The cooling continues until a temperature is reached where the hydrogen pressure is very low and mass flow becomes small. This occurs at about 220 K. The surface temperature remains approximately constant for almost 3 seconds and then begins to rise slowly. The results shown are accurate to

10

within the magnitude of the abrupt increase, 10 to 15 deg. After 10 seconds heating, the surface temperature has risen to about 285 K. This can be contrasted to the value of 540 K for the non-hydride case. The calculation clearly shows the capability of the hydride bed to maintain low window temperatures.

Calculations in Figures 9 and 10 show the thermal response of hydride beds with lower thermal conductivities. For K = 1.0 W/cmK, the surface temperature reaches 350 K after 10 seconds and for K = 0.25 W/cmK, a surface temperature of 640 K is reached. These calculations emphasize the importance of constructing a hydride bed with maximum thermal conductivity for efficient window cooling.

Calculations were performed to examine the sensitivity of the simulations on the hydrogen flow rate. Calculations for a K = 1.97 W/cmK $LaNi_5H_6$/Cu bed with the flow rate reduced by a factor of 10 and 100. The results are shown in Figures 11 and 12 respectively. A factor of 10 reduction in the hydrogen flow rate increases the surface temperature at 10 seconds by about 25 deg to 310 K. A factor of 100 results in a surface temperature of 340 K after 10 seconds. The results show that the hydride bed can successfully cool the window even with a factor of 100 reduction in hydrogen production kinetics.

Several calculations were performed at heating rates of 200 W/cm^2. Figure 13 shows the behavior for a non-ablating window with a high thermal conductivity equal to 1.97 W/cm°K. The surface temperature is about 650 K after 5 seconds heating and increases to nearly 800 K after 10 seconds. Figure 14 shows the response of an $LaNi_5H_6$/Cu hydride window to 200 W/cm^2 heating. After 5 seconds heating, the surface temperature is about 360 K and after 10 seconds,
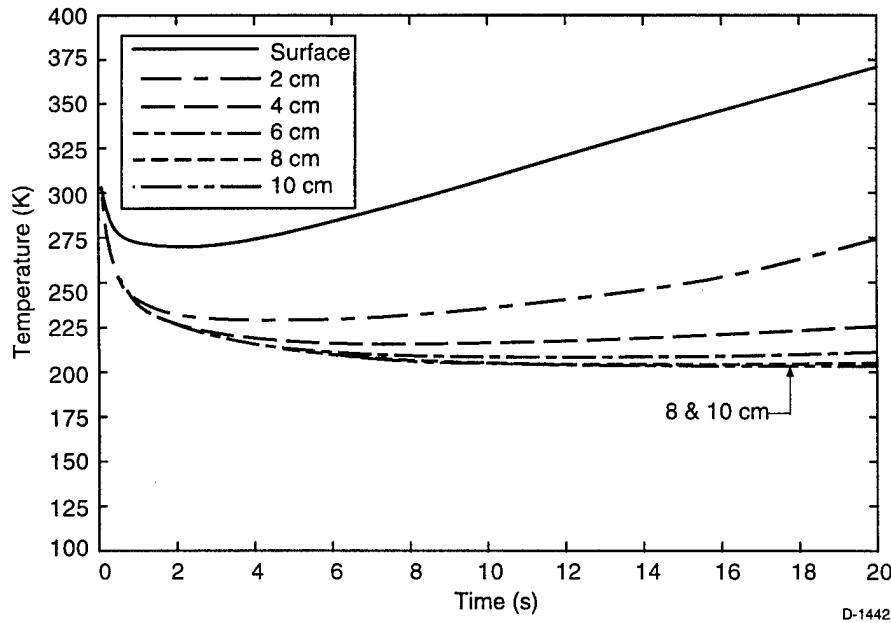
Figure 11.   Thermal Response of $LaNi_5H_6$/Cu to 100 W/cm^2 Heating; K = 1.97 W/cmK; Hydrogen Production Rate Reduced by Factor of Ten

11
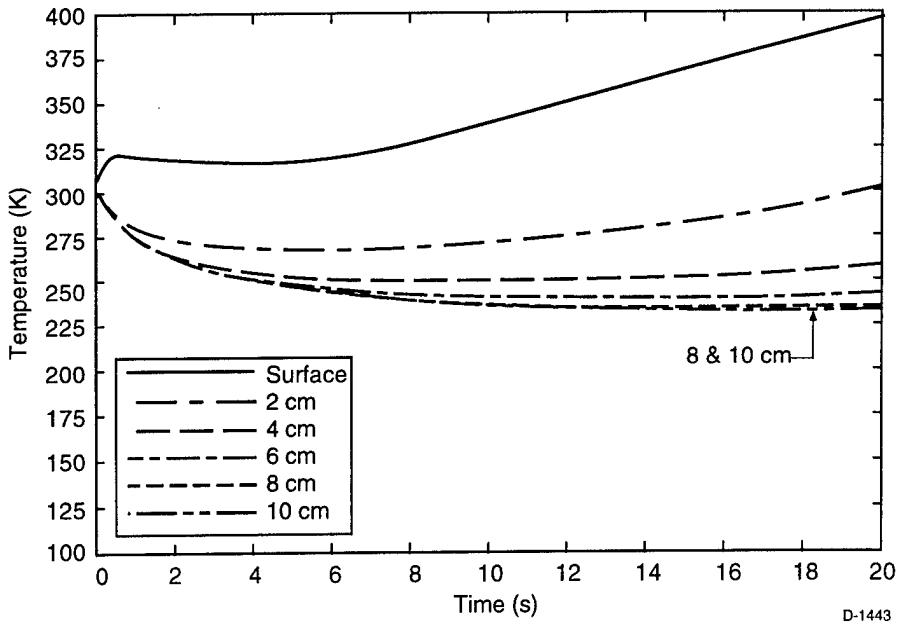
Figure 12. Thermal Response of LaNi$_5$H$_6$/Cu to 100 W/cm^2 Heating; K = 1.97 W/cmK, Hydrogen Production Rate Reduction Rate Reduced by Factor of 100
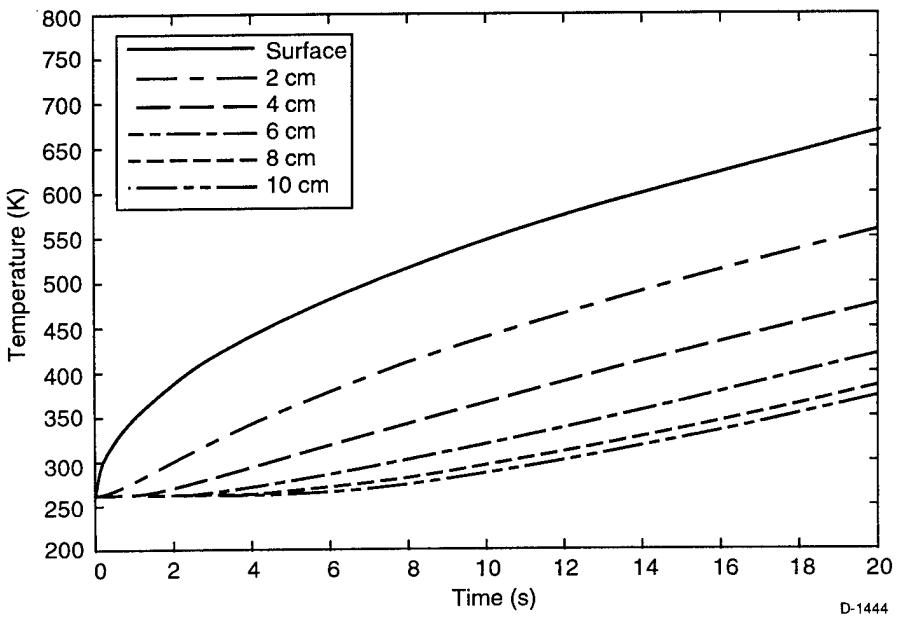
Figure 13. Thermal Response of Reference Material (No Pyrolysis) to 200 W/cm^2; K = 1.97 W/cmK

12
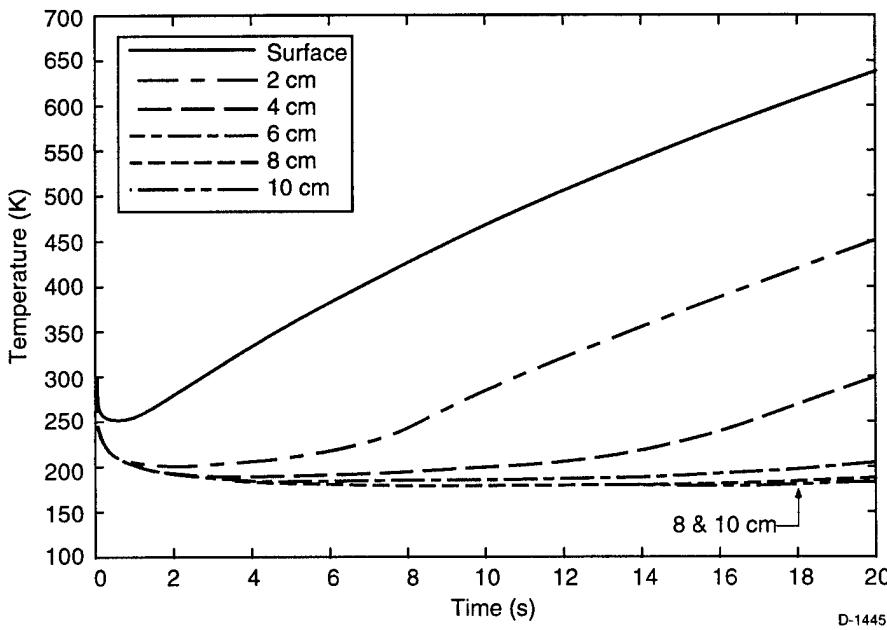
Figure 14. Thermal Response of $LaNi_5H_6$/Cu to 200 W/cm^2 Heating; K = 1.97 W/cmK

the surface temperature reaches 470 K. Thus the hydride window is capable of substantial cooling at this heating rate. It is most probable that this heating rate over these time periods is substantially greater than anticipated in realistic scenarios.

Simulations have also been performed for $(V_{0.89}Ti_{0.11})_{0.95}Fe_{0.05}H_2$/Cu mixtures. The mixture was formulated with a 1:3 Cu:hydride ratio yielding a thermal conductivity of 1.21 W/cmK. This hydride is potentially more effective than $LaNi_5H_6$ for window cooling since it has a higher heat of decomposition. Its vapor pressure dependence on temperature is shown in Figure 4 and is similar to $LaNi_5H_6$.

Figures 15 and 16 show the temperature variation of a $(V_{0.89}Ti_{0.11})_{0.95}Fe_{0.05}H_2$/Cu window heated at 100 and 200 W/cm^2 respectively. The behavior is qualitatively similar to that for the $LaNi_5H_6$ formulated window. Initially the window temperature drops to between 200 and 250 K. For the 100 W/cm^2 heating case the surface temperature is nearly constant over the 10 seconds heating period; its value after 10 seconds is 270 K. Subsurface temperatures are maintained at constant values of about 220 K. The results for the 200 W/cm^2, shown in Figure 16, indicate that the surface temperature is maintained at or below 300 K for 5 seconds and reaches 380 K after 10 seconds. Subsurface temperatures are virtually unaffected by the 200 W/cm^2 heating. These calculations show that this mixture is capable of effective cooling at heating rates up to 200 W/cm^2. In subsequent simulations, we will examine variable heating rates to represent realistic scenarios as well as attempt to optimize the hydride/thermal conductor formulation.

13
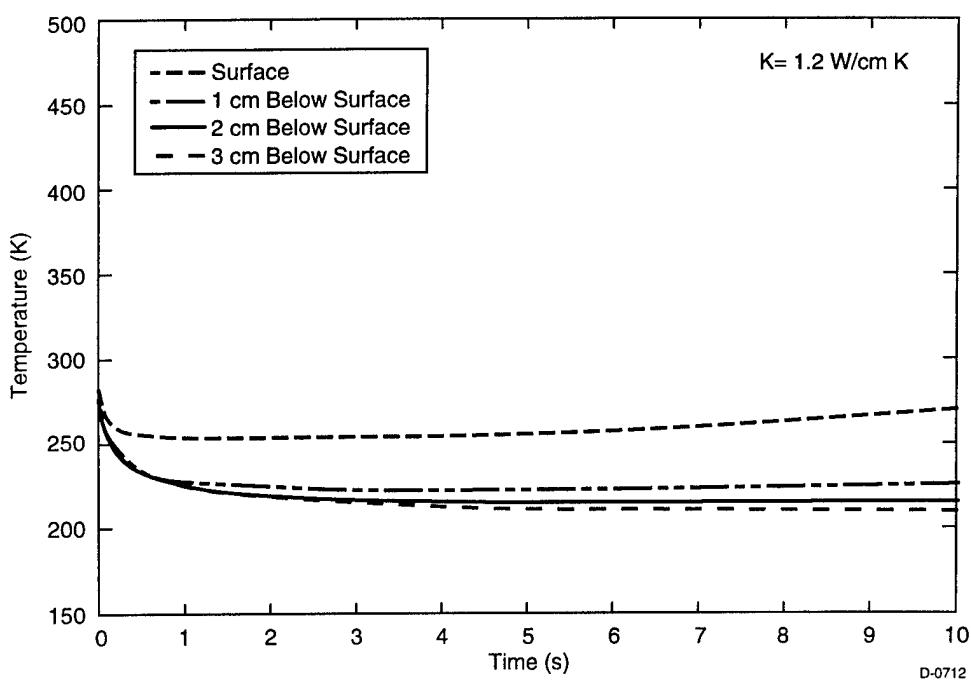
Figure 15. Thermal Response of $(V_{0.89}T_{0.11})_{0.95}Fe_{0.05}/Cu$ for a Heating Rate of 100 W/cm2
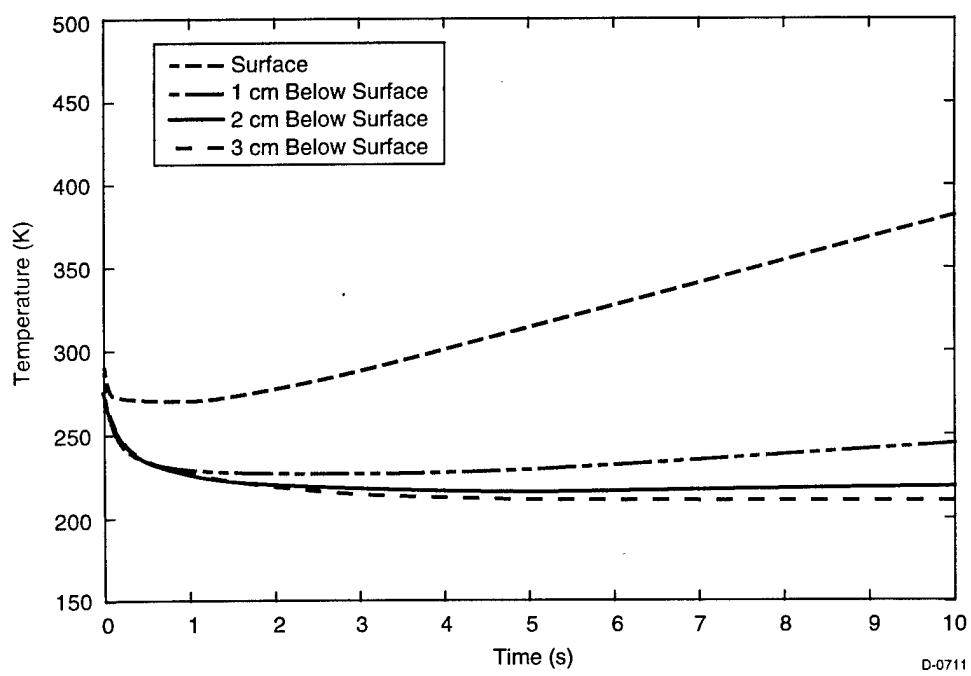
Figure 16. Thermal Response of $(V_{0.89}T_{0.11})_{0.95}Fe_{0.05}/Cu$ for a Heating Rate of 200 W/cm^2

14

2.4.1 Initial Assessment of Passive Window Cooling

We have simulated the thermal response of window materials composed of hydride/ thermal conductor mixtures. The examined hydrides were $LaNi_5H_6$ and $(V_{0.89}Ti_{0.11})_{0.95}Fe_{0.05}H_2$ mixed with Cu. No significant effort was made to optimize mixture compositions. The simulations were performed using the PSI composite material thermal response code modified to account for the kinetics and thermochemistry of the metal hydride hydrogen evolution.

Both hydride formulations showed that window temperatures can be maintained at or below 300 K at heating rates of 100 W/cm^2. The $(V_{0.89}T_{0.11})_{0.95}Fe_{0.05}H_2$ is seen to be more effective at 200 W/cm^2 heating rate and can maintain a window surface temperature at or below 300 K for heating periods up to 5 seconds. These simulations demonstrate the feasibility of the window concept. They also point to several areas for further investigation.

Additional hydrides should be examined. A vast variety of reversible metal hydrides have been characterized for hydrogen storage and other applications. The optimal hydride or class of hydrides for the window cooling concept needs to be determined.

The simulations indicate that the hydride bed thermal conductivity is a critical parameter for effective cooling performance. The initial bed formulations contained mixtures of hydride with copper. Additional high thermal conductivity material/hydride compositions need to be examined. Silicon carbide/hydride formulations are an obvious choice as well as diamond/ hydride mixtures. The goal of examining different formulations is to produce a mixture with a high thermal conductivity and high hydride density that will minimize window temperature increase under a prescribed heating scenario. It is anticipated that the optimal mixture will be a function of the specific projected heating pattern.

2.4.2 Alternative Window Concept Using Extraordinary Thermal Conductors

One offshoot of the present effort is the potential of alternative concepts for window temperature maintenance. The thermal response simulations clearly indicated that the window bed thermal conductivity is critical to window performance. Windows containing hydride but having low thermal conductivity do not maintain the surface temperature at low values. This is seen clearly in Figure 10 where after 10 s of 100 W/cm^2 heating the surface temperature increases to 630 K while the subsurface temperatures are maintained at about 200 K. This behavior is due to the effective thermal insulation of the hydride bed in the subsurface region. The defeat of the hydride bed concept by poor thermal conductivity suggests an alternative strategy using the fiber optic sensing concept embedded in an extraordinary thermal conductor as discussed in Subsection 2.6.2.

Figure 17 shows the thermal response of material heated at 100 W/cm^2 as a function of time. The material has a thermal conductivity equal to 4 W/cmK. After 10 s, the surface temperature has reached 420 K. For less severe heating scenarios, this response might be adequate for sensing, i.e., if a 5 s engagement at 100 W/cm^2 is anticipated, the surface temperature would only rise to 380 K or 80 degrees above ambient. If materials having higher
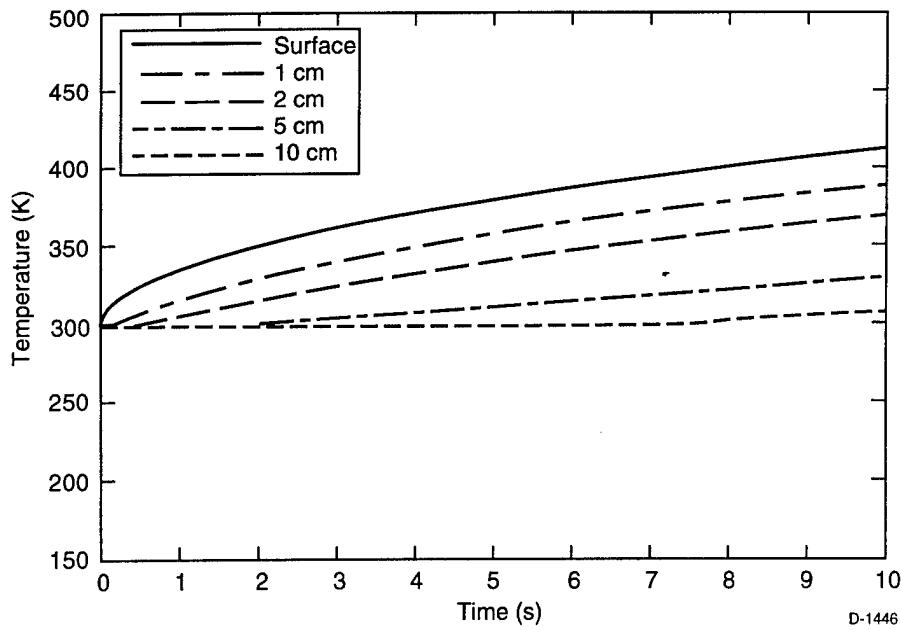
Figure 17. Thermal Response of High Thermal Conductivity Reference Material
(No Pyrolysis) to 100 W/cm² Heating Rate; K = 4.0 W/cmK

thermal conductivities such as SiC (K = 5.0 W/cmK) or diamond (K ~ 20 W/cmK) are used,
temperature rises can be further reduced. Moreover, conventional heat pipe devices can be
incorporated into these materials to further aid heat transport.

2.5 Empirical Hydrogen Desorption Kinetics

The above predictions assume that the bed temperature can be maintained at ~ 300 K
under the prescribed heating rates. In our initial feasibility calculations, we employed a simple
kinetic model to describe the kinetics of hydrogen desorption from the considered transition
metal hydrides. We have obtained empirical data for the hydrogen desorption of $LaNi_5H_x/Cu$
bed.[2] The empirical rate law for hydrogen desorption is

$$\dot{m} = C_d \exp\left(\frac{-E_d}{RT}\right) \left(\frac{P_g - P_{eq}}{P_g}\right) \rho_s, \frac{gm \ H_2}{bed \ volume \ s} \tag{10}$$

where P_g is the local hydrogen pressure, P_{eq} the equilibrium hydrogen pressure over the $LaNi_5H_x$
bed, ρ_s the density of the hydride bed. The constants E_d and C_d are equal to 16,473 J/mol and
9.57 s⁻¹, respectively.

16

2.6 Improved Thermal Response Calculations

We have performed thermal response calculations for $LaNi_5H_x$/Cu mixtures with k = 1.97 W/cmK heated at 100 W/cm^2. These improved calculations using Eq. (1) are compared to the initial calculations presented in Subsection 2.4 (Figure 8).

Figure 18 shows the thermal response of a $LaNi_5H_x$/Cu bed to 100 W/cm^2 using the above empirical hydrogen kinetics. The results are shown for 10 s heating periods. Over this time duration, the response is nearly identical to that of Figure 8. This is the case because for either hydrogen desorption rate law, the controlling factor in the bed temperature profile is the thermal conductivity. As long as the desorption kinetics are fast compared to the conductive heat flow this will be the case.
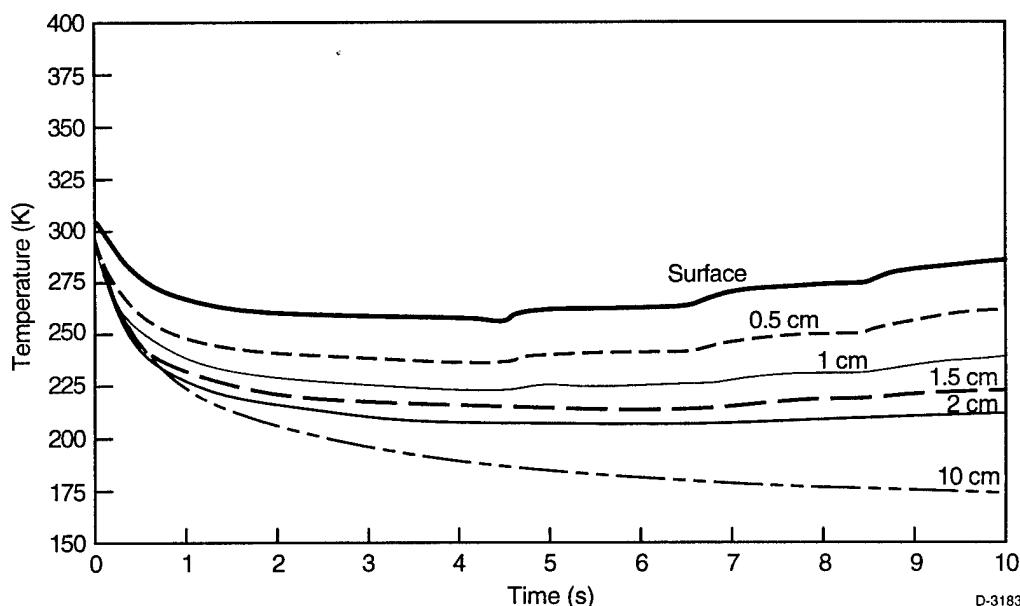
Figure 18. Thermal Response of $LaNi_5H_6$/Cu to 100 W/cm^2 Heating: k = 1.97 w/cmK. Hydrogen desorption kinetics described by Eq. (10) (see text).

2.6.1 Thermal Response Dependence on Bed Thickness

The design of an optical viewing system is facilitated by a thin hydride bed. We performed calculations to determine the thermal response of beds of varying thicknesses. The calculations were performed for heating rates of 100 W/cm^2. The results are shown in Figures 19 through 22 for the thermal response from 10, 6, 4, 3 and 2 cm thick beds. For beds 3 cm or more, thick thermal response is virtually identical. Only the 2 cm bed shows a significantly different response, that is due to all its hydrogen desorbing after about 7 to 8 seconds. The conclusion from these calculations is that the hydride bed will maintain cooling effectiveness as long as its hydride is not totally depleted of hydrogen independent of the bed thickness. The condition of not depleting all the hydrogen from the bed puts a minimum thickness on the bed from purely thermochemical considerations.

17
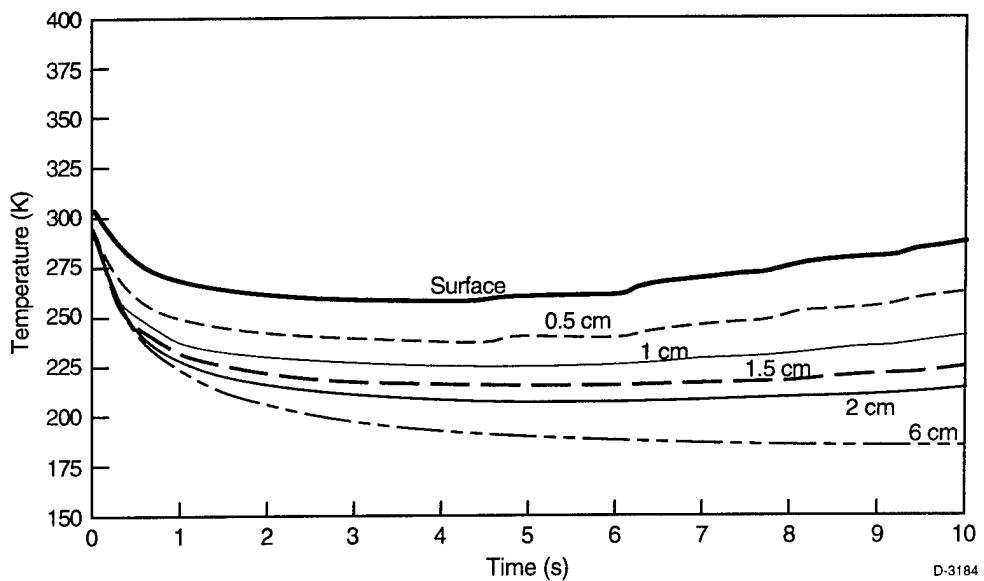
Figure 19. Thermal Response of LaNi$_5$H$_6$/Cu to 100 W/cm^2 Heating: k = 1.97 W/cmK, bed thickness = 6 cm. Hydrogen desorption kinetics described by Eq. (10) (see text).
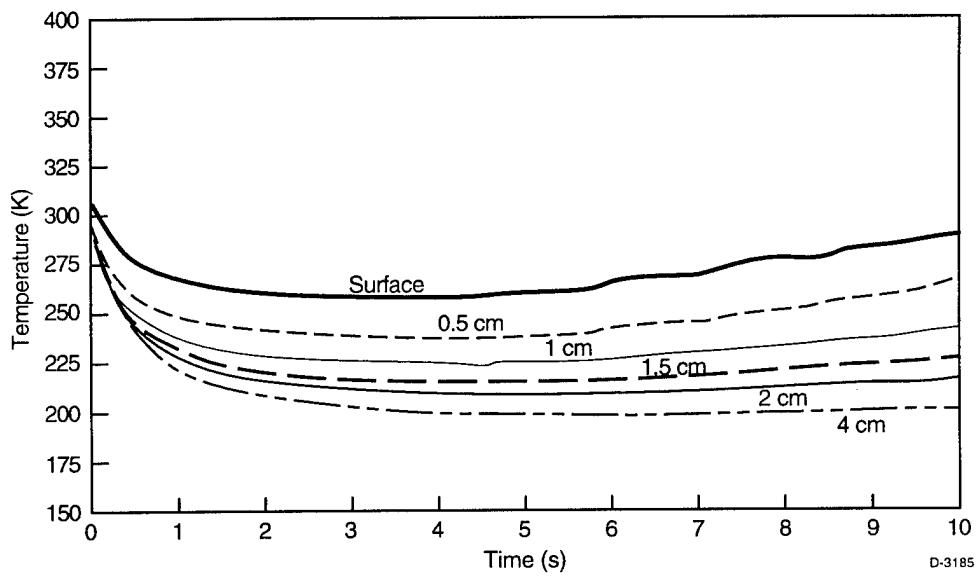
Figure 20. Thermal Response of LaNi$_5$H$_6$/Cu to 100 W/cm^2 Heating: k = 1.97 W/cmK, bed Thickness = 4 cm. Hydrogen desorption kinetics described in Eq. (10) (see text).
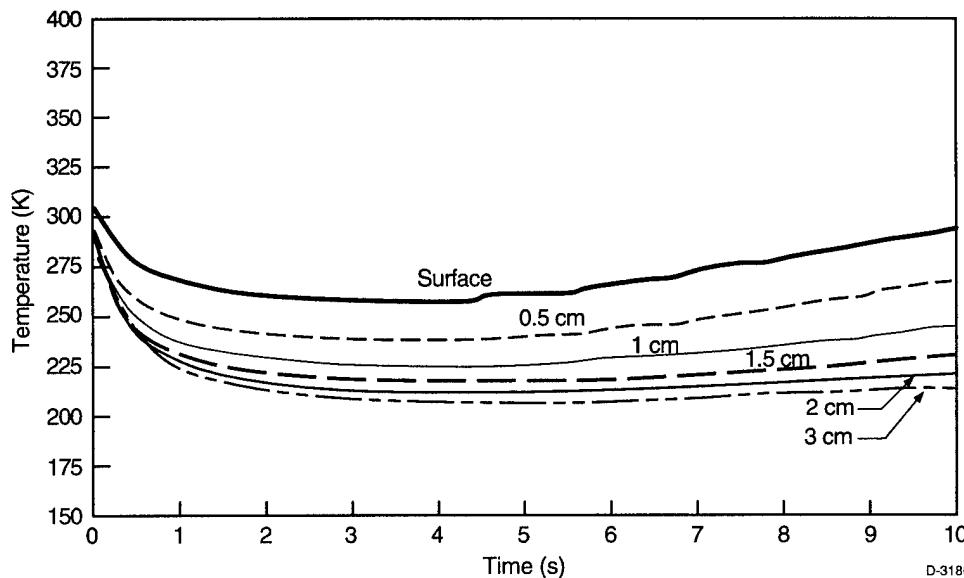
Figure 21. Thermal Response of LaNi$_5$H$_6$/Cu to 100 W/cm^2 Heating: k = 1.97 W/cmK, bed thickness = 3 cm. Hydrogen desorption kinetics described in Eq. (10) (see text).
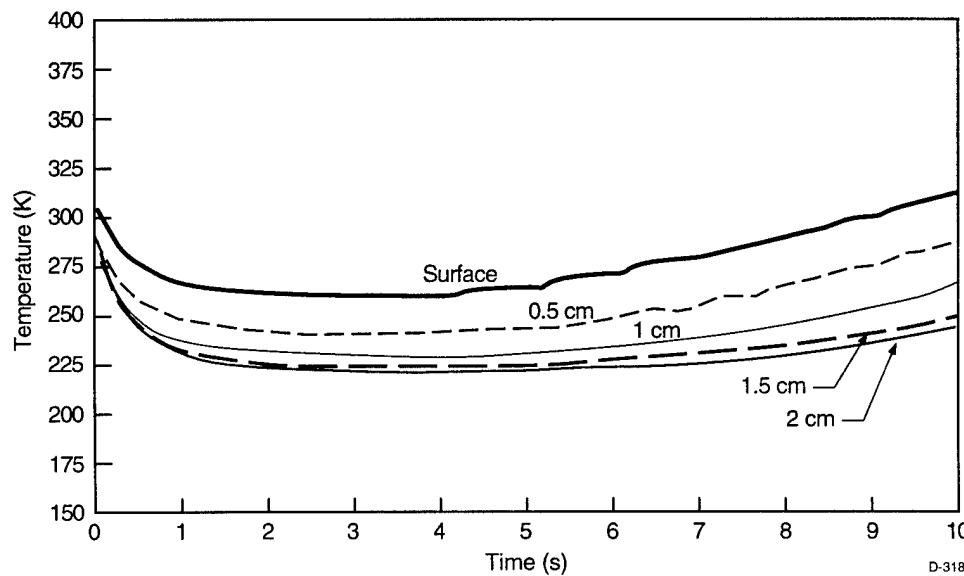
Figure 22. Thermal Response of LaNi$_5$H$_6$/Cu to 100 W/cm^2 Heating: k = 1.97 W/cmK, bed thickness = 2 cm. Hydrogen desorption kinetics described by Eq. (10) (see text).

2.6.2 Bed Fabrication and Thermal Conductivity Characteristics

We have begun a study of the fabrication of metal hydride/thermal conductor mixtures. The motivation for the use of additives is to increase the hydride bed thermal conductivity. The straightforward addition of powdered hydride to a powdered thermal conductor is not an efficient use of the conductor. Higher conductivity mixtures can be obtained by mixing the powdered hydride with fibers of thermal conductor. This can readily be done with copper metal by using a fine mesh copper "steel wool." Similarly, SiC is obtained in a fiber form. Diamond is not available in a fiber form and the simple mixing of metallic hydride with diamond powder may not result in a particularly high thermal conductivity mixture. We note that the use of fibers is dictated by the need to retain thermal connectivity throughout the bed.

An intriguing material is made by Amoco Performance Products, Inc. They produce a graphite fiber K-1100 for thermal management applications. It is produced as a continuous fiber and is a highly oriented crystalline pitch fiber. Its thermal conductivity is three times that of copper, i.e., k = 11 W/cmK. A 50/50 volumetric mixture of $LaNi_5H_x$ with K1100 might have a thermal conductivity as high as 5.5 W/cmK. Actual conductivities will have to be determined empirically.

Figure 23 shows the thermal response a $LaNi_5H_x$/K1100 bed with k = 5.0 W/cmK to 100 W/cm^2 heating over a 10 s interval. As can be seen, the bed temperature quickly drops from its initial value of 300 K to about 270 K where it remains over the entire heating period. The ability of the bed to maintain a nearly constant, low temperature is a consequence of its high thermal conductivity.
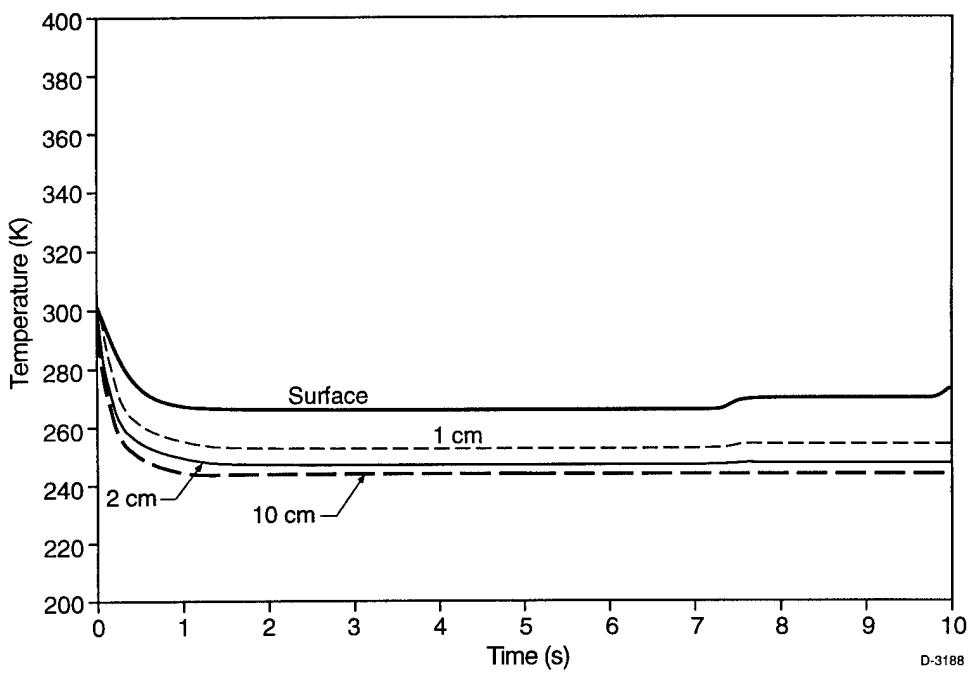
Figure 23. Thermal Response of $LaNi_5H_6$/K1100 to 100 W/cm^2 Heating: k = 5.0 W/cmK. Hydrogen desorption kinetics according to Eq. (10) (see text).

In conclusion then, these calculations show that a mixed metal hydride bed can keep a fiber optic system cold against nominal aerodynamic heating over two typical engagement times. More detailed predictions are warranted once a specific window design has been established. Alternative techniques for improving bed conductivity would be to introduce high conductivity, e.g., diamond, bed cover, and bore-hole walls.

2.7 Fiber Optic Heating

The proposed cooled window concept consists of a hydride bed with fiber optic ports through it to allow viewing. An issue of importance is the amount of temperature increase in a fiber optic. The potential consequences of such heating are discussed elsewhere in this report. The fiber optic heating model is discussed here.

We consider a cylinder of fiber optic material embedded in a hydride bed. The hydride bed is assumed to maintain the radial surface of the fiber optic at a constant temperature, T_0. We assume $T_0 = 300$ K. The exterior surface of the fiber optic is heated from above at a constant rate, I_0. The initial temperature of the fiber optic is assumed equal to the hydride bed. A schematic is given in Figure 24.
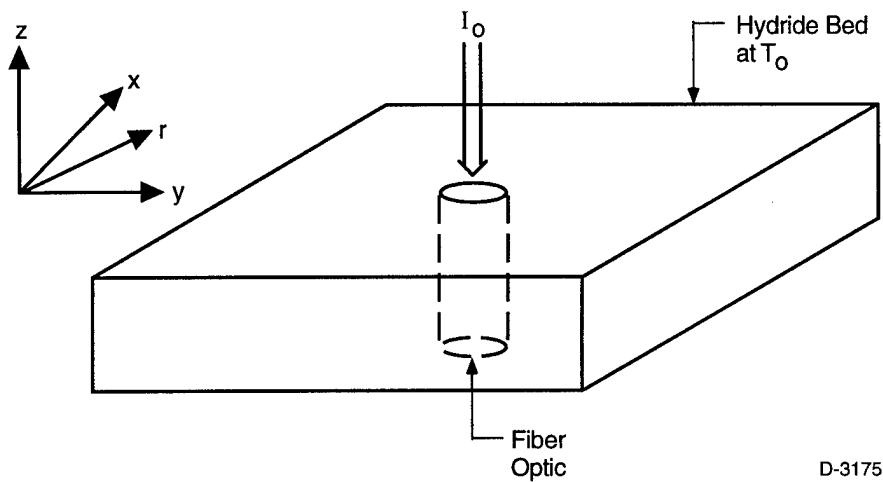
Figure 24. Schematic of Fiber Heating

The solution of the heat conduction equation for the increase in fiber optic temperature, $\Delta T (r, z)$ in the steady state case is

$$\Delta T (r, z) = \frac{2 I_0}{\pi k} \int_0^\infty e^{-\lambda z} J_0 (\lambda r)\{\sin \lambda r - \lambda r \cos \lambda r\} \frac{d\lambda}{\lambda^2} \qquad (11)$$

where k is the thermal conductivity of the fiber and λ is in units of inverse length. Figure 25 shows the thermal conductivities of silicon and germanium as a function of temperature. These two materials are candidate fiber materials.

21
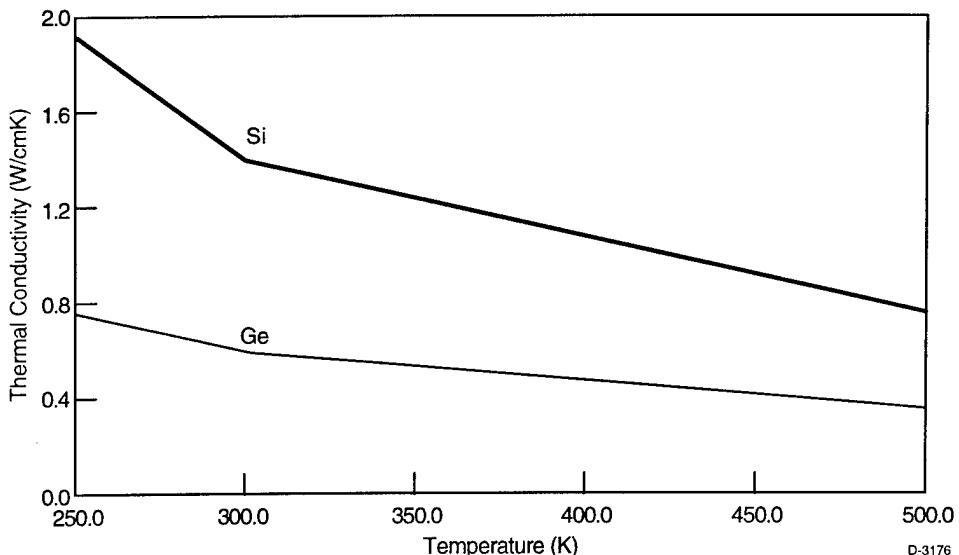
Figure 25. Thermal Conductivities of Silicon and Germanium as a
Function of Temperature

At the fiber surface, the value of ΔT is given by:

$$\Delta T\ (r) = \frac{2\,I_o}{\pi k}\int\limits_0^\infty\ J_o\ (\lambda r)\{\sin\ \lambda r - \lambda r\cos\ \lambda r\}\ \frac{d\lambda}{\lambda^2}\ .\tag{12}$$

We have employed Eqs. (11) and (12) to compute the centerline increase in fiber temperature for fibers of varying thermal conductivities as a function of fiber radius for varying heating rates. The results are shown in Figures 26 through 31. Each curve is labeled by the fiber thermal conductivity. Silicon fibers have thermal conductivities at 300 K of about 1.4 W/cmK, Ge about 0.6 W/cmK.

As can be seen, an Si fiber surface will experience less than 25°C maximum increase in temperature at a heating rate of 100 W/cm², Figure 26. For Ge fibers the temperature increase is about 50°C, Figure 29. The temperature increase 0.5 cm below the surface is reduced to about 10 and 20°C for Si and Ge respectively. The behavior at other heating rates is seen readily in Figures 27, 28, 30, and 31. The consequences of fiber heating on optical signal evaluation is discussed in the next subsection.

22
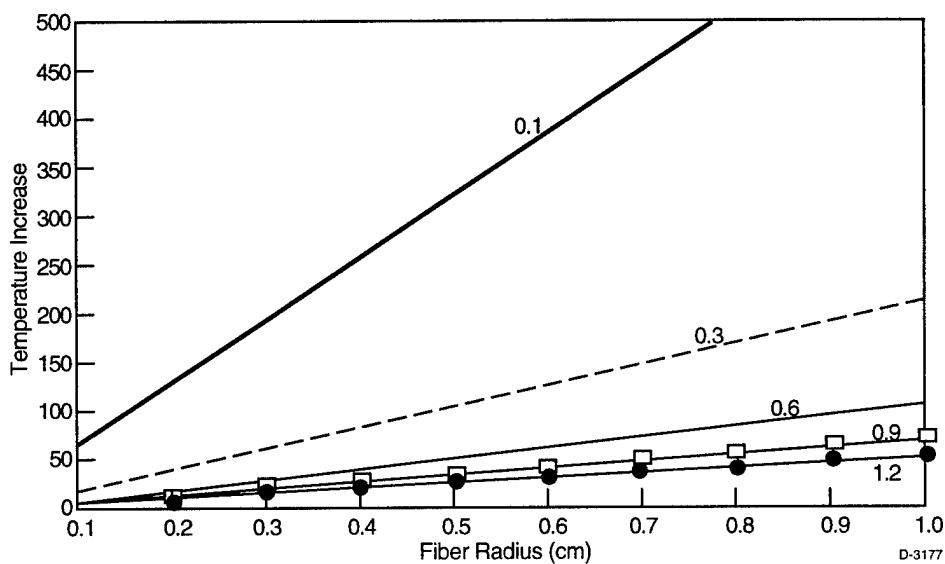
Figure 26. Fiber Surface Temperature Increase at Surface on
Centerline: $I_o = 100$ W/cm^2
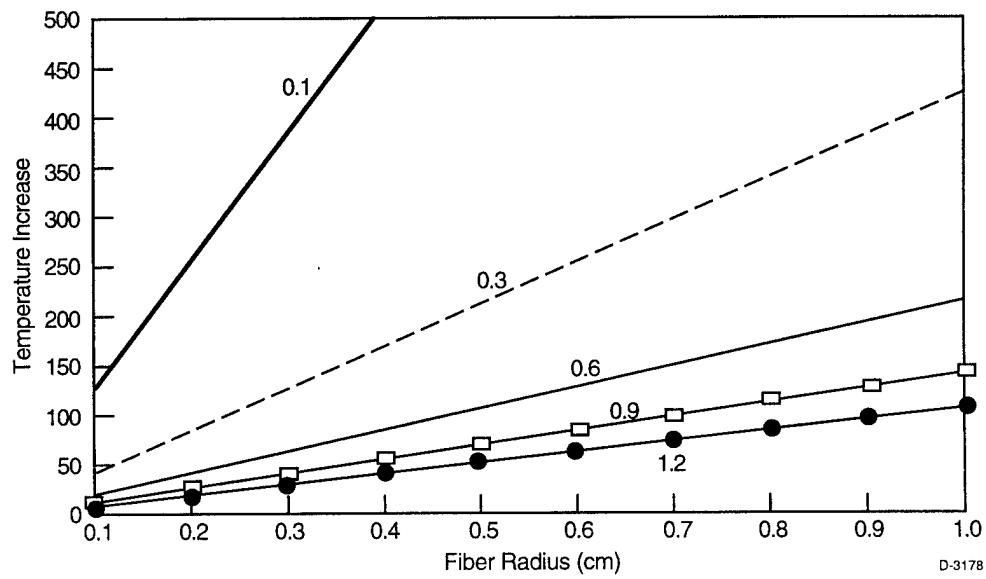
Figure 27. Fiber Surface Temperature Increase at Surface on
Centerline: $I_o = 200$ W/cm^2

23
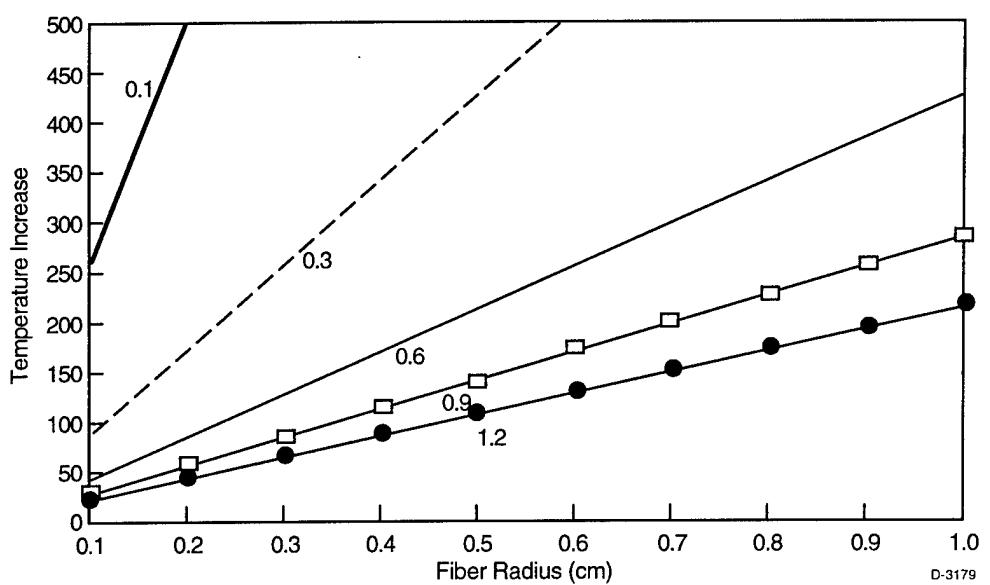
Figure 28. Fiber Surface Temperature Increase at Surface on
Centerline: $I_o = 400$ W/cm^2
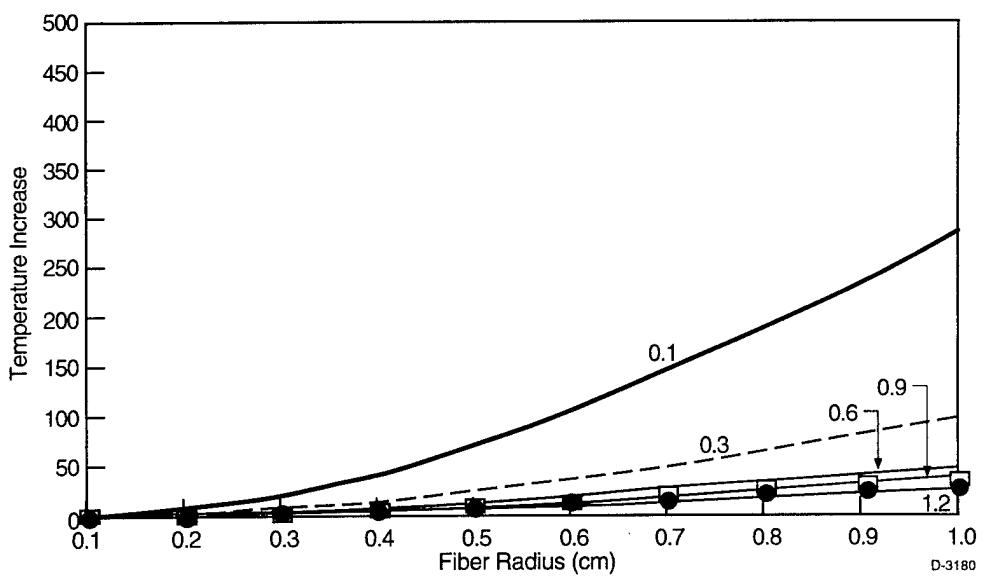
Figure 29. Fiber Temperature Increase 0.5 cm Below Surface on
Centerline: $I_o = 100$ W/cm^2
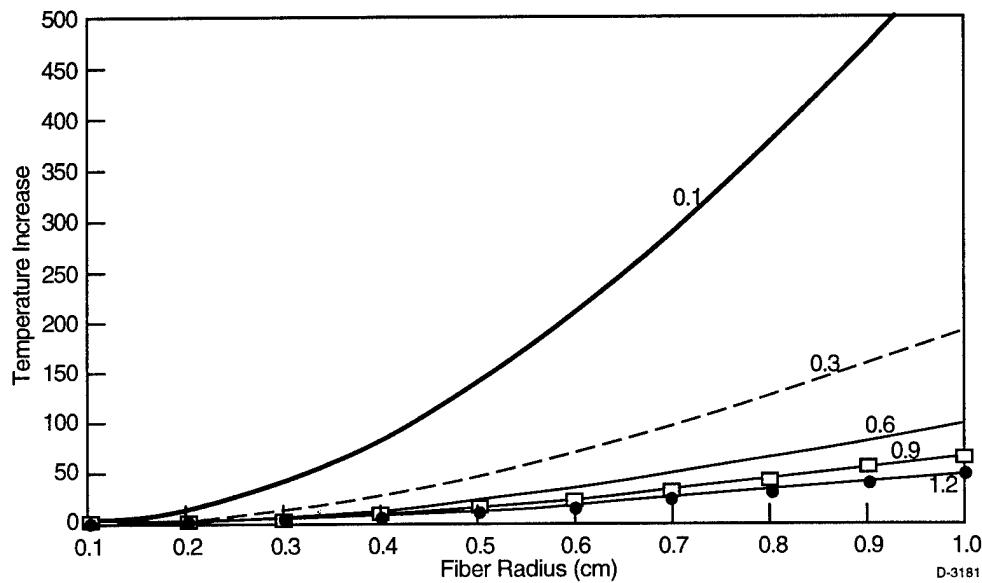
Figure 30. Fiber Temperature Increase 0.5 cm Below Surface on
Centerline: I_o = 200 W/cm^2
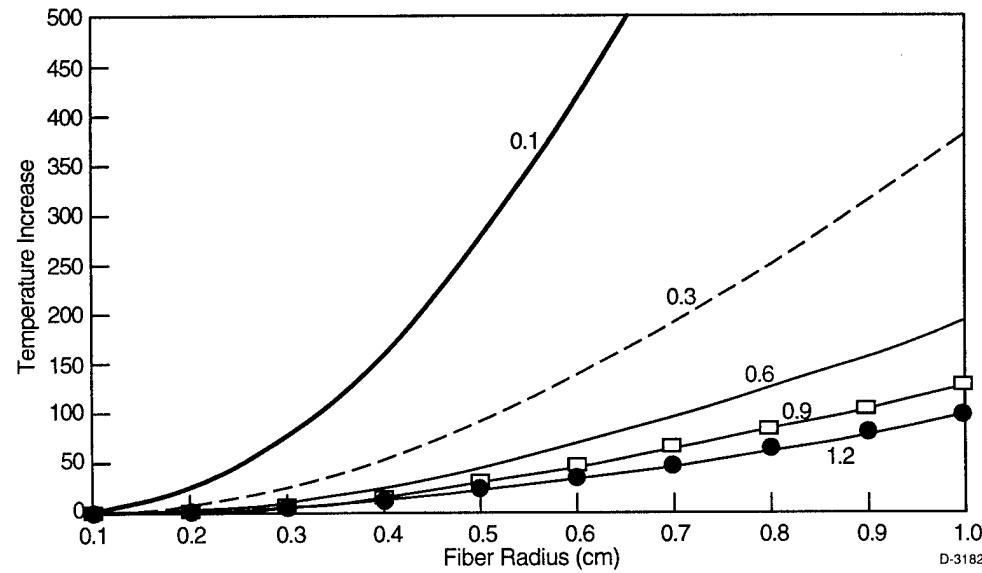
Figure 31. Fiber Temperature Increase 0.5 cm Below Surface on
Centerline: I_o = 400 W/cm^2

2.8   Preliminary Window Design

A task was carried out to develop preliminary optical design concepts for the proposed transition metal hydride-cooled IR seeker window. The basic objective was to establish the feasibility of designing a *multi-aperture* optical window with thermal, mechanical and optical properties that enable efficient metal hydride evaporative cooling of the window elements, while providing the required optical viewing access and resolution needed for the seeker's mission. Guidelines for mission requirements, operational scenarios, and geometries were derived from published data from recent optical seeker design efforts carried out by Loral Infrared Imaging Systems[3] and McDonnell Douglas.[4]

Figure 32 presents some of the principal window mount and viewing parameters that must be considered in designing an IR seeker window. The various geometric parameters shown play an important role in window design and performance. In particular key parameters that must be taken into account include vehicle cone angle (θ_t), nose radius (R_n), window cavity location (s_w), window cavity dimension (l_w), desired sensor viewing angle θ_{LOS}), and the required sensor field of view (FOV) (or "field of regard"). The nose configuration and window location will affect window surface heat flux and, along with the other parameters mentioned, must be considered in the window optical design. A realistic range of values of these parameters was considered for our preliminary design study.[3,4] For illustrative purposes, we present here values of some of these parameters used in the baseline design of Reference 3.

$$\text{From Reference (a):} \begin{cases} \theta_t = 15° & l_w = 2.7 \text{ in.} \\ R_n = 0.4 \text{ in.} & \theta_{los} = 7.6° \\ S_w = 7.4 \text{ in.} \end{cases}$$
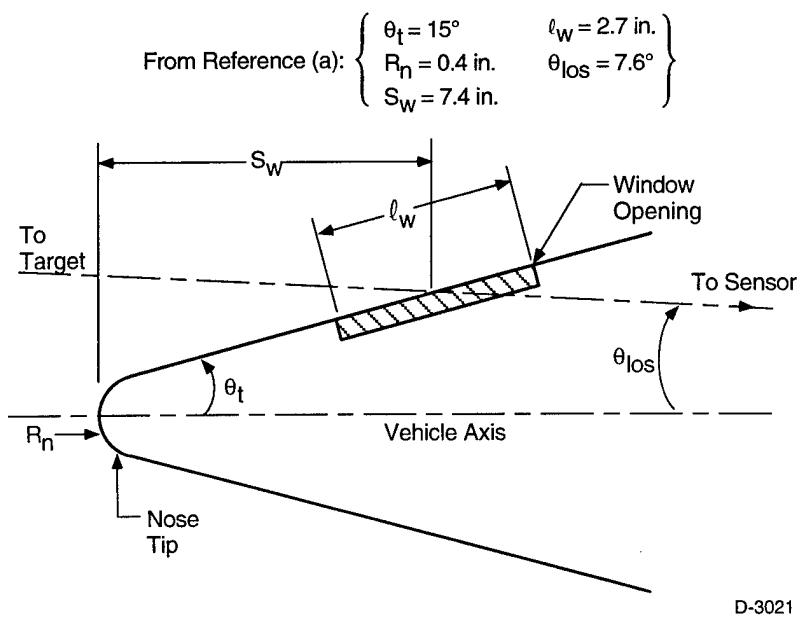
D-3021

Figure 32. Geometric Parameters that must be Considered in Designing
an IR Seeker Window

26

2.8.1 Basic Design Concept

Figure 33 below schematically illustrates the basic design concept investigated.
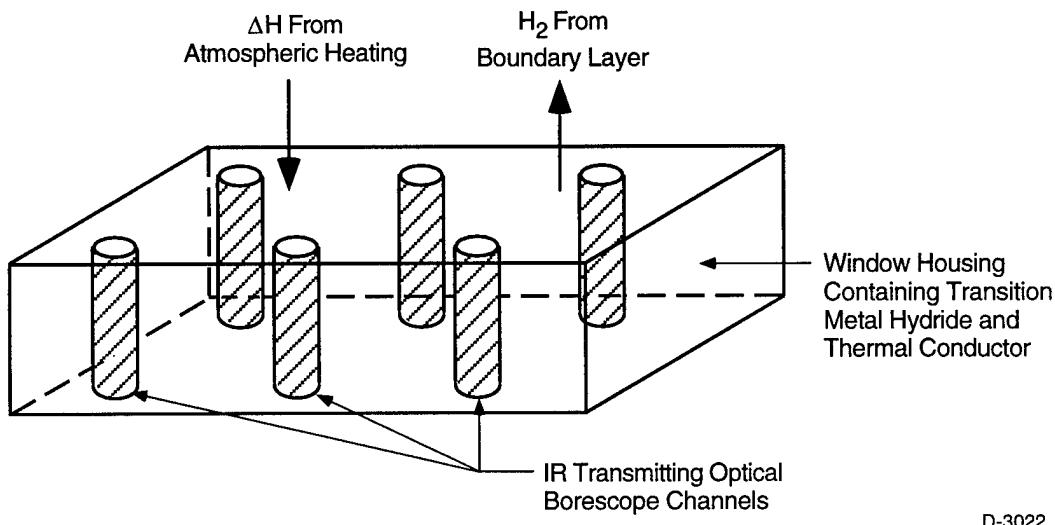
Figure 33. Basic Design Concept for Multi-Aperture IR Seeker Window Employing
Transitional Metal Hydride Evaporative Cooling

In its simplest possible embodiment the window assembly would consist of a limited array of separate window ports filled with IR transmitting optical material. (*As will be shown later, practical sensor FOV requirements combined with geometric constraints for effective cooling necessitate a more sophisticated optical design.*) The objective of the array of smaller diameter window ports is to enable effective radial cooling of the window optics by the metal hydride-filled cooling jacket.

In the design represented in Figure 33, the maximum diameter allowed for each optical channel is set by requirements for good radial cooling of the window element by thermal conduction. Effective cooling is needed not only to limit overall window temperature rise by aerothermal heating, but also to minimize thermal gradients across the aperture which will cause optical wavefront aberrations. The <u>total</u> number of ports needed, on the other hand, is determined by the total light collection aperture required to achieve acceptable sensor S/N as well as to meet diffraction-limited requirements for achieving angle measure accuracy (AMA) specifications of the seeker. These various design trades are discussed in detail below along with our proposed optical design approach for achieving sensor FOV requirements.

2.8.2 Heat Transfer Considerations

Preliminary "zeroth" order heat transfer calculations were performed to assess the effect of individual window port diameter on window temperature rise and temperature uniformity. The geometry and conditions assumed for these preliminary calculations were that of a cylindrical optical element heated at the front surface and cooled on the sides by immersion in a

27

fixed temperature (T_b) "bath" or heat sink assumed to be in excellent thermal contact with the window. If we assume the surface heat flux to be I_0, the radius and thickness (length) of the window element to be r_w and l_w, respectively, and the thermal conductivity of the window material to be k, we estimate the temperature rise at the center of the window to be:

$$\Delta T = I_0 r_w^2 / 2 l_w k \quad [\text{where } \Delta T = T_w(r=0) - T_b] \tag{13}$$

(see earlier analysis of Subsection 2.2). It should be noted that this relationship is valid for long heating times under which steady state conditions have been approached, i.e., $t_{heating} > r_w^2$ (and l_w^2)/$\varkappa$, where $\varkappa$ is the thermal diffusivity of the window material. Thus, for mission heating times > 4 s and sapphire as the window material ($\varkappa = 0.11$ cm^2/s), this relationship would apply for characteristic window element dimensions < 0.7 cm. For silicon ($\varkappa = 0.6$ cm^2/s), on the other hand, the relationship applies for window dimensions ≤ 1.5 cm.

In Figure 34 we present a plot of the estimated centerline temperature rise of a sapphire and a silicon window as a function of window radius. Temperatures were computed using Eq. (13), an assumed front surface heat flux of 200 W/cm^2, and a window thickness (length) of 6.5 mm. Temperature rises for other conditions will scale directly with heat flux and inversely with window thickness (as long as the window remains thermally thin as described above).

Figure 34. Computed Centerline Window Temperature Rise versus Window Radius

One can see from this plot the clear advantage of a higher thermal conductivity window material such as silicon for limiting the window temperature rise. For example, for the same window dimensions, the temperature rise is about 5x lower with silicon than with sapphire. Alternatively for the same design limit on window temperature rise, the acceptable diameter for the silicon window is about 2.2x larger than that for sapphire. For example, to limit the centerline window temperature rise to < 40 K, a sapphire window would have to have a diameter < 0.58 cm while a silicon window could be as large as 1.3 cm.

28

In the Loral Imaging Systems study (Reference 3) a design was developed for an IR seeker window which is recessed in a cavity to reduce aerodynamic heating. The objective of this design was to reduce window temperature rise to the point where active window cooling could be dispensed with. With that design, for example, it was shown to be feasible to limit the maximum window temperature rise at the end of a 4s intercept at 25 km altitude to < 150 K. (A sapphire window was assumed.) We think a reasonable goal of the current window design would be to limit the maximum window temperature rise under similar aerodynamic heating conditions to at least a factor of 5 to 10 lower, i.e., < 15 to 30 K. The preliminary results shown in Figure 34 indicate that to achieve this requires limiting the radius of each individual window to < 0.2 cm for a sapphire window and < 0.4 to 0.5 cm for a silicon window.

In addition to a requirement to limit the overall window temperature rise to reduce background signal seen by the IR sensor, there is also a need to limit thermal gradients across the window aperture so as not to introduce undue wavefront distortions to the target signal. The estimated edge to center wavefront distortion is approximately given by:

$$WFD = n\Delta t + t\Delta n \quad \text{where}$$

n is the window index of refraction at temperature T_0, t is the window thickness and, Δt and Δn are, respectively, the change in thickness and index of refraction at the window centerline due to the rise in temperature.

Let us now estimate the window temperature rise at centerline that is required to assure that the wavefront error introduced is small, i.e., < one wavelength of light (3 to 5 x 10^{-4} cm). Using handbook values for the temperature dependent linear expansion coefficients and refractive indices of sapphire and silicon and assuming a window thickness of 6.5 mm, we then find,

$$\Delta T_{max} \text{ (sapphire)} < 23 \text{ K and}$$

$$\Delta T_{max} \text{ (silicon)} < 3 \text{ to } 5 \text{ K .}$$

The lower allowable temperature rise for silicon as compared to sapphire arises from silicon's index of refraction having a significantly higher temperature dependence. It should be noted that the index of refraction of germanium has an even higher temperature dependence than that of silicon.

From the thermal considerations and results presented above, we therefore conclude that, for proper cooling and temperature uniformity, the individual window elements of the proposed multi-aperture window design will likely have to be no more than 0.5 cm diameter (0.25 cm radius). We now discuss below the implication this has for the overall window design in light of anticipated requirements for sensor FOV, total light collection, and sensor spatial resolution/ angle measurement accuracy.

2.8.3 Optical Design Considerations

FOV Requirements

For the purpose of the present analysis we have assumed engagement geometries and interceptor/target velocities similar to those considered for the EndoLEAP mission[3] and, therefore, also assume similar FOV requirements for the sensor. In Ref. 3, it was shown that for direct-hit missions (the majority of missions of interest) the desired aperture FOV is approximately 2.5 to 12.7 deg from the vehicle axis, thus a total FOV of 10.2 deg. This is illustrated in Figure 35.
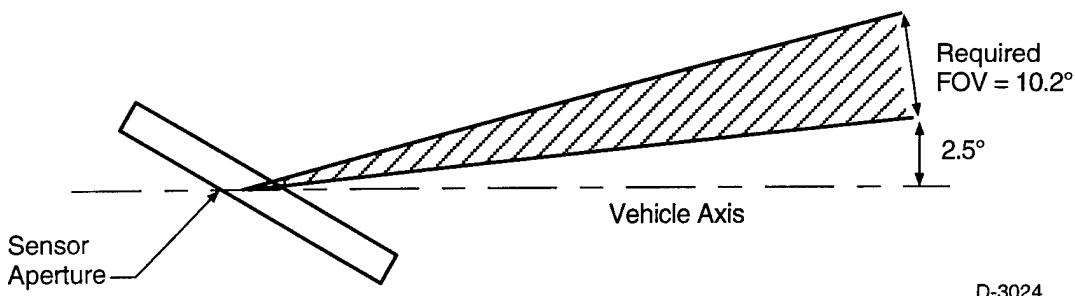
Figure 35. Field-of-View Required for Proposed Direct-Hit Endoatmospheric IR Seeker Missions (according to Reference 3).

For the currently proposed design utilizing a multi-aperture window plate, the maximum FOV that is possible is given by the aspect ratio of an individual port, that is the ratio of the diameter of the port to the length of the port. Assuming a maximum port diameter of 5 mm as determined above, and a total port length of 20 mm (see earlier section of report on hydride loading requirements), we find that under the best of conditions, (assuming the principal objective lens can be mounted virtually flush to the back of the window), the maximum full angle FOV is about 14 deg. Because of the highly acute angle of the nose cone, the need for small "look angles" with respect to the vehicle axis, and the substantial size of the overall window assembly required to meet *total* aperture requirements (see discussion below), this most favorable viewing situation cannot be achieved, however.

Figure 36 helps to illustrate some of the geometric constraints. In short, for a 15 deg half-angle nose cone, a required minimum "look angle" of 2.5 deg, and assumed window assembly length, l_w, of no less than 6.8 cm (a discussion which follows suggests that an even longer window may be required), one finds that the closest practical center to center spacing between the window assembly and the lens is about 32 mm. The effect of this required lens to window spacing is to reduce the maximum FOV to under 5.5 deg - less than is required for the interceptor mission.

The solution to overcome the FOV limitation introduced by the multi-aperture window is to incorporate in each port a "fish-eye" objective lens to expand the field of view that can be observed through each port. This approach is similar to that used in entry door security viewers.
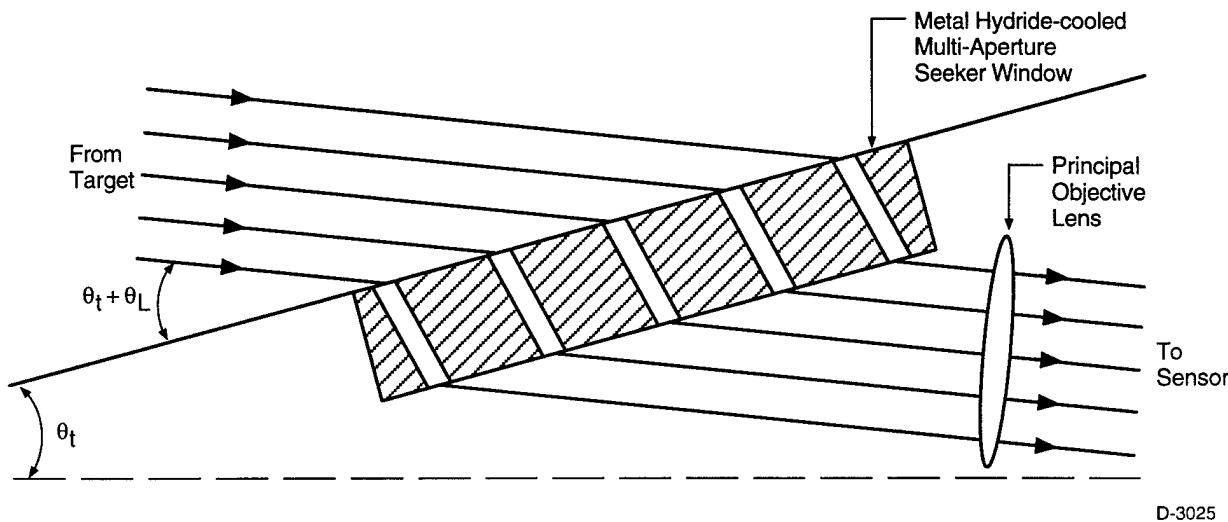
Figure 36. Viewing Constraints Imposed by Requirements for Shallow "Look" Angle Through Multi-Aperture Window Mounted on Shallow Angle Nose-Cone.

Figure 37 depicts the complete optical assembly we propose for each viewing port of the window. It consists of a front beam turning prism for establishing the desired direction of view with respect to the axis of the window port, followed by a relay lens assembly consisting of a front objective lens, a field lens and a final objective lens. After the lens assembly is an optional optical phase corrector (discussed in a later section on spatial resolution) and, finally, a wedge prism.
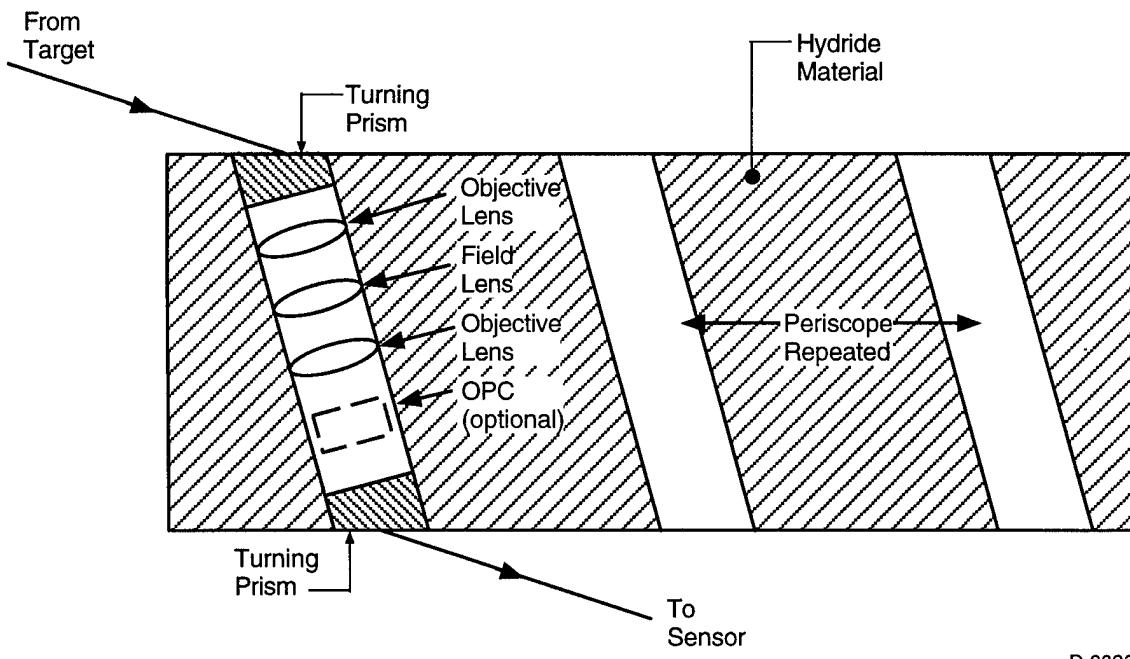
Figure 37. Proposed "Periscope" Optics Design for Metal Hydride-Cooled IR Seeker Window

31

The front beam directing prism serves to establish the desired direction of view while obviating the need for placing optical ports at a highly oblique angle with respect to the cooled window housing. The relay lens assembly serves the function of a miniature periscope establishing the field of view and transferring the view seen from the front end of the "periscope" to the back end. The final wedge prism then directs the port image to the rest of the sensor optical system which ultimately directs the scene image on to the sensor.

It should be mentioned that at an early stage in this study it was thought that an array of infrared fiberoptic lightguides might provide an ideal solution for achieving the necessary image transfer. However, on closer examination, it was found that the state-of-the art in mid-IR fiberoptics is still not adequate to produce a coherent bundle that competes with an image guide utilizing miniature refractive relay lenses. This is particularly true when the application only requires, as does the present one, short, rigid image guides that are several mm or more in diameter. This conclusion is consistent with the fact that the first generation of mid-infrared laparoscopes just now being developed utilize refractive relay lenses rather than IR fiber bundles for the image guide. Of course as mid-IR fiberoptics technology advances it may eventually present a preferred solution.

Total Light Collection Requirements

As indicated above, the diameter of an individual window port in our design is likely to be limited by heat transfer constraints to a rather small effective aperture of < 5 mm. To increase the overall light collection capability, however, an array of several such ports can be used. The total light collection aperture needed will ,of course, depend on the expected background noise level and the desired sensor S/N. While the ultimate reduction in thermal background we can achieve with our proposed approach is not yet known, we can, in the meantime, base a conservative preliminary estimate of the required light collection aperture on the analysis of Reference 3.

In the investigations performed in Reference 3, the performance of an IR optical seeker using an uncooled but cavity recessed window was analyzed. A key conclusion of that study was that with a light collection aperture of ½ in. (1.27 cm) - and f/#5 optics - a sensor system design minimum S/N of 10 could be exceeded for all mission scenarios. Assuming for our design an individual optics diameter of 5 mm, and $\theta_L + \theta_t = 22.6$ deg (see Figure 36), we estimate that a total of about 15 equivalent 5 mm optical ports would be required to yield an equivalent total *projected* aperture for light collection. This is depicted in the sketch in Figure 38 where we have chosen to arrange these ports in a five by three rectilinear array. Further studies, including detailed heat transfer analyses, are required to determine the preferred optimum arrangement and center to center spacing.

It should be noted that for the investigations of Reference 3, considerably higher window temperatures were allowed than are proposed for the cooled window concept we put forward here, and thus higher thermal background noise had to be assumed in that study. For this reason, it is likely that with our approach total light collection requirements would be reduced and, therefore, a smaller total light collection aperture may, in fact, prove adequate. This would, of
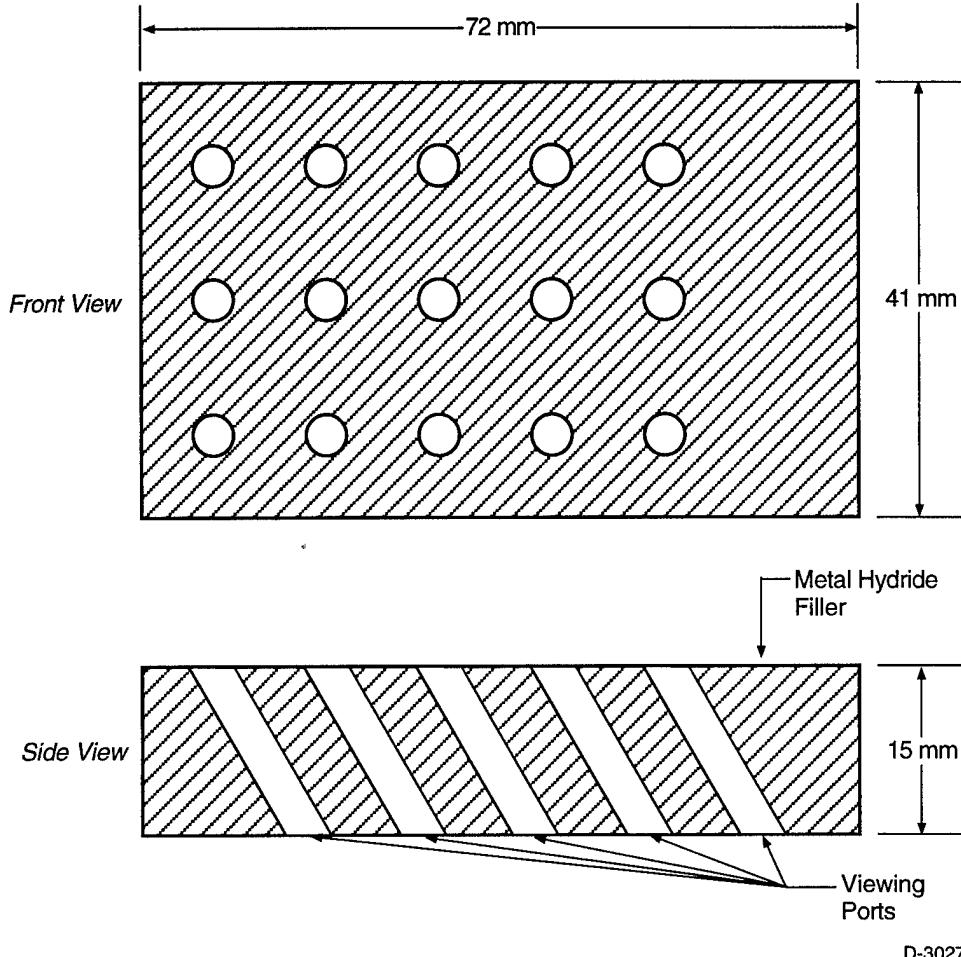
Figure 38. Candidate Multi-Aperture Array Configuration for Rotal Projected Light Collection Area of Approximately 1.2 cm²

course, translate to fewer ports being required in the window assembly than are shown in Figure 38.

Spatial Resolution/Angle Measurement Accuracy Requirements

A final parameter that must be considered in the optical design in addition to field of view and total light collection requirements is that of sensor spatial resolution or, more specifically for the seeker mission, angle measurement accuracy (AMA).

In the LIRIS Endo LEAP study[3] it was indicated that the required AMA for hit-to-kill is ≤ 0.2 mrad. It was also shown that such an accuracy can be achieved, using point spread function (PSF) methods, with a diffraction-limited (Rayleigh criterion) sensor IFOV of only 660 micro-radians and assumed sensor S/N of ≥ 10. This condition was achieved with a limiting optical aperture of 1.27 cm diameter. If for the present design, on the other hand, we were to assume only a single 5 mm light collection aperture, the corresponding Rayleigh criterion limited IFOV

33

would be only 1.7 mrad. By analogy, with such a degraded IFOV, the minimum sensor S/N would have to increase by a factor of 6.5 (S/N > 65) in order to achieve a similar AMA via PSF techniques. With effective window cooling such an increase in sensor S/N may be possible.

Another approach for achieving the desired AMA would of course be to *coherently add the signals from multiple apertures*. This would, in principle, increase the effective limiting aperture for focusing as the square root of the number of individual apertures and, by also increasing the collected light signal, could yield dramatic improvements in sensor performance. Similar techniques are employed in large area array astronomical telescopes.

2.8.4 Design Conclusions

A preliminary optical analysis has been carried out to assess the feasibility of developing a practical IR seeker window design that exploits the proposed metal hydride-based window cooling technique. The zeroth order analysis performed suggests that a window employing an array of small diameter optical ports (probably ≤ 5 mm diameter) is required to enable effective radial cooling of each optical element. In addition, to achieve the required FOV for the seeker mission, each port will likely have to contain, at a minimum, a field-of-view expanding objective lens followed by a short, simple "periscope-like" image guide. A preliminary assessment indicates that, based on the current state-of the-art, fabricating the image guides from refractive optics is preferred to using coherent bundles of IR fibers. The total number of ports or apertures required for the window assembly will depend on the degree of window cooling that can effectively be achieved and on the corresponding improvement in S/N that ultimately results. A preliminary scheme for coherently combining the signals from multiple window apertures has also been examined.

In conclusion, our preliminary analysis suggests that a feasible optical design solution for the metal-hydride cooled IR seeker window appears possible. The next step is to validate this design through more detailed and rigorous optical engineering analyses as well as extensive laboratory performance tests.

34

3. INTERCEPTOR BOUNDARY LAYER TRANSITION CONTROL

3.1 Background

Hypersonic boundary-layer flow control has potentially important applications in atmospheric interceptor technology development. The boundary-layer control could either be laminar or turbulent flow control and it could be used primarily for two purposes: decrease the aerothermal heating load to the interceptor or minimize the optical distortions over the seeker window. At sufficiently high altitudes, the flow over the entire vehicle, including the window, is laminar. In this regime one minimizes aerodynamic heating with proper geometric design and obtains the optimum seeing through the boundary layer over the seeker. In the other extreme at very low altitudes, where the Reynolds number is so large that the flow over the nose of the vehicle and the remainder of the body surface is turbulent, large heating rates and poor optical seeing can result. This study emphasizes the altitude regimes between these extremes where it may be possible to control the location of boundary-layer transition and the concomitant turbulent flow regions.

Our efforts have concentrated upon boundary-layer transition control under situations when the wall of the interceptor remains very cool during atmospheric flight.[5,6] This situation occurs naturally with the use of our "cool window" approach as outlined in the noted references as well as in the previously proposed studies.[7,8] It was found that one could maintain the wall temperature at values near 300 K even though a heat flux of 100 to 200 W/cm^2 was being absorbed by the surface. The physico-chemical behavior of these hydride materials is described in the previous references. This study assumes that such a window material would be available to provide a cold wall boundary condition during the critical 5 to 10 s of seeker operation.

Cooling stabilizes a hypersonic boundary layer under Mach number conditions which fall below the appearance of the second-mode instability. This critical Mach number M_c depends on the Reynolds number or flight altitude. This well-established behavior of supersonic boundary-layers has been used to guide the assessment of boundary-layer transition on a typical atmospheric interceptor geometry from the Atmospheric Interceptor Technology (AIT) program.[9] A simple redesign of the original shape provides lower edge Mach numbers that fall below the critical value.

3.2 Motivation for Boundary Layer Control on Interceptors

Kinetic energy interceptors fly different trajectories depending upon the specific Theater Missile Defense (TMD) mission requirements. The most challenging environmental flight involves high-speed transit in the lower portions of the atmosphere where the boundary layer over the window is turbulent. The overall altitude range of interest is from about 10 to 40 km. Boundary-layer transition movement for a candidate Atmospheric Interceptor Technology (AIT) design[9] is shown in Figure 39 using a typical empirical transition relationship.[10]
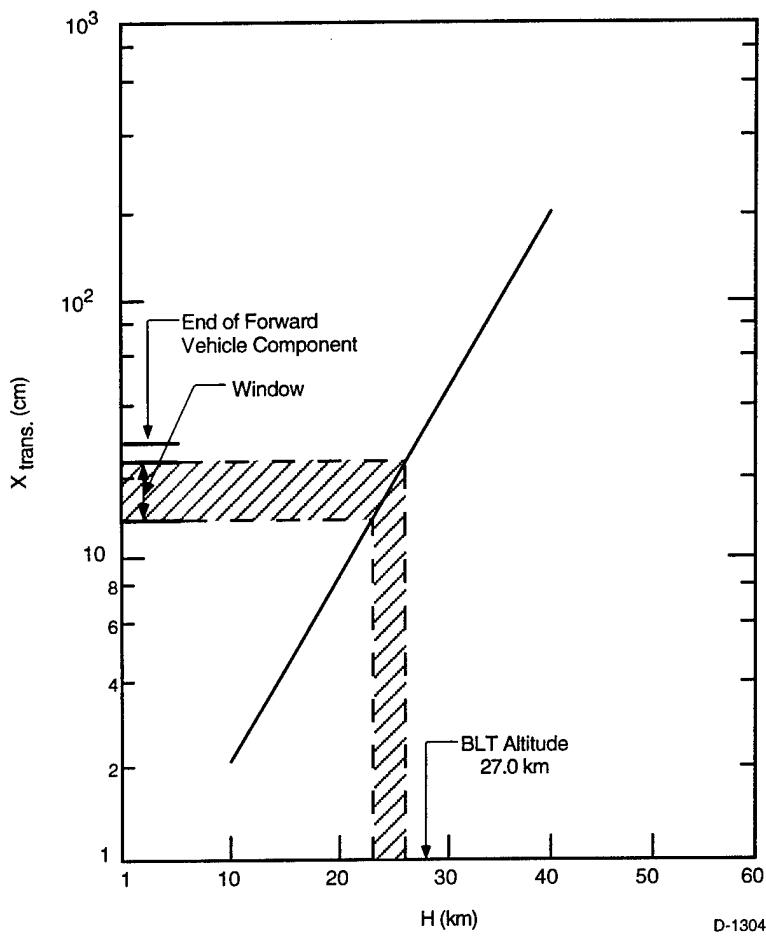
Figure 39. Transition Movement Across the Optical
Window for an M = 15 Interceptor

The window region is shown shaded and the end of the intereceptor is also indicated. The regime of interest here is between about 22 to 25 km and above 27 km, the flow over the vehicle would be entirely laminar. The approximate geometry of the interceptor is shown in Figure 40. Even though the interceptor is predominantly an axisymmetric conical shape, the window region has flat surfaces that make the geometry wedge-like over these regions.

The basic aim of hypersonic boundary-layer control is to move the boundary layer transition location back beyond the end of the window region. From Figure 39, it is evident that at an altitude of 25 km and higher, the window boundary flow is laminar. As the altitude is decreased, however, the turbulent flow initiation moves forward on the interceptor as indicated in the figure. At an altitude of 10 km, a significant increase in the transition Reynolds is required to control transition until aft of the window. The factor (F) improvement needed is nearly 11. This quantity decreases with altitude as shown in
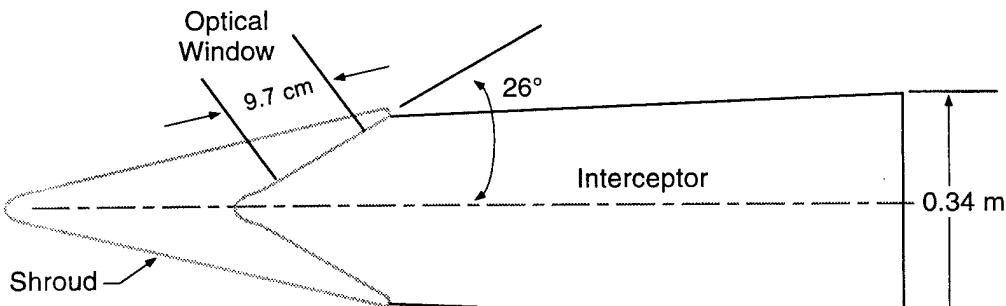
Figure 40. A Candidate Interceptor Geometric Configuration (McDonnell Douglas Design)
from the AIT Program[1]

Figure 41 until at 25 km, it becomes unity.
It will be shown later that cooling the wall
has been demonstrated experimentally with
F factors up to about 4 for Mach numbers of
interest. This would imply from Figure 41
that control could be achieved down to
17 km, at least. The required F factor of
near 11 at 10 km will be much more
challenging. Stability and transition studies
have, however, indicated that complete
control with laminar flow over the window
is manageable.

Approximate window heating rates
over a "typical" interceptor window con-
figuration such as the AIT schematic shown
earlier are provided in Figure 42. Indepen-
dent curves were generated for laminar and
turbulent flow over the window configu-
ration at Mach 15. These were then faired in
at the window-location transition altitudes of
22 to 25 km. These curves suggest that
above 27 km, the laminar heating rates
would be below 200 W/cm^2. At very high
altitudes, the laminar and turbulent heating

Figure 41. Increase in Boundary -Layer
Transition Reynolds Number to Achieve
Laminar Flow Over the Optical Window

rates approach one another; however at altitudes between 27 and 40, if turbulent flow prevailed,
the window heating rates would be significantly higher than the laminar values.

3.3   Hypersonic Stability Results Applicable to Interceptors

Boundary-layer instability and transition analyses have become rather routine under
relatively low-speed, incompressible or, even, subsonic flow situations. At high speeds where
compressibility effects are important, activities have been increasing with Malik[11] following the
pioneering work of Mack.[12] Furthermore, Stetson[13] has recently reviewed the status of
hypersonic stability and transition in a very comprehensive survey. The primary results from
these studies that are applicable to the interceptor problem relate to the "control" of the second
mode instability below a "critical" Mach number. The geometric configuration of candidate
interceptor designs allows for the use of these results.

Three potential means for control of the transition of the hypersonic boundary layer are
wall cooling, boundary-layer suction and wall shaping (favorable pressure gradient). All of these
methods will be examined independently and suggestions regarding their synergistic influence
will also be made. The computational and experimental results utilized to establish a potential
control technique have been taken from the literature. Additional work in this area will require a
detailed computational feasibility analysis and subsequent experimental verification.
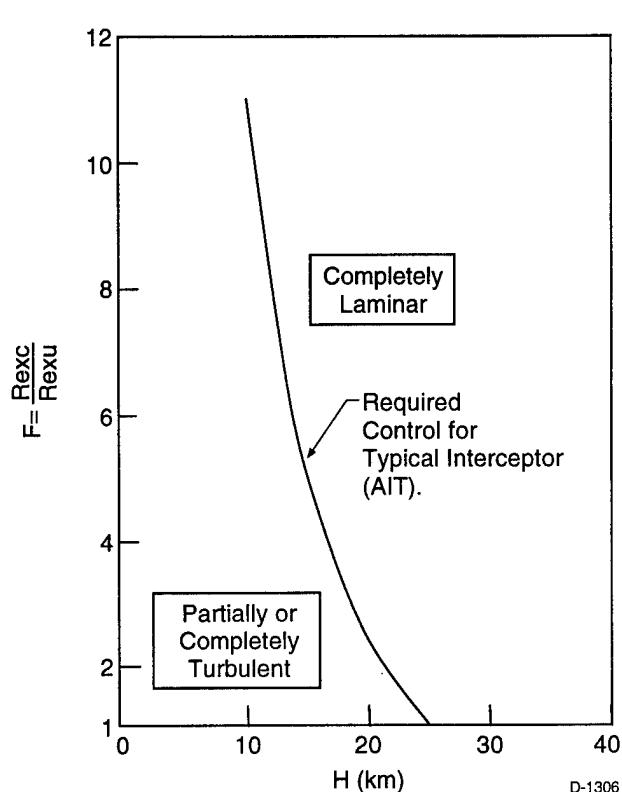
37

Figure 42. Approximate Window
Heating Rates as a Function of
Altitude for the AIT Configuration

We begin with the dramatic appearance of the second-mode instability (Mack[14]) at an edge Mach number near 3.6 as shown in Figure 43. The spatial amplification rates of the maximum first and second mode at an R = 1500 are shown (the length-based Reynolds number, Rx = R^2). Note how critical the value of the edge Mach number is to the appearance of the second mode. Below a value of about 3.6, the first mode decays with increasing Mach number.

The "critical" appearance of the second mode depends upon the edge Mach number and the Reynolds number as shown in Figure 44. The parameter ranges span the region of interest for the current low-altitude interceptor applications. The altitudes corresponding to primarily the Reynolds number are also shown in the figure. The key feature of this chart is that at a sufficiently low Mach number, i.e. below the appearance of the second mode, one can potentially control boundary layer behavior by one of the techniques mentioned earlier. Another way of stating this is that at sufficiently high Mach numbers, the second mode is destabilizing.

Malik[11] states that, "Cooling cannot stabilize the second mode." This point is well illustrated from Figure 45 taken from his paper. Note how the amplification rate decreases with wall temperature cooling for the first mode at Mach 2 and 4.5. The amplification rates become zero at different wall temperature ratios. There is no second mode at Mach 2 and hence, boundary-layer stabilization results, but at Mach 4.5 one observes an increase in the amplification rate and an inability to stabilize the flow. Consequently, if the edge Mach number can be controlled below the "critical value" by geometry shape changes, the stabilization by cooling appears possible. This is the primary theme of this section.

3.3.1 Wall Cooling

A high-speed boundary layer can be stabilized by cooling the wall. The lower temperatures modify the near wall viscosity and thereby promote a stabilizing velocity profile. This stabilizing effect only occurs for the first unstable mode. As described earlier, the second unstable mode is amplified by wall cooling. This behavior is edge Mach number dependent since it depends upon the presence of the second mode. Wall cooling and the appearance of the second mode have been controversial topics in the past. The recent calculations of Malik[11] and some previous experimental surveys by Potter[15] have served to clarify the matter.

38

Figure 43. Maximum First and Second Mode Spatial Amplification Rates at R = 1500 (from Mack[6])

The control of supersonic and hypersonic boundary layers using wall cooling has been demonstrated for simple cone and flat plate geometries as shown in Figure 46 taken from Potter. The cone data reveal factors of transition improvement, F, in excess of 3 as the wall to adiabatic wall temperature ratio is reduced to low values. Such movement is significant as witnessed by Figure 41 where the requirement for the AIT vehicle is given. An F factor of about 11 is needed to yield laminar flow over the window down to altitudes of 10 km.

Other illustrations of the effectiveness of wall cooling are provided in Figure 47 where the transition Reynolds number is given versus the wall temperature ratio. The NOL range data (open squares) at Mach 5 is most interesting. It first reveals an increase in the transition Re until one reaches a very small wall temperature. Subsequent reduction in the wall temperature leads to a dramatic increase in the transition Re; in fact, the flow is laminarized. This is precisely the behavior we would like to produce on the interceptor window.

39
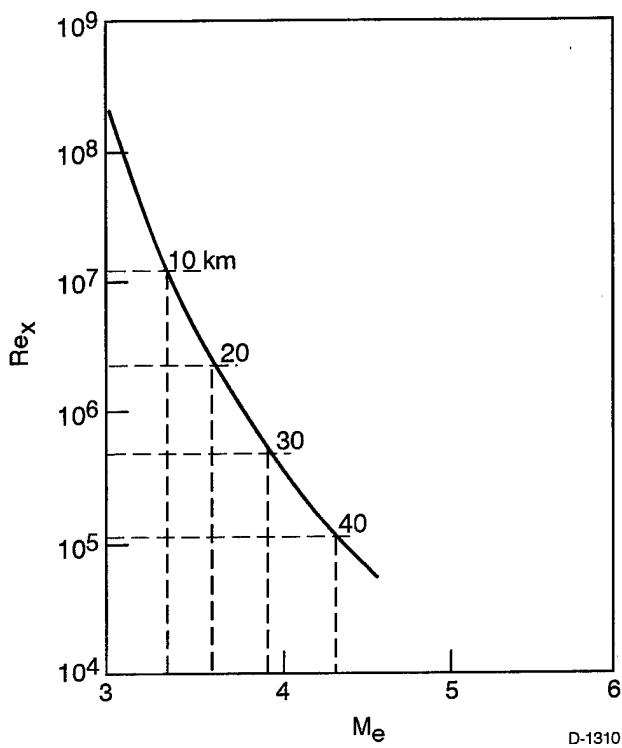
Figure 44. Flow Conditions for the Appearance of the Second Mode (from Malik[11]). Altitudes correspond to AIT vehicle geometry. Critical edge Mach numbers shown.
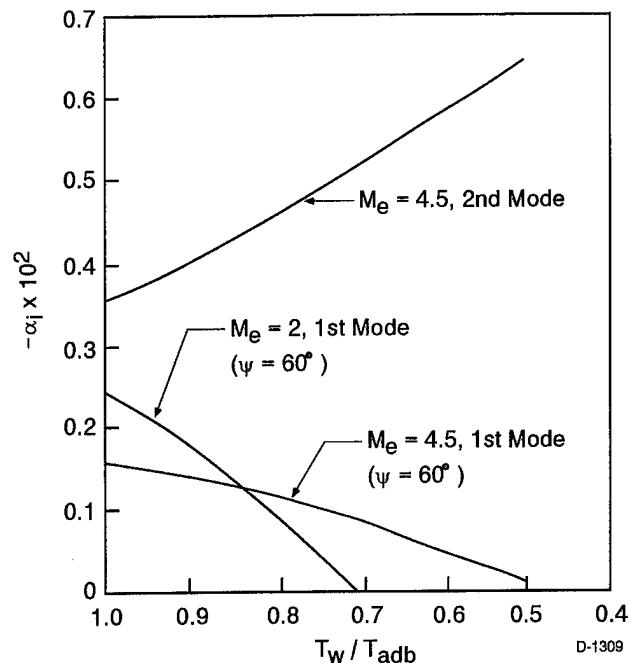
Figure 45. Effect of Wall Cooling on a Flat Plate Boundary Layer at R = 1500 (from Malik[11])
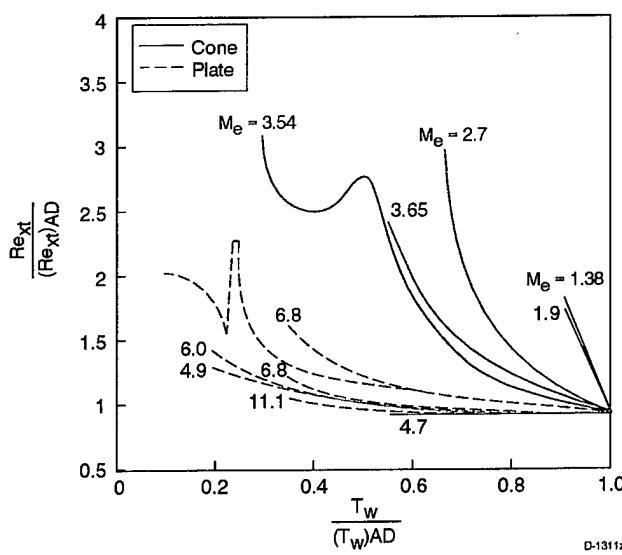
Figure 46. Experimental Data Revealing Control of Boundary-Layer Transition Using Wall Cooling (from Potter[15])
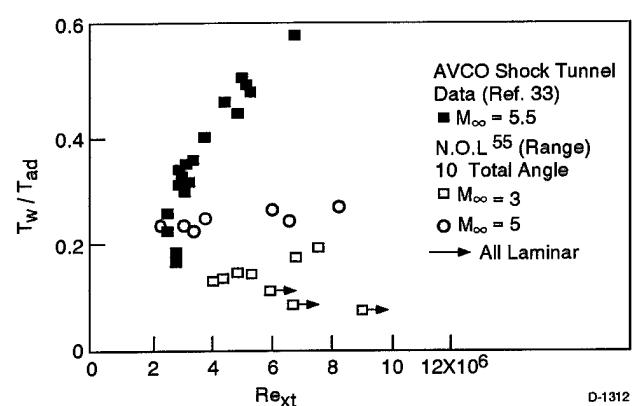
Figure 47. Additional Experimental Data on Effects of Cooling (from Stetson[13])

3.3.2 Wall Suction

Wall suction effectively modifies the velocity profile near the wall and can provide complete stabilization as shown in Figure 48. Specifically, at a value of $f_w = 0.4$, the amplification rate becomes negative resulting in disturbance decay and boundary layer stabilization. The suction requirements for this situation are developed below for the interceptor situation. We begin with the observation from Figure 48 that

$$f_w = \sqrt{2} \; R \; \rho_w V_w / \rho_e U_e = 0.4 \quad . \tag{14}$$
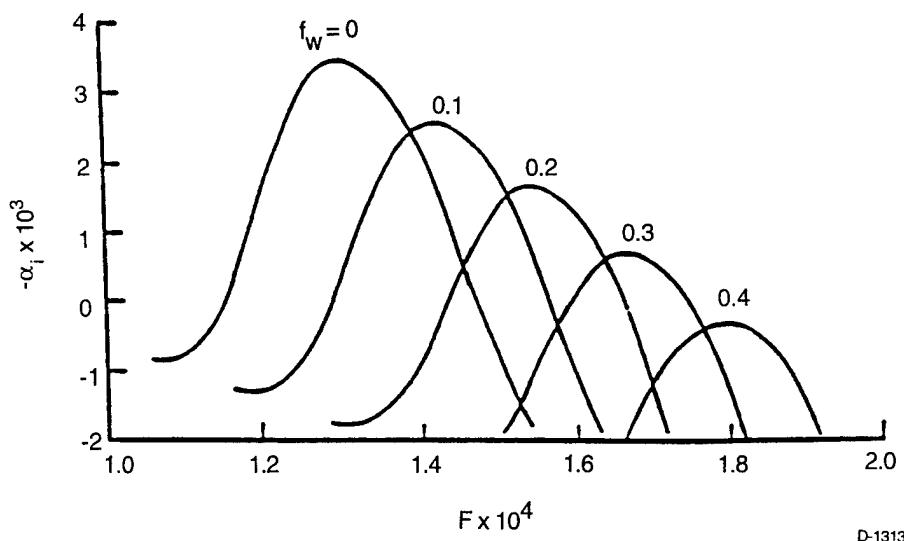
Figure 48. Second Instability Suppression with Wall Suction at Me = 4.5 and R = 1500 (from Malik[11])

This expression can be rewritten to exhibit the required mass flow

$$\rho_w V_w = -0.28 (\rho_e U_e)^{1/2} \mu_e^{1/2} / \ell^{1/2} \tag{15}$$

At 20 km, for the AIT interceptor this becomes a modest flow rate of $\rho_w V_w = -0.038 \; \text{g/cm}^2\text{s}$. The interceptor propulsion system should readily provide such a level of suction. The practical engineering aspects of providing this wall suction above the window area have not been faced, but some of the needed features have been addressed during the discussion of the PSI wall cooling concept in Section 2. The passive wall cooling technique provides a hydrogen gas flow that could be used for boundary-layer stabilization and port cooling purposes. This natural feature of the passive window technique should be exploited.

41

3.3.3 Wall Shaping for Favorable Pressure Gradient

A favorable pressure gradient can also stabilize the boundary layer. Recent calculations by Malik demonstrate the effects very well as shown in Figure 49. As the pressure gradient becomes more favorable, the amplification rate decreases and at a value of $\bar{\beta} < 0.075$, it becomes negative. This implies stabilization of the boundary layer. The quantity $\bar{\beta}$ is the transformed pressure gradient parameter

$$\beta = \frac{2\xi}{U_e} \frac{dU_e}{d\xi}$$

(16)

A value of $\bar{\beta} = 0.075$ corresponds to a velocity exponent $m = 0.0375$ where $U_e = A\xi^m$.
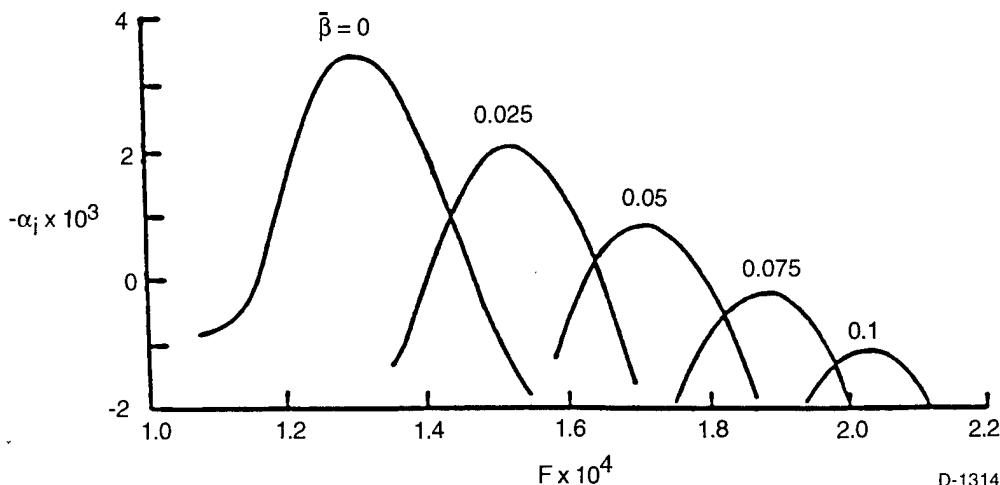
Figure 49. Effect of Pressure Gradient on the Second Mode Instability at Me = 4.5 and R = 1500 (from Malik[11])

Such a velocity distribution can be achieved with an ogival wall contour where the slope of the body decreases with increasing downstream distance. Specific body contours can be generated once stability computations appropriate to actually interceptor configurations have been undertaken. Hypersonic boundary-layer stabilization can certainly be advanced using shaping to provide a favorable pressure gradient. There is, however, a significant difference between the two stabilization techniques just considered: wall suction and favorable pressure gradient and the wall cooling technique. The latter is limited by the occurrance of the critical Mach number for the second mode instability whereas the former two schemes can be applied at higher Mach number since they "eliminate" the second mode. Wall cooling has the opposite effect as shown previously in Figure 44.

3.3.4   BLT Control Using Extreme Cooling

Three potential means to control hypersonic boundary-layer transition for interceptor applications were identified in the previous section. The wall cooling technique is the most interesting since its implementation is most direct. It also connects the PSI Passive Window Cooling Concept (Section 2) with boundary-layer transition control. As described above, high-speed transition control can be achieved with extreme wall cooling if the edge Mach number is below the critical value for the appearance of the second mode instability. The first mode is stabilized with $T_w/T_{aw} \ll 1$. The synergism with the window cooling concept is immediate since one achieves room-temperature cooling and wall temperature ratios $T_w/T_{aw} \sim 0.04 - 0.05$.

The connection between transition and the window cooling scheme is represented in Figure 50 where wind tunnel and ballistic range data provide transition factor F improvement as a function of wall cooling ratio. In addition, the extremely low wall cooling ratio achievable with the window cooling scheme is shown. The potential for complete laminarization is evident. As mentioned earlier, this wall cooling approach will only work if the edge Mach number is relatively low, i.e., below the values shown in Figure 45.

The edge Mach numbers of interest are so low that they could not be achieved with very slender hypersonic vehicles characterized by relatively small cones angles. They can, however, be achieved by the AIT candidate interceptors which have relatively large cone angles as shown in the geometry sketch (c.f. Figure 40).

Figure 50. PSI Window Cooling Concept in Relation to Existing Experimental Data on Wall Cooling.

This point is illustrated for sharp cones and wedges in Figure 51 taken from NACA 1135.[16] Note that at a nominal free-stream Mach number of 15, the required edge Mach numbers between 3 and 4 can readily be achieved. The AIT interceptor has a flow deflection angle of 23 deg which is in the middle of the range shown in the figure. It is also important to remember that since the nose radius of the interceptor is relatively large, entropy layer effects will reduce the Mach number below the values indicated in Figure 51.

43

Figure 51. Sharp Cone and Wedge Edge Mach Numbers for Deflection Range of Interest

3.4 Conceptual Design for Boundary Layer Control

The external geometric design of atmospheric interceptors depend upon three coupled disciplines: the external flowfield, the window characteristics, and the thermal protection materials and their response. Various elements of these disciplines for interceptor design are summarized in Figure 52 which focuses upon the coupling between the disciplines.

Consider first the external flowfield of the entire configuration. In general, it depends upon many different parameters. It is basically a three-dimensional flowfield since the interceptor is oriented at significant angle of attack near the end-game. High heating rates provide net surface heat flux values that can lead to
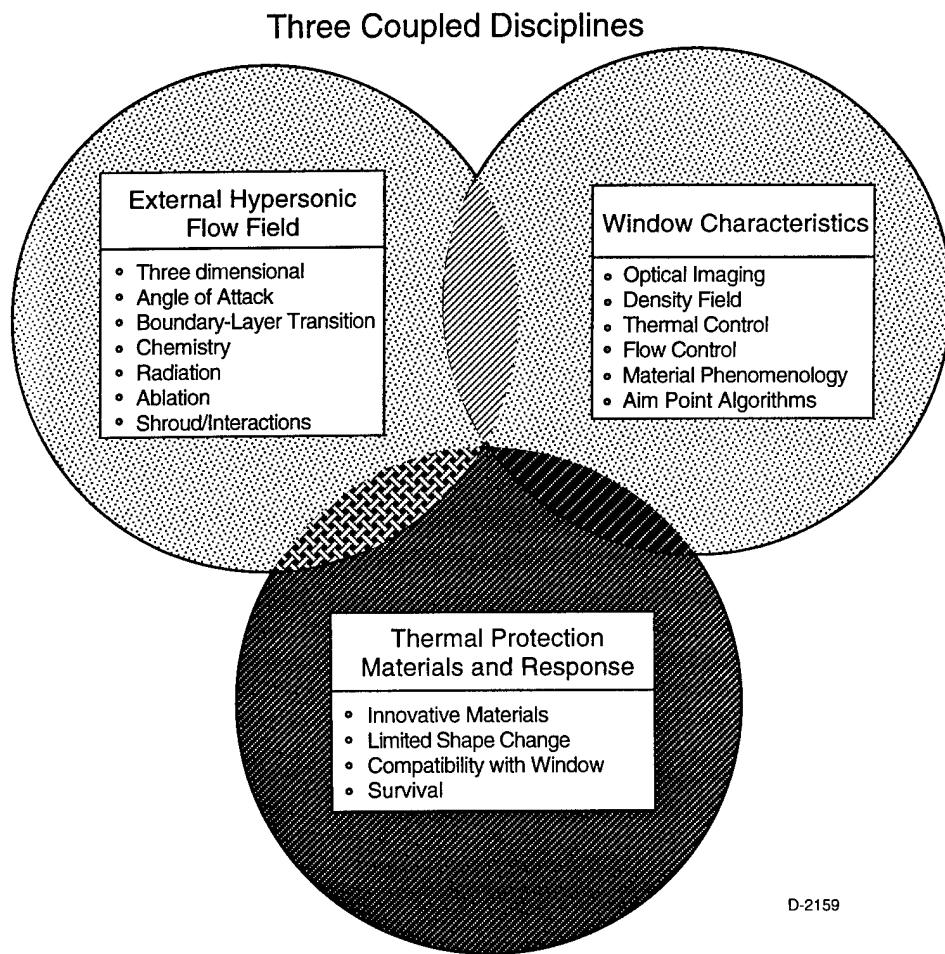
Figure 52. Interceptor Design Issues

44

material mass removal via ablation mechanisms. The propensity to do this depends upon the surface materials employed on the interceptor. These materials have to be compatible with the window material, i.e., limited ablation materials are desired upstream of the window. The window material requires thermal control, a good density field to promote optical seeing and non-interference from neighboring material ablation behavior. The local flow over the window can also influence the external hypersonic flow if the disturbances are significant.

Candidate interceptor designs with window (or seeker head) geometric configurations are shown in Figure 53. These are from the AIT effort. The configuration in the upper left is from McDonnell Douglas, whereas the one in the lower right is from Lockheed. Both designs have a relatively flat window embedded in a multi-faceted three-dimensional geometry.
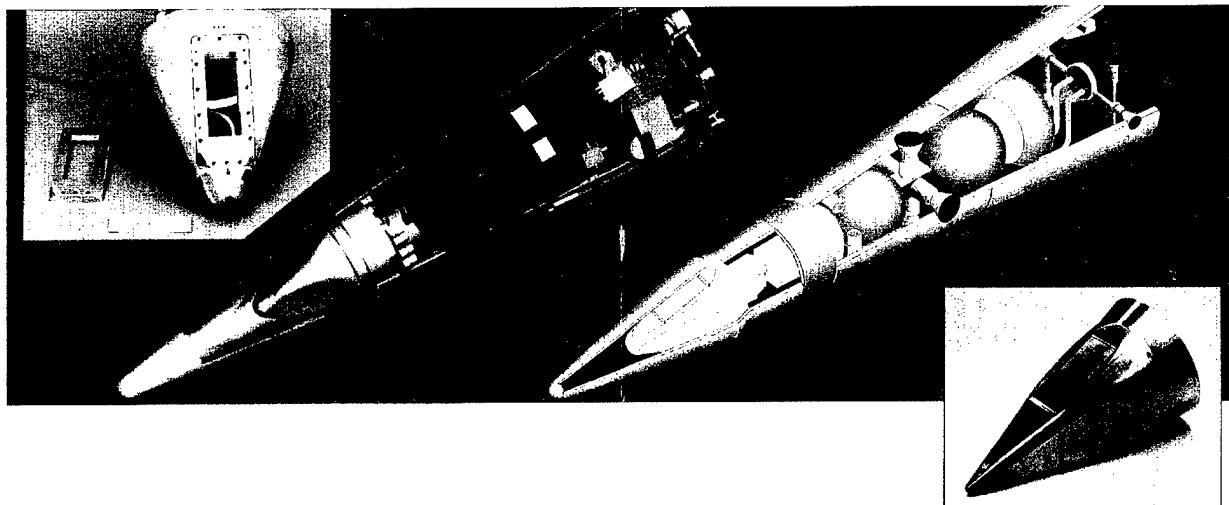
Figure 53. Window Configurations

We have perturbed the McDonnell Douglas schematic design shown in Figure 40. The sketch is the cross-section of the three-dimensional seeker geometry. The front part of the interceptor is wedge-like on four surfaces with one of the facets containing the window. The approximate dimensions of the geometry are shown in the figure including a wedge angle of 23 deg. If this design were not changed, the edge Mach number would exceed the critical value and stabilization by extreme cooling would not work.

If the wedge angle in Figure 40 were increased to 26 deg, then the aforementioned stabilization would work. In order to accommodate the same shroud we shift the nose region backward. This minor loss of volume will have an insignificant impact on interceptor or seeker functions. The edge Mach number for a 26 deg window angle is below the critical Mach number for the presence of the second mode instability over the interesting altitude range between 10 and 40 km. This implies that the passive cool window/boundary stabilization control even works at

45

the very low altitudes where window cooling is a potential problem. The HITT program[17] out of USA-SMDC may have use for such a system. Since a functioning hydride window concept is assumed, the release of H_2 gas must be well designed to not interfere with the window flow. It can be plumbed to enter the flowfield downstream of the window.

The computed wall temperature ratio for two candidate hydrides are shown in Figure 54 as a function of surface heat flux. These results are representative and have not been optimized for maximum cooling. Additional configurations of the hydride bed could lead to similar values of the wall temperature ratio at higher surface flux levels. Experiments are desperately needed to confirm the validity of the hydride window cooling concept. For now, we will assume that they have the capability to achieve temperature ratios between 0.04 and 0.05.
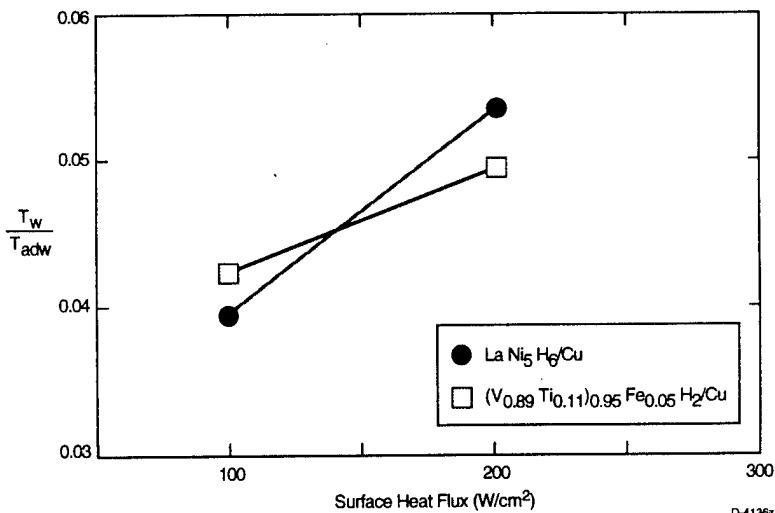
Figure 54. Computed Wall Temperature Ratios for Two Candidate Hydrides

The requirements for stabilizing supersonic and hypersonic boundary layers have been demonstrated previously for rather simple geometries such as cones and flat plates in wind tunnels and ballistic ranges. These results were summarized in Subsection 3.3.1. There is also a unique flight test of stabilization by wall cooling (organized by Joe Sternberg after WW II) of a captured V-1 rocket that led to the highest transition Reynolds number ever measured. Although this flight experiment is very interesting, the ground test data is characterized more thoroughly. In Figure 46 experimental data organized by Potter[15] shows the increase of the transition Reynolds number as the wall temperature is decreased. Note that cooling is more effective for cones than flat plates and that there is a stabilizing effect for even minor cooling. Furthermore, the edge Mach numbers effective cooling are rather low, i.e., up to Me = 3.65. This value is in the neighborhood and below the critical Mach number mentioned earlier. If one extrapolates this data, one would achieve about a factor of four increase in the transition Reynolds number at extreme cooling wall temperature ratios achievable with the "cool window" technique.

In other environments the behavior is not so direct. An assessment by Stetson[13] has shown that transition reversal occurs over a very narrow range in wall temperature ratio, i.e., between 0.2 and 0.1 for Mach 3 ballistic range experiments of cones. From these studies one can expect transition control for all cooling ratios in the current interceptor study with the maximum effectiveness at the extreme cooling values. It also suggests that boundary-layer transition would also be potentially effective under situations of higher heating rates in the order of 1000 W/cm^2 if the passive window can provide some cooling. This is a very important point since there are

46

no easy solutions for very low altitude interceptors under high heating environments. This relates back to the HITT program.[17] The stability assessments were done for a wall temperature of 300 K.

The design concepts for the flow-controlled interceptor window depend upon the edge Mach number M_e of the window flow. More specifically, the design concepts change dramatically whether or not M_e is greater than or less than the edge Mach number corresponding to the appearance of the second-mode instability.[11,14] This critical Mach number is a function of the local flow Reynolds number and will be identified as M_{e2}. Consequently, two design paths are possible. When $M_e < M_{e2}$ wall cooling can be used to stabilize the hypersonic boundary layer. Alternatively, when $M_e > M_{e2}$ wall cooling is destabilizing, but boundary-layer suction and use of favorable pressure gradients can be employed to control the flow. Based upon stability calculations performed in the literature, the critical boundary can be determined as a function of Reynolds number or altitude. The critical value M_{e2} varies in a fairly narrow range between 10 and 40 km as shown in Figure 55.
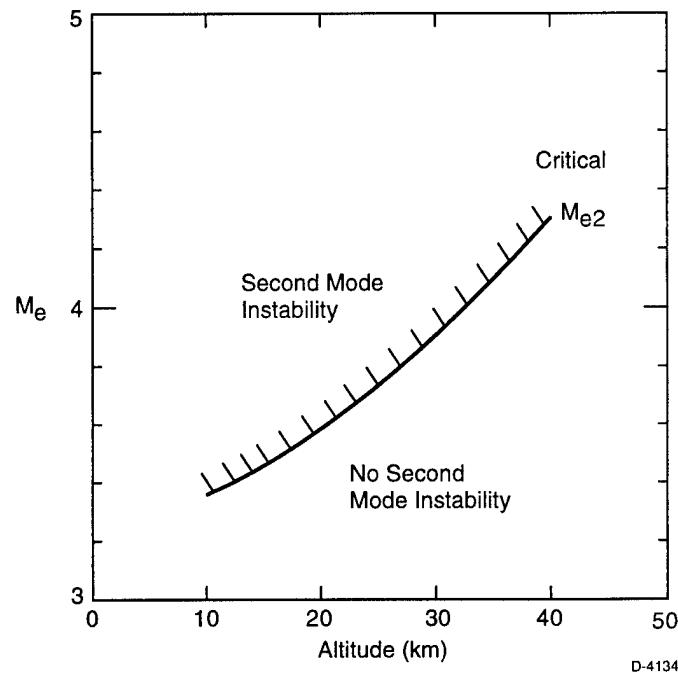
Figure 55. Critical Edge Mach Number for the Appearance of the Second-Mode Instability

The relationship between Reynolds number and altitude necessitates the definition of a length scale, i.e., the distance from the nose of the interceptor to the beginnng of the seeker window. This has been used to generate the critical boundary. This is based upon ideal gas approximations involving no chemical reactions. The potential influence that chemistry plays on the definition of the critical boundary is an open question. Candler[18] is investigating such issues as part of his CFD research program at the University of Minnesota.

There is a direct relationship between M_e and the flow deflection angle. The flat, wedge-like flow geometries over the window lead to values of M_e as shown in Figure 56 for wedge deflection angles at $M_\infty = 15$. These ideal gas results were taken from NACA 1135. As the deflection angle increases, M_e decreases and at sufficiently high deflection, M_e remains below the critical value over the entire altitude range. This occurs at an angle of 26 deg. The angle exceeds the "design" value for the McDonnell Douglas version of the AIT interceptor configuration by 3 deg. This design will be described in some detail later.

Although the interceptor will experience additional heating due to the higher wedge angle over the window region, the potential maintenance of laminar window flow over the entire

47
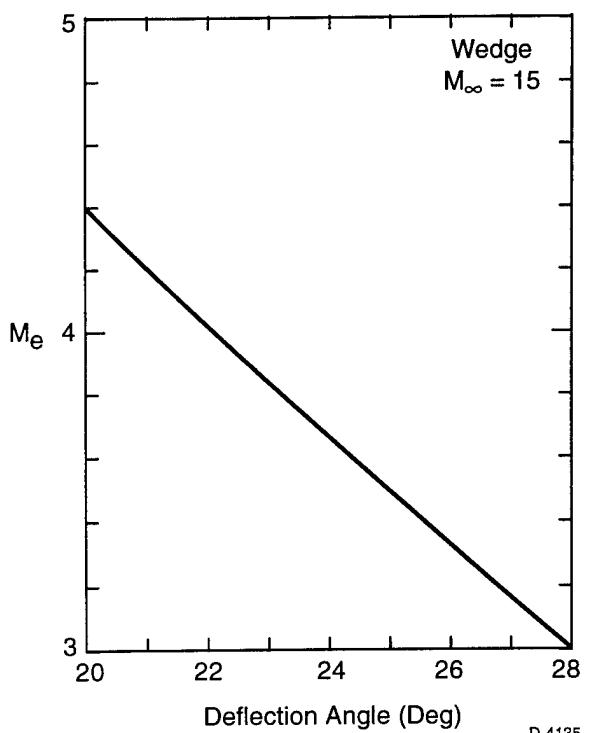
Figure 56. Dependence of M_e on Deflection Angle for a Wedge at Mach 15

altitude regime will offset this effect. Furthermore, we anticipate utilizing the synergism with the "cool" window approach employing hydrides to establish very low wall temperatures. The appropriate temperature ratio is the wall to adiabatic wall temeprature T_w/T_{adw} which varies from 0.038 to 0.053 for the range of heat flux considered. The quantitative results from the cool window analytical study (Section 2) were already summarized in Figure 54 for different hydrides. Note that the H_2 that is released can be vented into the boundary-layer flow downstream of the seeker window.

The approach envisioned is to perturb the McDonnell Douglas AIT design[19] shown schematically in the upper part of Figure 57. The sketch shown is the cross-section of the three-dimensional seeker geometry that is also displayed in the figure. The front part of the interceptor is wedge-like on four surfaces. Approximate dimensions of the window on one of the flat faces are also indicated. The wedge angle is 23 deg. If this design were not changed, the edge Mach number would exceed the critical value and stabilization by extreme cooling would not be possible. The approximate location of the conical protective shroud is indicated by the dashed line.

The perturbed window geometry is provided in the lower part of Figure 57 with the wedge angle increased to 26 deg. The nose region is shifted backward in order to accommodate the same shroud configuration. Is the minor loss of volume significant for seeker/interceptor functions? We will not be concerned with this overall system issues at the present time, but there could be changes in thermal protection material thicknesses due to the geometry change. Furthermore, venting of the H_2 must also be considered since our cool window approach releases this gas during its operation. In order to avoid perturbing the BLT-controlled flow, it is important to vent downstream of the corner on the conical part of the interceptor as indicated in the figure.

The potential control of boundary-layer transition utilizing extreme wall cooling is very attractive due to the synergism with the PSI cool window concept, but the need for low edge Mach numbers limits the flight speed for which this scheme can be used. There are, however, alternative flow control techniques that can be used at higher M_e when the second-mode instability occurs. Two schemes that have been evaluated under hypersonic conditions[11] are boundary-layer suction and pressure gradient. Since the formation of a pressure gradient on the surface of the interceptor requires a substantial surface geometry change over the window region, it has not be considered from a conceptual design point of view.

48

Figure 57. Interceptor Schematic Designs and the Three-Dimensional Seeker Geometry

Boundary-layer suction seems like a more likely alternative candidate for BLT control since the suction system can help to redirect some of the evolved H_2 away from the surface. This is important since gas evolution or blowing into a hypersonic boundary layer destabilizes the flow and makes it more prone to transition to turbulence. It is for this reason that the hydrogen was vented downstream of the window region on the conical surface in the lower schematic of Figure 57. The suction characteristics can also be made compatible with the window "seeing" characteristics. In addition, since the interceptor is rocket and control-jet powered, there exists significant power to pump air and the relatively small hydrogen flow.

The boundary-layer suction required to stabilize the boundary-layer flow at $M_e = 4$ is shown in Figure 58 as a function of altitude. Stability calculations by Malik provided the suction requirements needed to stabilize the flow.

3.5   Computational Assessment of BLT Control

Flow control over interceptor surfaces are important for reduced heat transfer to thermal protection surfaces and improved seeing through the optical seeker windows. Our particular emphasis is upon window flow control in this study. Consequently, a laminar flow is the desired flow state over the window region. Although the results from the literature[1] indicate that this may be possible for the basic geometric configurations of current interceptor designs as outlined in the previous section, detailed computational assessments are necessary to confirm these suppositions. This proceeds in two steps. Complete fluid dynamic solutions are required over the surfaces of interest followed by an assessment of the stability and transition characteristics of the flow. Both of these aspects are described in this section.

49
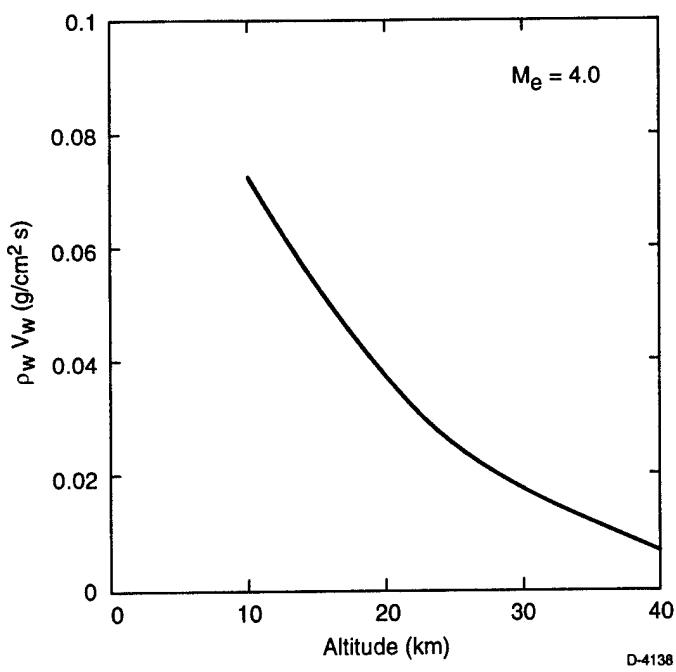
Figure 58. Boundary-Layer Suction Requirements
for Stability at $M_e = 4$

3.5.1 Flow Configurations

Flow control is desired over interceptor surfaces under high Reynolds number (low altitude) situations typical of future advanced systems. Furthermore, the cooled window approach provides for a very low wall temperature for a high-speed atmospheric vehicle. The nominal flow conditions are summarized in Table 2.

Since the complete geometric configuration is a complicated three-dimensional shape, a sequence of geometric configurations should be evaluated. Four of these are shown in Figure 59. The first configuration (a) is simply a wedge with the appropriate wedge angle for second-mode stability. The window location is shown in the schematic. The second configuration (b) remains two-dimensional, but adds streamwise curvature to the wedge. The third configuration (c) is mildly three-dimensional adding leading-edge curvature to the basic wedge shape in two dimensions. The fourth configuration (d) is fully three dimensional and represents a flat surface intersecting a conical-type surface (c.f. Figure 57). The flow solutions for the basic wedge and the complex three-dimensional geometry have been obtained.

Table 2. Nominal Flow Conditions

Altitude	20 km
Mach Number	15
Wall Temperature	300 K (range is 260 to 400 K)

3.5.2 Wedge Flow

The hypersonic flowfield over the basic wedge geometry was generated at the University of Minnesota[19] by Heath B. Johnson, who is a graduate student in Prof. Graham Candler's group. They utilized their latest CFD solver to handle this two-dimensional flow and the three-dimensional flow discussed in the next section. The 2D or 3D Navier-Stokes equations are solved with an implicit finite-volume method that uses upwind evaluations of the fluxes. The method[20,21] is first-order accurate in the body-normal direction, and second-order accurate in both the axial and circumferential directions. The Data-Parallel Lower-Upper Relaxation Method is used to solve the system of equations that results from the implicit time integration method. The code has been implemented on the massively parallel Thinking Machines CM-5, so that very large computational grids can be used to obtain accurate mean flow solutions. Typical grids have
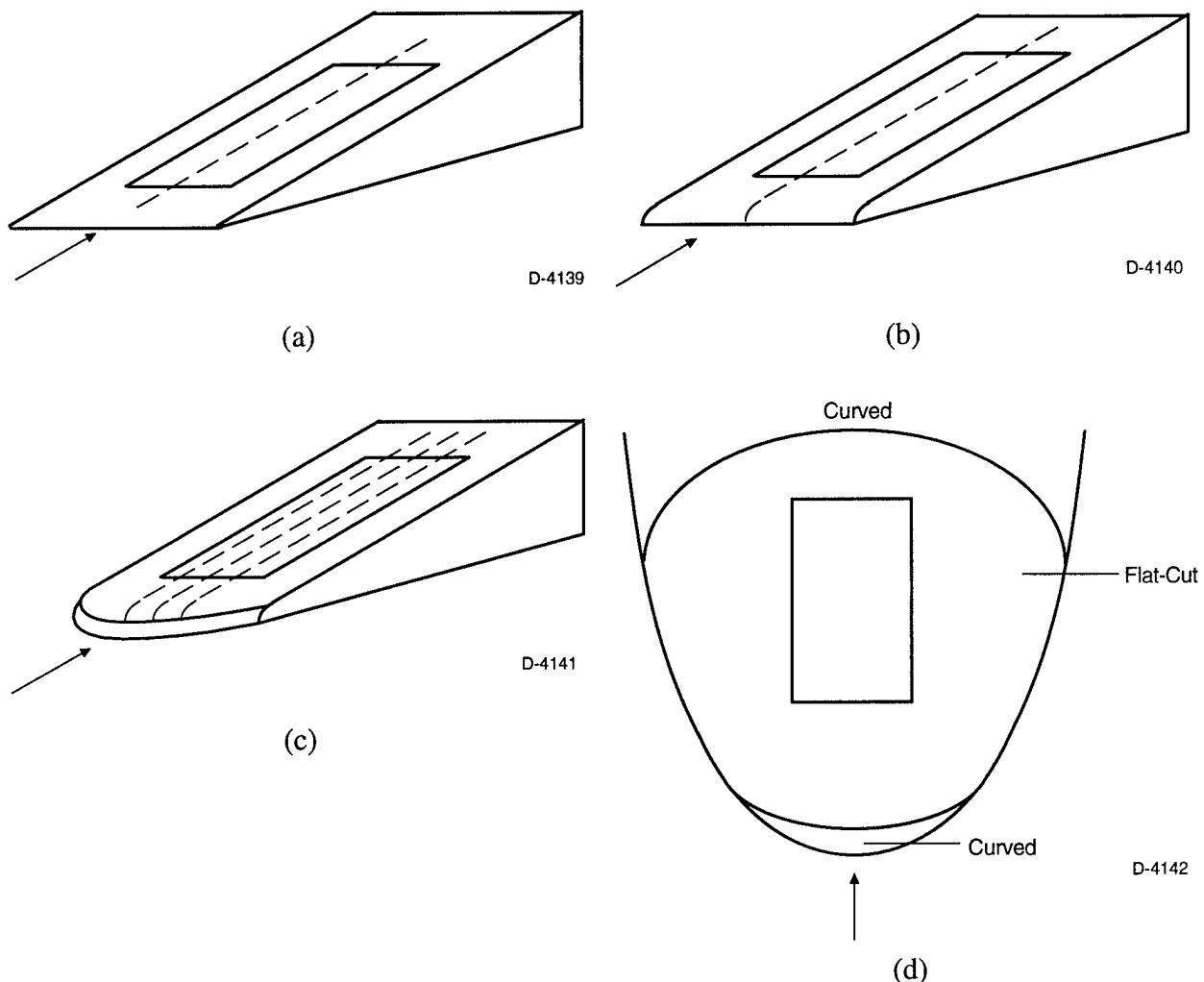
Figure 59. Modeling Configurations

at least 100 grid points in the boundary layer to assure adequate resolution of the gradients. When the effects of finite-rate internal energy relaxation and chemical reactions are included, the governing equations are extended to include conservation equations for each chemical species and internal energy. The extended set is solved with the same numerical method.

The geometry of the wedge is closely related to the geometry of the AIT[11] configuration described in Subsection 3.4. The specific sharp wedge configuration as well as a rounded wedge shape is provided in Figure 60. Recall that the wedge angle of 26 deg is a slight modification from the wedge angle of a candidate AIT design which is 23 deg. The purpose of the modification is to reduce the edge Mach number below the critical second-mode instability Mach number M_{e2} as illustrated previously in Figure 55. Computational results were only obtained for the sharp wedge case. The rounded wedge will be explored in future studies.

51

Sharp Wedge

163 mm

81.8 mm

Window

93.6 mm

26°

191.9 mm

Rounded Wedge

163 mm

81.8 mm

Window

93.6 mm

26°

$R_n = 23.4$ mm

161.92 mm

D-4143
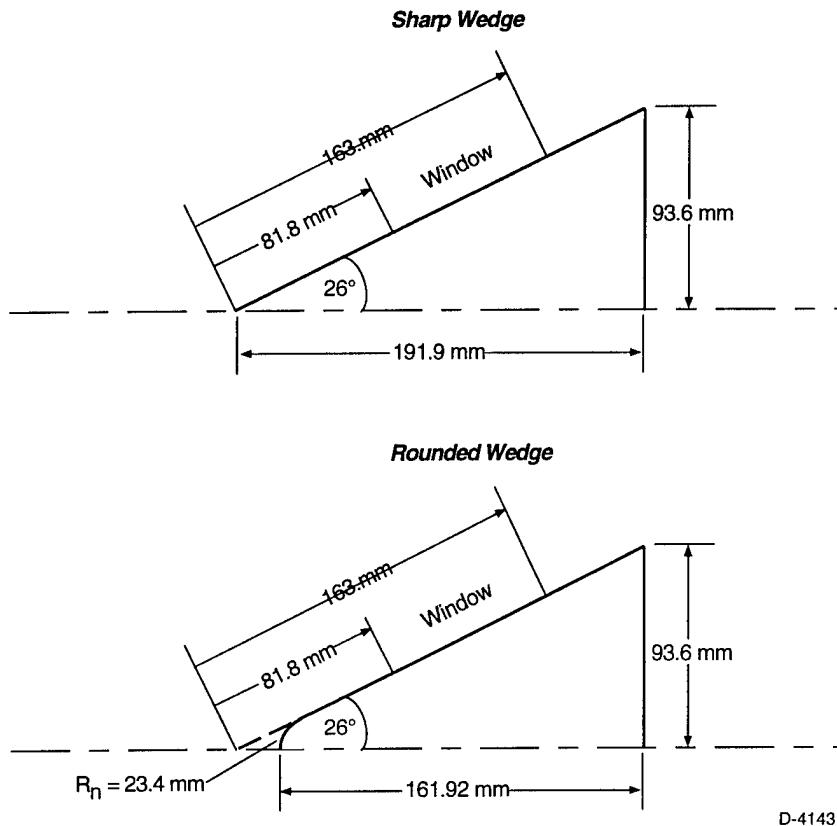
Figure 60. Sharp and Rounded Wedge Geometry

The results of the perfect gas calculations for flow over the 26 deg wedge are described below for converged solutions employing a 128 x 256 grid. Boundary-layer velocity and temperature profiles for this case are provided in Figures 61 and 62.

The edge velocity for the wedge case was nearly 3.8 km/s and the corresponding temperature profile provided a maximum temperature exceeding 3000 K. The boundary layers at these high Reynolds number conditions are very thin. For example, the maximum temperature point in the boundary layer is only 25 microns from the surface! This is evident from the temperature contours of the wedge flow shock layer shown in Figure 63 where it is not possible to distinguish the thin boundary layer.

3.5.3   Three-Dimensional Flow

The seeker head geometry of the AIT interceptor is significantly more complex than the wedge geometry. The initial assessment of the configuration led to the contour specification found in Table 3 where the Contour ID is shown in Figure 64. The geometry was deduced assuming that the geometry was the result of the intersection of a plane and a blunted cone. An alternative and essentially similar contour was actually used in the CFD simulations.
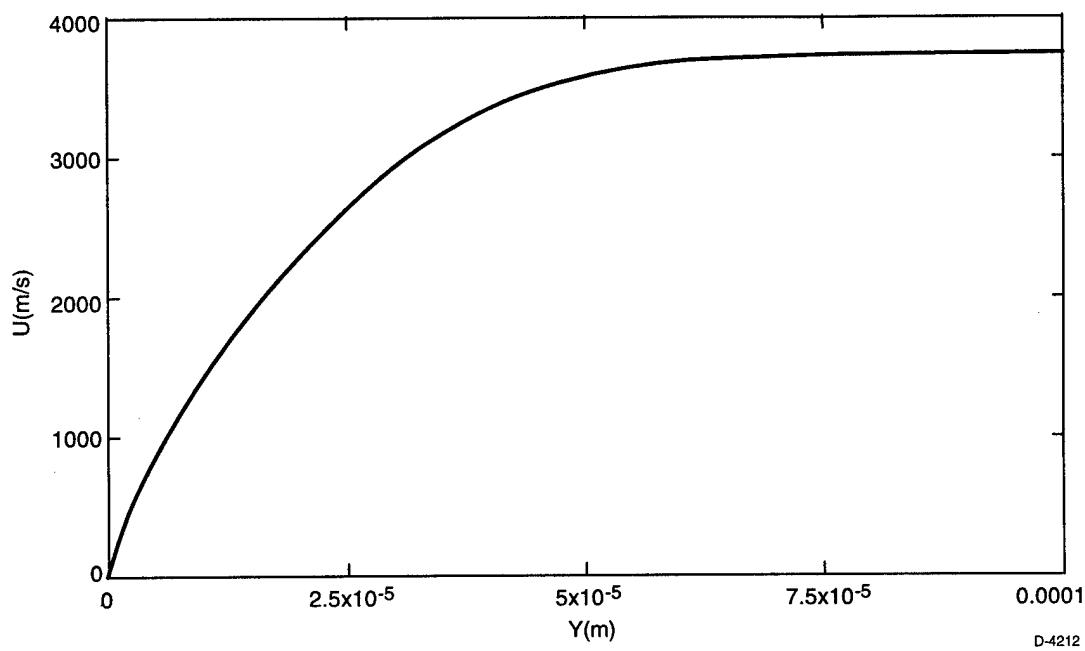
Figure 61. Velocity Profile for Wedge Geometry
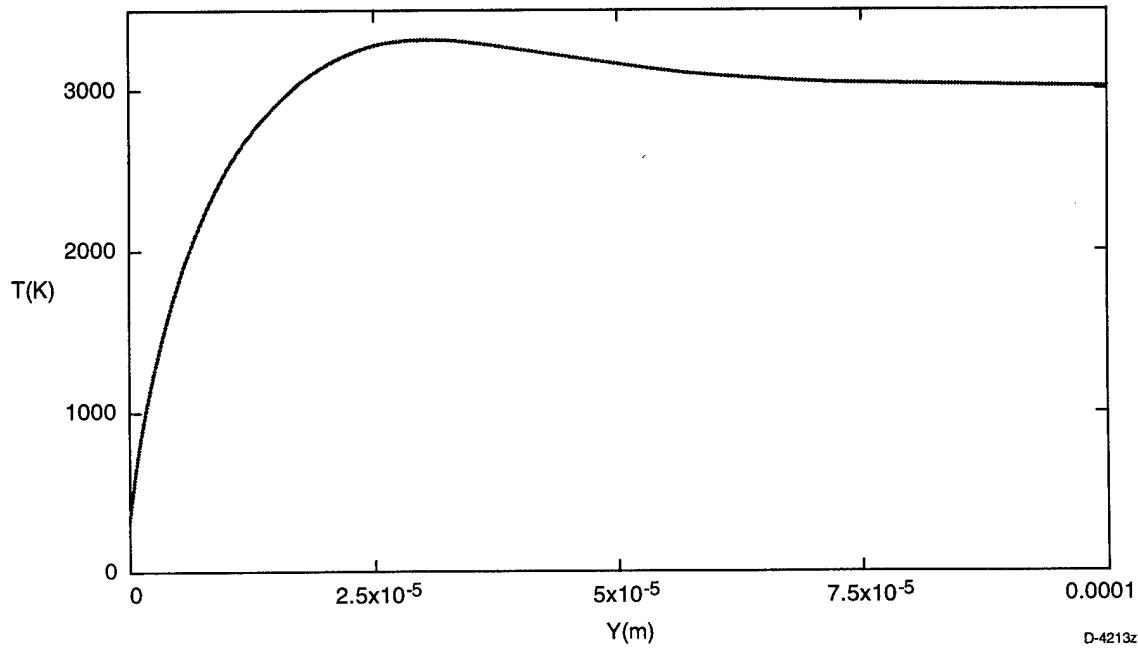
Figure 62. Temperature Profile for Cold Wall, Wedge Boundary Layer

53
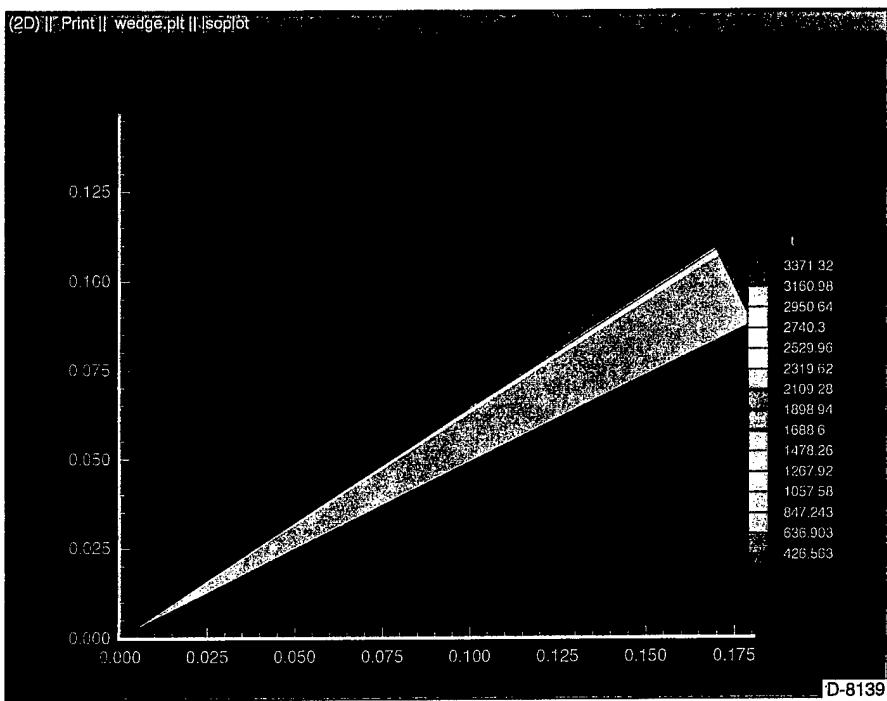
Figure 63. Wedge Temperature Contours

An alternative representation of the three-dimensional geometry can be developed by considering the basic configuration of the interceptor front-end to be a biconic or perhaps even a variable angle axisymetric shape. If one uses such an approach, then the flat zone accommodating the window can easily be incorporated into the geometry. The definition of the geometry is shown in Figure 65 where a biconic with angles of 34 and 6 deg has been used and the wedge angle of 26 deg is also shown.

Heath Johnson provided some postscript pictures of this latter geometry. The first two-thirds of the body is generated by the 34 deg cone angle and the remaining third is characterized by a 6 deg cone angle. The first cone intersects the blunted nose smoothly with a nose radius of 23.4 mm. Three pictures are provided. The front view is shown in Figure 66; the side view is given in Figure 67 and the window view is given in Figure 68. Although it is difficult to interpret these two-dimensional images of a three-dimensional shape, the side view (Figure 67) bears a fairly close resemblence to the photograph insert of the AIT configuration in Figure 57.

A linear-stability code is used to evaluate the stability characteristics of the mean flow. The code employed is the compressible linear stability code: eMalik3d.[22] It is employed for N-factor calculations for fully thee-dimensional flows. The code employs quasi-parallel stability theory and considers both crossflow and Tollmien-Schlichting (TS) disturbances. The TS instability is viscous instability at low Mach numbers, but has an inviscid character when the Mach number increases due to a generalized inflection point in the profile of the density-velocity gradient product. As mentioned previously, this mode can be stabilized by wall cooling as well as by suction and pressure gradient. The inflectional nature of the cross-flow velocity profile

54

Table 3. 3D Geometry Definition

Contour ID	Slant (mm) Length*	Radius (mm)	Flat (mm)	Window (mm)
3.6	46.30	20.30	0.0	
4	51.45	22.55	7.72	
5	64.31	28.19	23.15	
6	77.17	33.83	33.44	
6.36	81.80	35.86	36.01	25.72
7	90.03	39.47	46.30	25.72
8	102.89	45.10	56.59	25.72
9	115.75	50.74	64.31	25.72
10	128.61	56.38	69.45	25.72
11	141.47	62.02	69.45	25.72
12	154.38	67.68	66.88	25.72
12.74	163.80	71.81	65.20	25.72
13	167.20	73.30	64.31	
14	180.06	78.93	56.59	
15	192.02	84.57	46.30	
16	205.78	90.20	23.15	
16.6	213.50	93.60	0.0	

Notes for table:

*The slant length location is based upon the sharp 26 deg wedge.

The radius is the conical radius at that slant location, i.e., (sin 26) x (slant length).

The flat is the length of the flat region taken from the photograph.

The window dimensions are also shown.
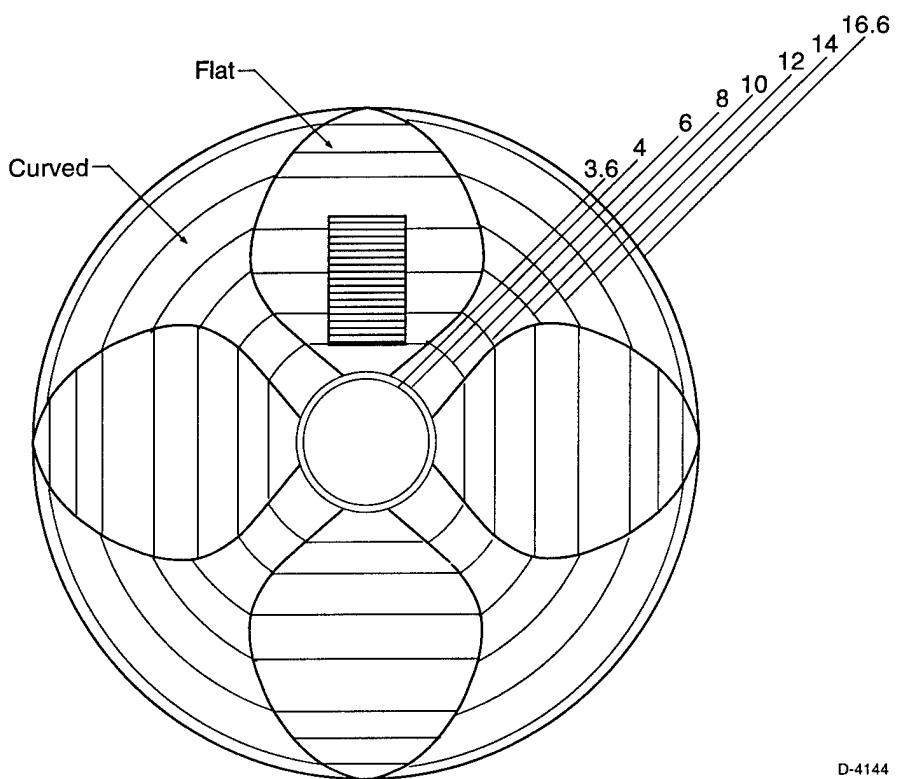
Figure 64. Head-on View of the Seeker-Head Geometry and the Identification of Contours

All lengths are in inches.
All angles are in degrees.

Nose rad	L1	L2	L3
0.921258	1.47	2.20	2.3

Theta 1	Theta 2	Theta 3
34.00	34.00	6.00

Theta 4	Z intercept
26.0	-2.10

Base Geometry

Window Plane
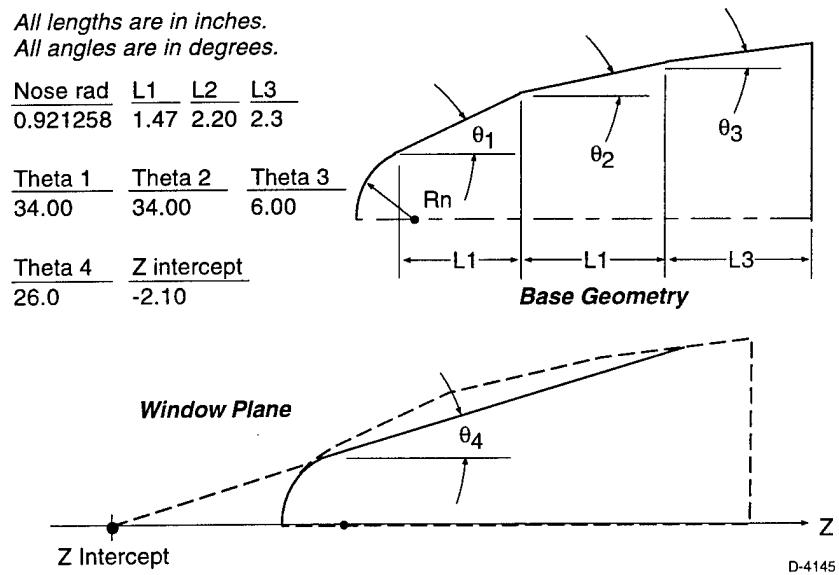
Figure 65. Modified Biconic Geometry
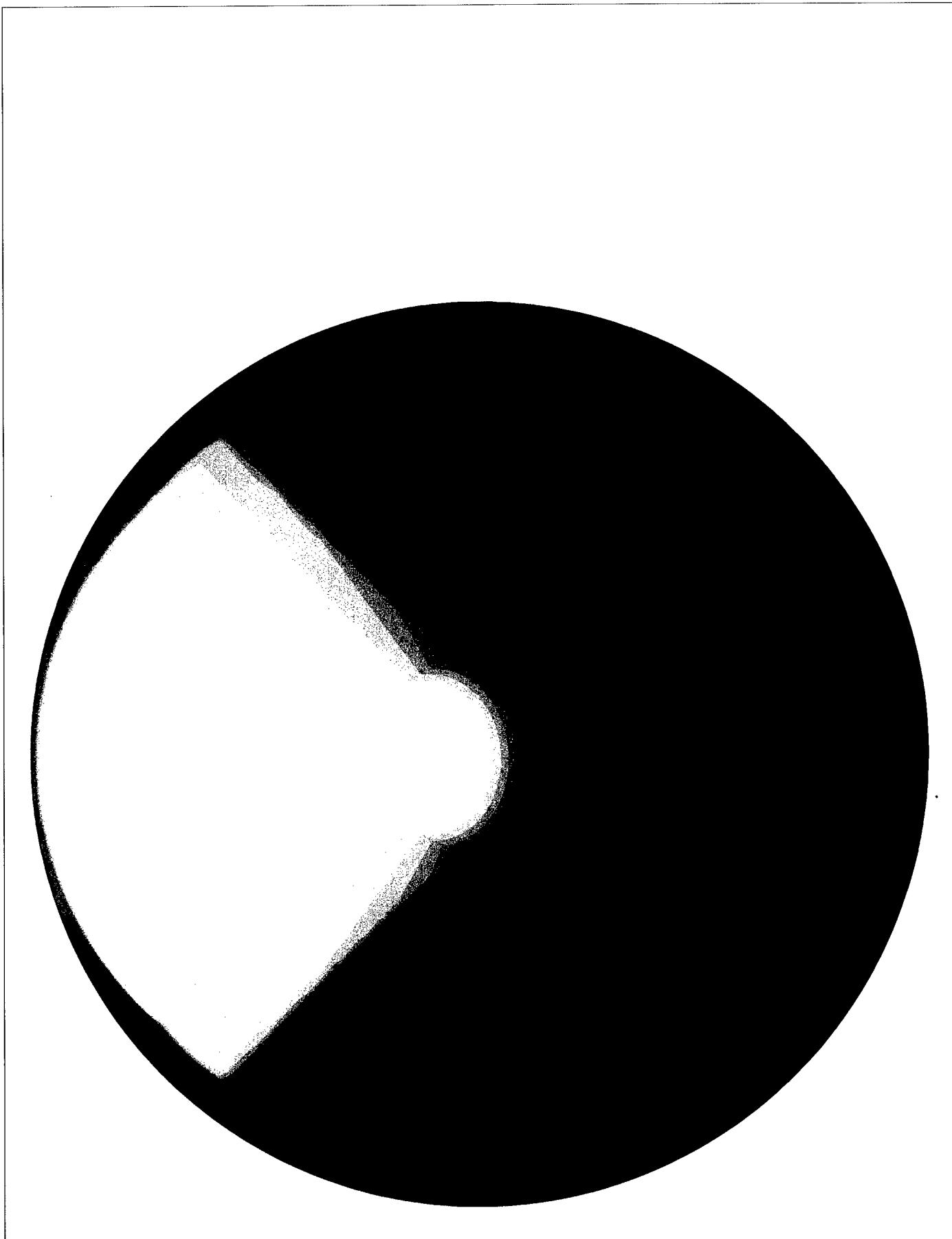
Figure 66. Front View of 3D Geometry
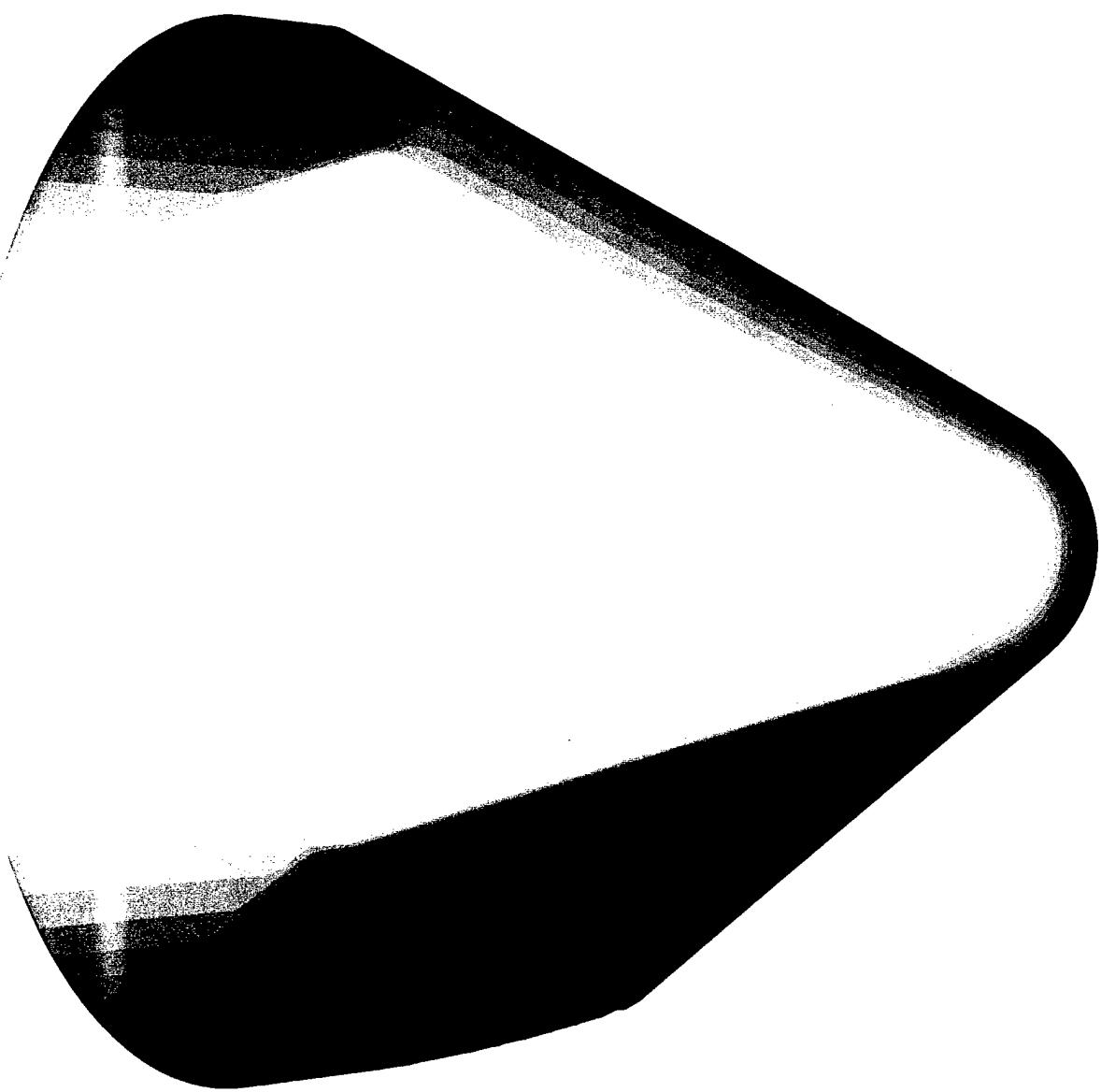
Figure 67. Side View of the 3D Geometry

Figure 68. Window View of 3D Geometry
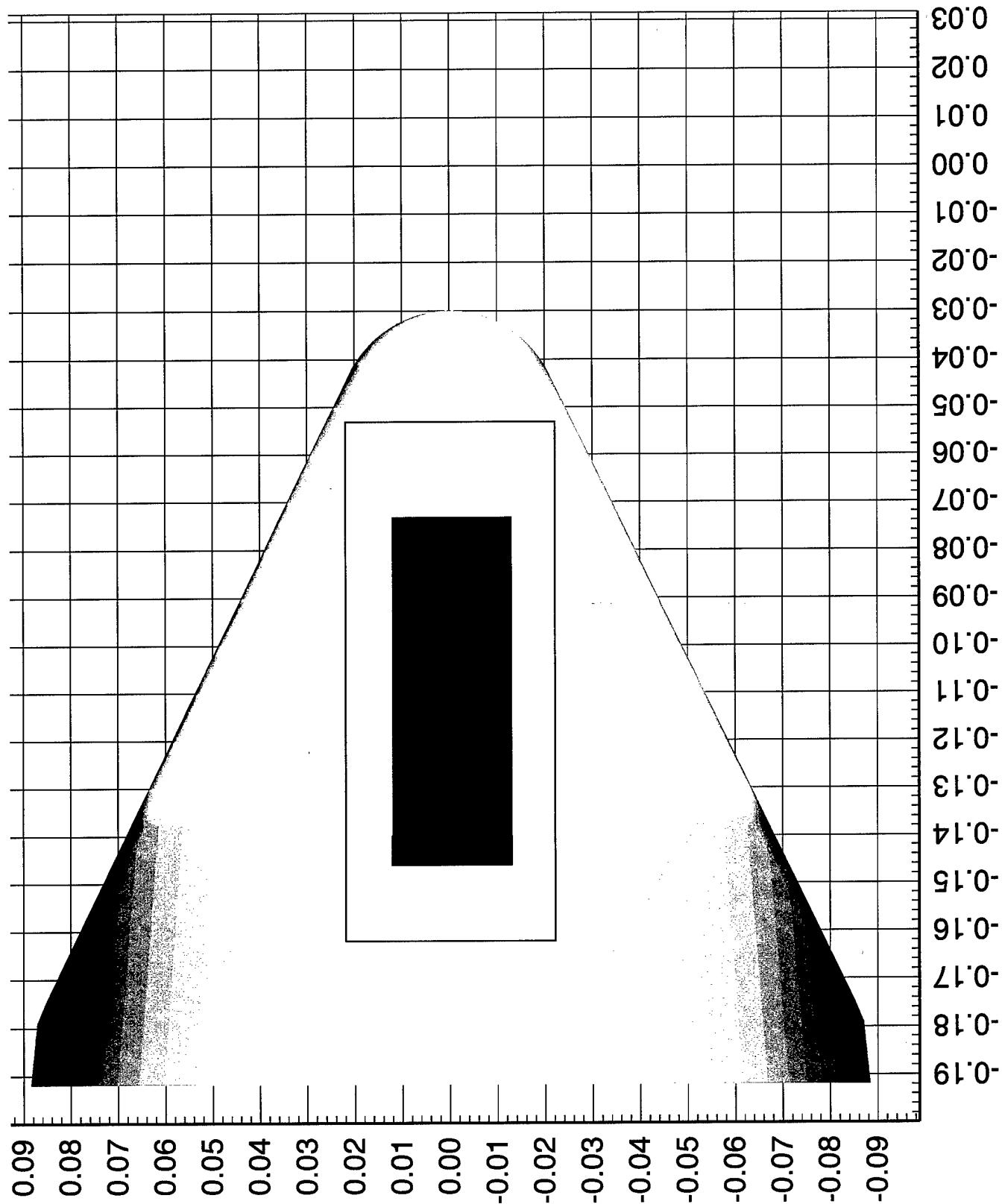
leads to instability in three-dimensional boundary layers near leading edges or on bodies at angle of attack. The code was developed for laminar flow control applications and can be used to study the compressible, three-dimensional boundary-layer stability characteristics. It was used in this manner for the current effort.

The nominal flow conditions for the interceptor are summarized below:

- Altitude 20 km
- Mach Number 15
- Wall Temperature 300 K

Mean flow calculations have been performed for both the sharp wedge with a deflection angle of 26 deg and the seeker head geometry.

The temperature profile shown in Figure 62 reveals the thin boundary layer characteristics. It was important to examine the idealized wedge flow case since the more complex three-dimensional geometry has a wedge-like character on each of the four seeker head facets as shown previously in Figure 64.

The complete three-dimensional problem is fairly complex. Sufficient effort was expended to idealize the geometry and provide an adequate representation of the seeker head shape. A blunt triconic body with a modified biconic window-plane configuration seemed to match the photograph of the interceptor quite well. The modified base and window plane geometry are shown in Figure 65. This window plane contour is very close to the contour that results when a blunted cone is intersected by a plane.

A window view of the geometry is also of interest as shown in Figure 68. The dark area is the actual window area whereas the other rectangular boundary is the neighboring structure region around the window.

The cross-sectional shape employed in the computer calculations is shown in Figure 69. This shape closely resembles the window view provided in the previous figure.

The next few figures reveal the flow over the surface of the seeker head in a region away from the window location. In Figure 70, note the nose region and the three triconic sections as one moves out from the apex of this quadrant view. The velocity accelerates to values in excess of 4.1 km/s. Furthermore there is significant cross-stream behavior near the body geometry discontinuities as shown in Figure 71.

Boundary-layer profiles in the middle of the window region are shown in Figures 72 to 74. The profiles identified as 80 are near the beginning of the window region, and the profile identified as 115 is near the end of the window region in the downstream direction. The primary downstream velocity is W which is shown in Figure 72. The cross stream velocity profiles given in Figure 40 have an inflection point and change considerably as one proceeds downstream. The corresponding temperature profiles are shown in Figure 74. The influence of the geometry is
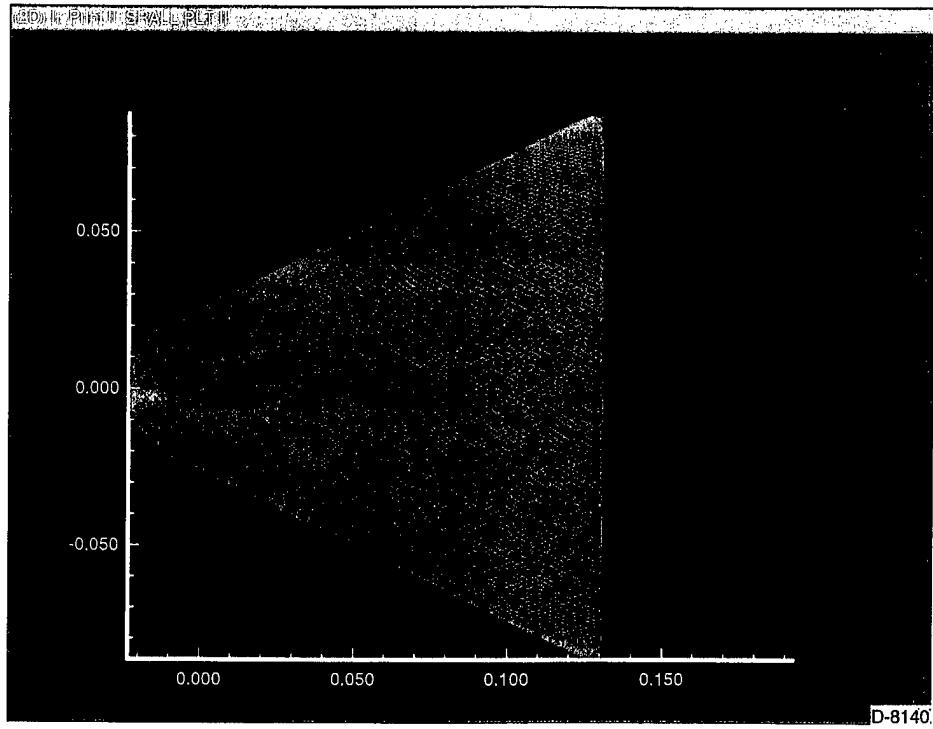
Figure 69. Computer-Generated Contour
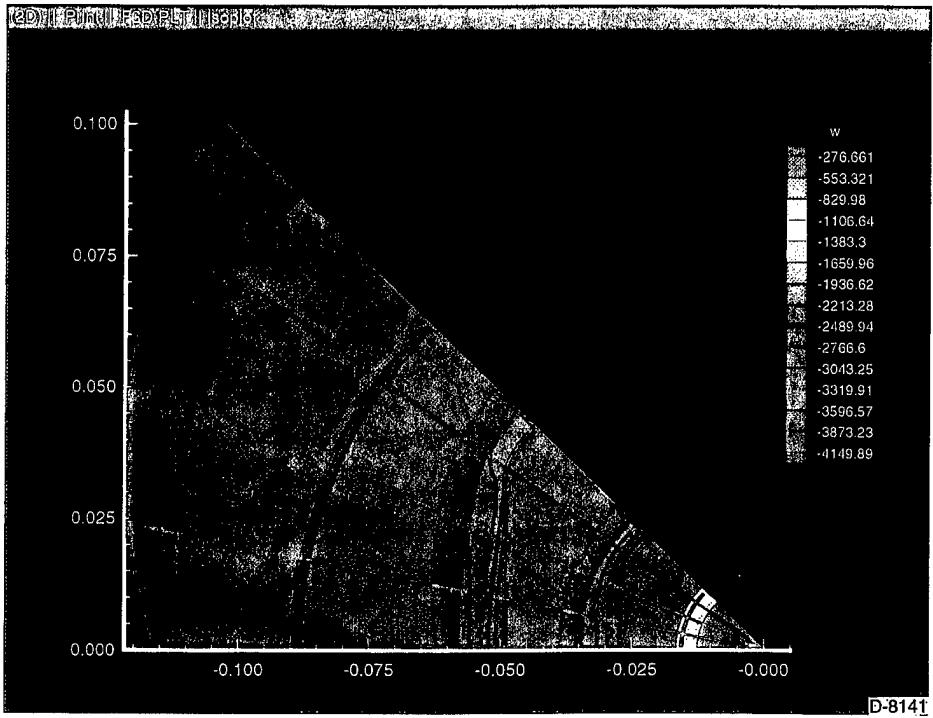
Figure 70. Main Stream Velocity Contour for 3D Flow

61
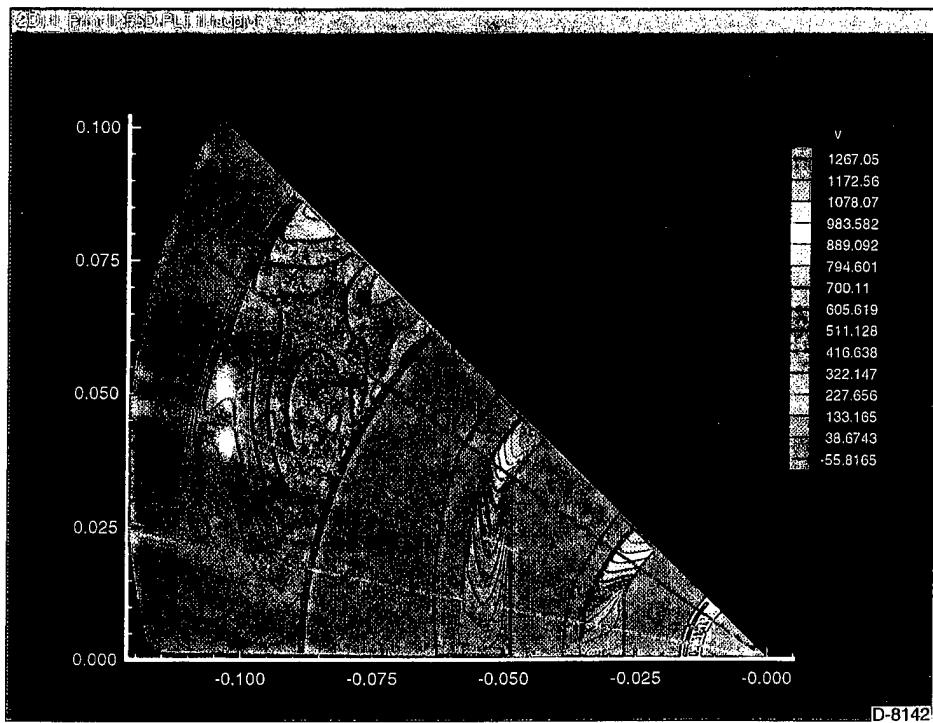
Figure 71. Cross-Stream Velocity Contours
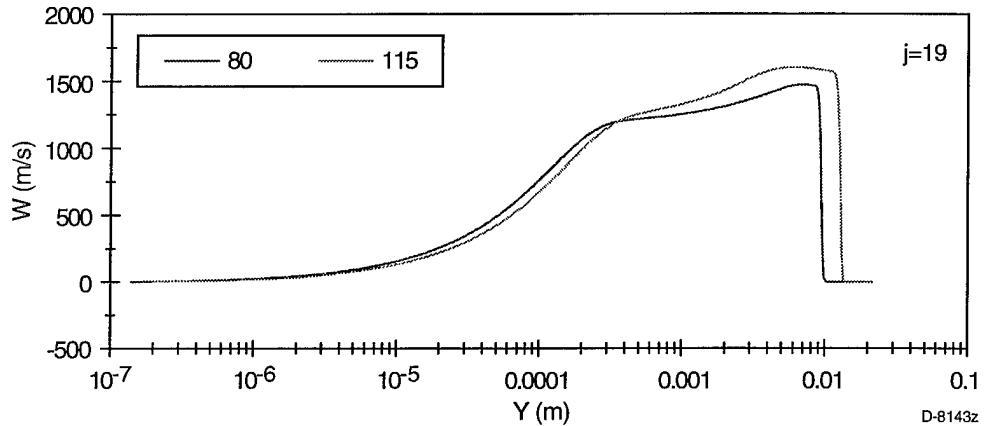
Figure 72. Main Stream Velocity Component

considerable in this case with temperature as high as 6000 K in the boundary layer. Note how well the wall condition of 300 K is achieved.

The stability characteristics of this mean flow was investigated by examining the flow over the window. The search for instability was initiated at the I=80 location and marched downstream until the end of the flowfield at I=126. Although the flowfield is changing significantly along the window in the downstream direction, no instability was found. The
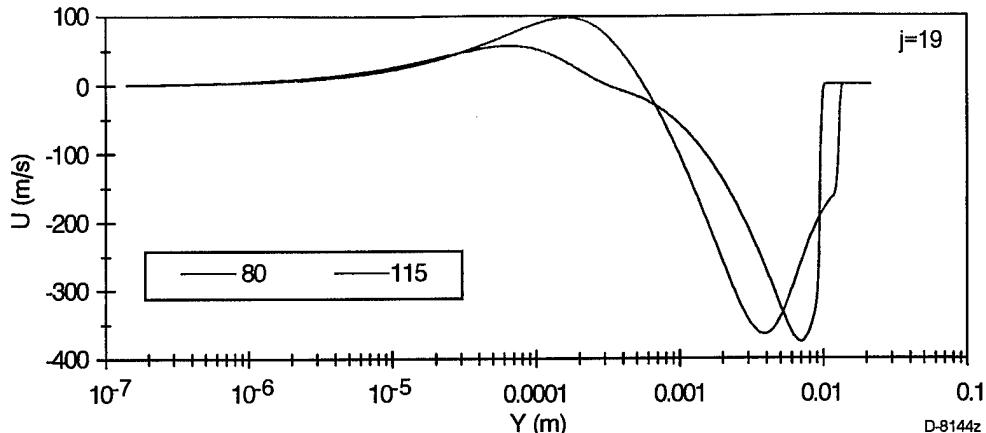
Figure 73.   Cross-Stream Velocity Component
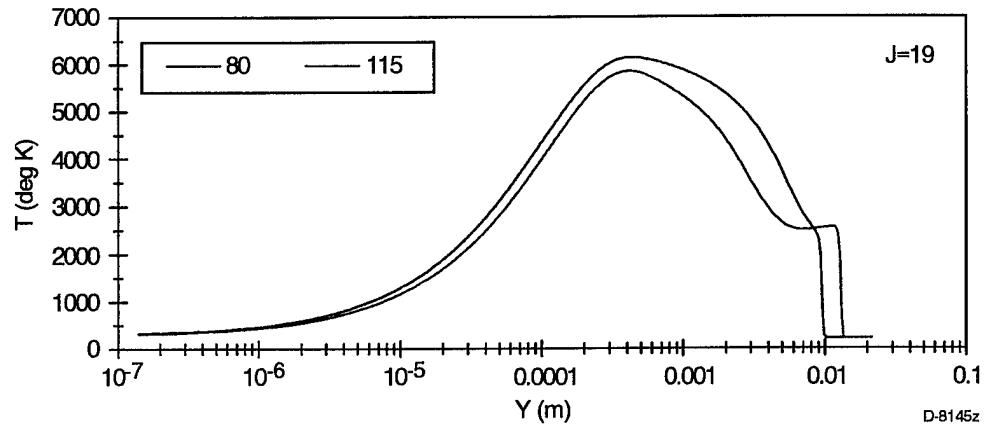
Figure 74. Temperature Profile

running conditions at the various "I" stations are summarized in Table 4 from the output of eMalik3d and it was continually noted that no instability was found. This result is entirely consistent with the results obtained by Johnson and Candler using a different stability approach.[23]

The wedge-like part of the window flow on the three-dimensional seeker begins at about I=99 and continues until about I=117. The nearly constant Mach number and temperature over this region is clearly evident.

Additional calculations were done over other regions of the window, but no instability was observed at any location. The emphasis in future work will be aimed at perturbing the mean flow calculation and assessing the sensitivity of the results.

63

Table 4. Stability Results for Nominal Flow Conditions

I	Me	Te(K)	Instability (?)
80	1.83	5957	No
81	1.84	5940	No
82	1.84	5922	No
83	1.84	5918	No
84	1.85	5900	No
85	1.86	5880	No
86	1.87	5858	No
87	1.88	5816	No
88	1.91	5750	No
89	1.96	5625	No
90	2.03	5472	No
91	2.11	5283	No
92	2.69	4137	No
93	2.97	3683	No
94	3.60	2835	No
95	3.74	2685	No
96	3.81	2603	No
97	3.84	2573	No
98	3.87	2546	No
99	3.89	2522	No
100	3.88	2532	No
101	3.89	2513	No
102	3.89	2522	No
103	3.91	2506	No
104	3.90	2514	No
105	3.91	2501	No
106	3.90	2508	No
107	3.90	2514	No
108	3.89	2520	No
109	3.89	2526	No
110	3.88	2532	No
111	3.88	2536	No
112	3.87	2540	No
113	3.87	2542	No
114	3.87	2544	No
115	3.87	2546	No
116	3.86	2548	No
117	3.86	2551	No
118	3.84	2580	No
119	3.60	2843	No
120	2.42	4644	No
121	2.50	4391	No
122	2.69	4025	No
123	2.85	3764	No
124	3.07	3441	No
125	3.29	3152	No
126	3.43	2969	No

3.6   Validation Experiment at LENS

It is recommended that the seeker head boundary-layer control due to cooling be experimentally verified in a ground test facility. The most appropriate ground test facility would be the Large Energy National Shock (LENS) Tunnel facility located at the Calspan-University of Buffalo Research Center, Buffalo, NY. Lens provides a unique combination of very large Mach number/Reynolds number simulation capability as shown in Figure 75 where the relevant national facilities are compared.
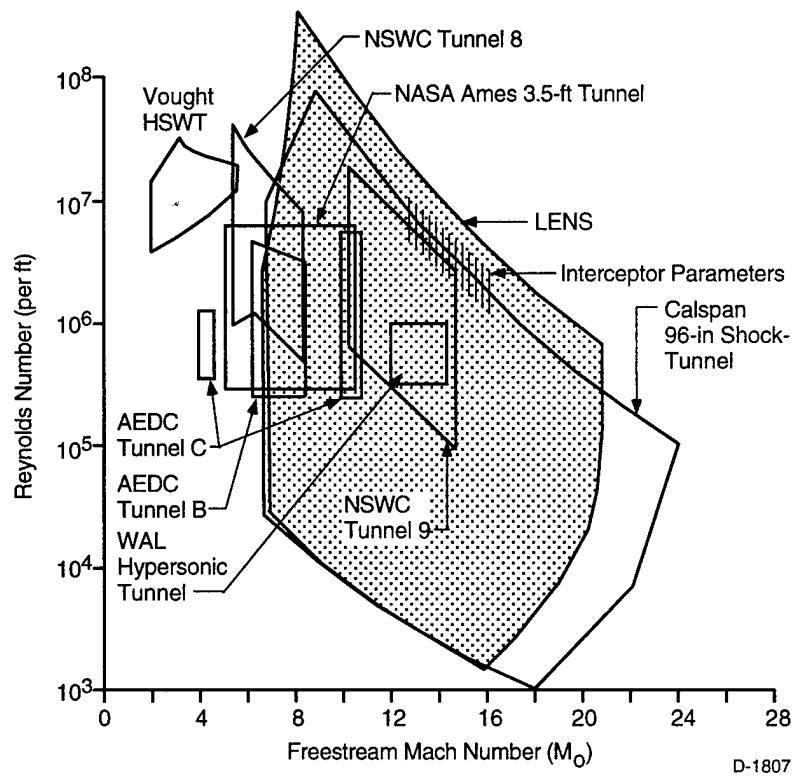
Figure 75. LENS Simulation Capability

LENS obviously has the highest Mach number capability (up to 18) and the highest Reynolds number (exceeding 100 million per ft). The approximate interceptor parameters are shown as vertical hashed lines in the figure. The measurement diagnostics suite at LENS is very extensive as outlined in Table 5 and would be very appropriate to measure boundary-layer transition behavior or the lack thereof. The heat transfer gauges would be the primary transition sensors, but the e-beam temperature technique would also be appropriate. The benefit of a flow-controlled boundary could also be assessed using the extensive aero-optics diagnostics that are also indicated in the table.

65

Table 5. LENS Instrumentation

Surface/Flowfield	Aero-Optics

Heat Transfer
    Thin Film
    Calorimeter
    Co-Axial
 	
Pressure
    Piezoelectric
    Strain Gage
 	
Free Stream
    Pitot Pressure
    Total Temperature
    Thin-Film
 	
Non-Intrusive
    Interferometry (density)
    e-beam (density, temperature)
    Laser-induced Fluorescence (species)
    Absorption Spectroscopy (species)
	Optical Bench
	
	Light Sources
	    Ruby Laser
	    HeNe Laser
	    Blackbody Source
	    Collimated Beam
	
	Refractive Sensors
	    IR Focal Plane Array
	    Visible
	
	Radiative Sensors
	    MWIR Emission
	    1.5 to 5 micron Spectrometer

3.7   Comments on High Speed Boundary-Layer Transition

The calculations presented above revealed that wall heating in concert with some geometry modifications lead to stabilizaton of the boundary layer. This control of transition to turbulence is based upon techniques that have been known to the fluid dynamics community for many years. Recent activities undertaken at the University of Minnesota by Prof. Candler and his students, Heath Johnson and Trevor Seipp, may lead to new ways to influence the stability of hypersonic boundary layers. They have shown that chemical reactions have a direct influence on boundary-layer stability and have confirmed experimental data taken by Prof. Hornung and co-workers at Caltech on three different test gas flows: nitrogen, carbon dioxide and air.

These results should be exploited for hypersonic vehicle flow control. One can envision circumstances where one would want to delay transition in order to reduce heating rates, minimize aero-optics effects and reduce boundary-layer radiation. Such beneficial behavior could be attained by seeding the boundary-layer flow with appropriate molecules leading to the required chemical reactions. It may even be possible to embed effective seed molecules directly into the ablative heatshields or thermal protection systems in order to generate the desired transition effect. At this stage of the research it is difficult to assess how robust *chemical boundary-transition control* could potentially be.

These techniques could also be employed to promote earlier boundary-layer transition. In reentry physics applications it is sometimes necessary to increase heating by forcing boundary layer transition to occur earlier in the flight for signature control purposes. A molecule in a heatshield could provide this effect in a more benign way than tripping the boundary layer flow with protuberances or fences.

Chemical boundary-layer transition control could impact the current emphasis on high speed interceptor at very low altitudes. These become very high Reynolds number, high enthalpy flows with extremely high heating rates. Reductions in aerothermal effects on seeker windows are essential in order to design viable systems. In order to evaluate whether chemical boundary-layer transition control could be a valuable resource for such applications, it is recommended that a combined theoretical and experimental program be developed. Theoretical CFD calculations would first be designed to find appropriate chemical reactions that impact transition. This would be followed by transition experiments that would be designed to implement the chemistry. A seeded heatshield is probably the easiest way to introduce the required molecules, but other techniques would also be explored. Boundary-layer transition delay and tripping would be studied.

4. SUMMARY

The theoretical analysis and design studies of passively cooled windows have revealed a potentially novel solution for interceptor seeker windows that is _passive_ and provides low window temperatures. Calculations of window thermal response have shown that acceptable window cooling is attained at aerodynamic heat fluxes up to 200 W/cm^2 and it is anticipated that much higher fluxes can be accommodated with proper design of hydride/bed material thermal conductivity. A feasible optical design using optical ports was also assessed.

The primary emphasis of future work must be the experimental demonstration of the cooling capacity of transition metal hydrides when subject to representative aerodynamic heating loads. Such experimental activities would be performed in several phases.

In the first phase, the hydride/thermal conductor mixture would synthesized and characterized, hydrogen production would be monitored, and the bed thermal response would be measured under moderate heating environments. The initial bed mixtures would consist of mixtures of $LaNi_5H_6$ and thin copper filaments to increase the bed thermal conductivity. More advanced thermal conductivity materials such as carbon fibers would also be used. Thermal performance calculations would also be performed in order to evaluate the measured response of the bed material to thermal loads, as well as to model the performance characteristics of optical windows.

The second phase would emphasize fabrication, characterization, and testing of the window concept when subject to high heating loads representative of the aerothermal environment. The operation of the window would be evaluated in a thermal facility where the bed material can be exposed to a range of heat flux levels simulating the interceptor aerodynamic environment. Two arc-jet facilities (H2 Facility at AEDC in Tullahoma, TN and the 60 MW Facility at NASA-Ames in CA) and the laser facility (Laser Hardened Evaluation Material Laboratory at Wright-Patterson AFB in OH) would be considered for these experiments which primarily test the cooling capacity of the window rather than simulating the hypersonic aerodynamic environment. Based upon these evaluations, optimum window designs and plans for a complete validation test including "optical seeing" through the window flowfield at the LENS facility in Buffalo, NY would also be developed.

We demonstrated that high-speed laminar boundary layers on typical three-dimensional seeker head geometries are stabilized by extreme wall cooling. The laminar flowfield over the wedge-like geometry for an advanced interceptor traveling at 5 km/s was employed in a three-dimensional stability code in order to calculate the propensity for the flow to undergo transition to turbulence. This boundary layer control is made possible by utilizing the Physical Sciences Inc. (PSI) passive window cooling technique which provides a relatively cold wall boundary condition over time a typical 5 to 10 s interceptor engagement time. These results are consistent with stabilization found by Candler and Johnson using a different stability model. The sensitivity of these results to changes in wall temperature and wedge angle are currently being investigated. In addition to these theoretical calculations, the practical details of performing experiments to demonstrate this stabilization have been examined. This includes a review of previous

successful cold wall experiments as well as the definition of potential experiments in the LENS facility at Calspan U. Buffalo Research Center. Experiments at LENS would be most appropriate since full-scale seeker head models could be employed.

It is recommended that hypersonic boundary-layer stabilization be pursued in two other directions. One would be the continued definition of a demonstration experiment in the LENS facility. This would involve specification of wall cooling techniques using artificial means initially, and then, perhaps, PSI's passive hydride scheme. It would also involve pre-test predictions of the experimental configuration. The flexibility to perform aero-optics measurements, in addition to fluid dynamic assessments, in the LENS facility allows for an immediate assessment of boundary-control benefits.

The second area involves very high-speed interceptor technology at low altitudes for boost-phase applications. This is an emerging area of interest that places extreme conditions on the interceptor seeker problem due to the turbulent, high-heating environment. Modeling studies would be performed to design interceptors (geometry, window configuration, heatshield) that satisfy low weight and seeker requirements. Passive cooling, flow control and advanced TPS materials would be considered.

5. LIST OF PUBLICATIONS AND TECHNICAL REPORTS

5.1   Personnel

The individuals who participated in this research effort include Mr. George Caledonia, Drs. Alan Gelb, Hartmut Legner, and David Rosen, and Mr. Les Popper.

5.2   Reports and Publications

a)   Appendix A manuscript to be submitted to J. Thermophysics and Heat Transfer.

b)   A.H. Gelb, H.H. Legner, and G.E. Caledonia, "High Velocity Interceptor Investigations," PSI TR-1426, December 1995.

c)   A. Gelb, H. Legner, D. Rosen, and G. Caledonia, "High Velocity Interceptor Investigations," PSI TR-1458, December 1996.

d)   H. Legner and G. Caledonia, "High Velocity Interceptor Investigations, PSI TR-1545, March 1998.

e)   D.P. Karipides, I.D. Boyd, and G.E. Caledonia, "Development of a Monte Carlo Overlay Method with Application to Spacecraft Glow," AIAA-96-1847, 31st AIAA Thermophysics Conf., June 17-20, 1996, New Orleans, L.A. Published *J. Thermophys and Heat Transfer*, 12/1, 30-37 (1998).

f)   D.P. Karipides, I.D. Boyd, and G.E. Caledonia, "Detailed Simulation of Surface Chemistry Leading to Spacecraft Glow," AIAA-98-2848, 7th AIAA/ASME Joint Thermophysics and Heat Transfer Conf., June 15-18, 1998, Albuquerque, NM.

6. REFERENCES

1. Libowitz, G.G., Electrochem. Soc. Proc. Vol. 92-5, 3 (1992).

2. Jemni, A., and Hasrallah, S. Ben, "Study of Two-Dimensional Heat and Mass Transfer During Desorption in a Metal-Hydrogen Reactor," *Int. J. Hydrogen Energy* **20**, 881 1995).

3. Werner, J., and Shui, V., "Optical Seeker Window Technology Program," Final Technical Report for Contract No. DASG60-91-C-065, prepared for U.S. Army Strategic Defense Command by Loral Infrared and Imaging systems, Inc., September 1992.

4. Endo/Exo Interceptor for Navy Theater Missile Defense, McDonnell Douglas Aerospace Brochure MC 6970.1 4-95.

5. Gelb, A.H., Legner, H.H., and Caledonia, G.E., "High Velocity Interceptor Investigations," Annual Report, December 1995, Physical Sciences Inc., PSI-1239/TR-1426.

6. Gelb, A.H., Legner, H.H., Rosen, D.I., and Caledonia, G.E., "High Velocity Interceptor Investigations," Interim Progress Report, December 1996, Physical Sciences Inc., PSI-1239/TR-1458.

7. Gelb, A., Legner, H.H., and Caledonia, G.E., "Cooled Imaging Window," PSI Proposal to U.S. Army Research Office, February 1996.

8. Caledonia, G.E., "Passively Cooled Window Investigations," PSI Proposal to U.S. Army Research Office, May 1997.

9. Configurations for the Atmospheric Interceptor Technology Program were described in two marketing documents distributed at the AIAA/BMDO Technology Readiness Conference. One summarized the BMDO Program and the other highlighted the McDonnell Douglas Aerospace activities (MC 6970.1 4-95).

10. Loral Infrared and Imaging Systems, Inc., "Optical Seeker/Window Technology Program," Final Technical Report, September 1992.

11. Malik, M.R., "Prediction and Control of Transition in Supersonic and Hypersonic Boundary Layers," AIAA J., Vol 27, No.11, November 1989, 1487.

12. Mack, L.M., "Boundary Layer Stability Theory," Rept 900-277 Rev A, November 1969, Jet Propulsion Lab., Pasadena, CA.

13. Stetson, K.F., "Comments on Hypersonic Boundary-Layer Transition," Flight Dynamics Laboratory, Wright Research and Development Center, WRDC-TR-90-3057, September 1990.

14. Mack, L.M., "Linear Stability Theory and the Problem of Supersonic Boundary Layer Transition," AIAA J., Vol. 13, No.3, March 1975.

15. Potter, J.L., "Review of the Influence of Cooled Walls on Boundary-Layer Transition," AIAA J., Vol 18, No. 8, August 1980.

16. Ames Research Staff, "Equations, Tables and Charts for Compressible Flow," NACA Report 1135, 1953.

17. Lianos, D., "Hypervelocity Interceptor Technology Testbed (HITT) Program," , Proceedings of the Forum on Interceptor Aerothermochemistry, Huntsville, AL, 25-26 Sept 1997.

18. Candler, G.V. is currently studying the influence of chemistry effects on boundary-layer transition. This activity is closely related to our research program.

19. Johnson, H.B. and Candler, G.V., provided CFD calculations for the sharp wedge and the three-dimensional seeker-head geometry, June 1996.

20 Candler, G.V., Wright, M.J., and McDonald, J.D., "A Data Parallel LU relaxation Method for Reacting Flows," *AIAA J.*, Vol. 32, No. 12, pp. 2380-2386, December 1994.

21. Wright, M.J, Candler, G.V., and Prampolini, M., "Data Parallel Lower-Upper Relaxation Method for Navier-Stokes Equations," *AIAA J.*, Vol. 34, No. 7, pp. 1371-1377, July 1996.

22. Malik, M.R., "eMalik3d: An e^N code for Three-Dimensional Flow over Finite-Swept Wings," High Technology Report No. HTC-9502 (version 2), April 1995.

23. Johnson, H. And Candler, G.V., "Transition to Turbulence in TMD Interceptor Flows," presented at the Forum on Interceptor Aerothermochemistry, 25-26 September 1997, University of Alabama in Huntsville, Huntsville, AL.

24. Candler, G.V., Private communication on boundary-layer transition estimates, April 1996.

APPENDIX

<u>Passive Cooled Optical Windows</u>

PASSIVE COOLED OPTICAL WINDOWS

Alan H. Gelb,[*] Harmut H. Legner,[†] Leslie A. Popper,[‡] and George E. Caledonia[¤]

Physical Sciences Inc.

ABSTRACT

A novel concept for passively cooling hypersonic missile windows is presented which utilizes the heat of desorption of hydrogen from metal hydrides to balance aerodynamic heating. Model calculations indicate windows can be maintained near room temperature for 10 s at 200 W/cm^2 heating.

INTRODUCTION

High velocity vehicles operating at low altitudes between 20 and 40 km will experience severe aerodynamic heating. This heating will affect optical sensing and tracking operations. A variety of techniques involving window design and gas injection have been developed to minimize window heating. Active technologies such as gas injection can be cumbersome due to

---

[*]Principal Research Scientist, Physical Sciences Inc., 20 New England Business Center, Andover, MA 01810-1077

[†]Principal Research Scientist, Physical Sciences Inc., 20 New England Business Center, Andover, MA 01810-107, Associate Fellow, AIAA

[‡]Principal Research Scientist, Physical Sciences Inc., 20 New England Business Center, Andover, MA 01810-1077

[¤]President, Physical Sciences Inc., 20 New England Business Center, Andover, MA 01810-1077, Associate Fellow, AIAA

the need to carry gas cylinders and auxiliary flow control equipment. A passive window cooling technique is presented here which uses the heat of decomposition of a highly endothermic reaction to balance the aerodynamic heat flow.

A schematic of the passive window cooling concept is presented in Figure 1. The optical window is constructed from optical ports embedded in a container filled with a transition metal hydride. The optical ports extend through the container and provide optical access to sensors within the vehicle. The optical ports can either contain fiber optics leading to the sensors or can be empty. Window temperature control is achieved by the balance of aerodynamic heat flow with heat absorption from the release of hydrogen from the transition metal hydride.

Transition metal hydrides are a wide variety of compounds characterized by their ability to absorb and desorb hydrogen reversibly. The discussion here will focus on one such compound, $LaNi_5H_x$. The thermodynamics and kinetics of the hydrogen absorption/desorption reactions have been well characterized. Most significant of the properties of $LaNi_5H_x$ is that it is a high-energy, low-temperature ablator, 15.5 kJ/gm H_2. Its equilibrium vapor pressure is high at low temperatures, p ~ 3 atm at 300 K, so that the heat absorption by hydrogen desorption can maintain the window at low temperatures. The desorbed hydrogen flow required to balance an aerodynamic heating of 100 W/cm^2 is 6.46×10^{-3} gm H_2/cm^2. This amount of hydrogen can be readily vented downstream or injected into the boundary layer of the window.

In this paper we present model calculations of the thermal response of hydride window bed heated between 100 and 200 W/cm^2. The results demonstrate the feasibility of maintaining an optical window at room temperature by passive cooling. Issues involving sensor operation and image formation are deferred to future work.

THERMOCHEMISTRY OF LaNi₅Hₓ

We discuss briefly the relevant properties of $LaNi_5H_x$. General discussion of transition metal hydrides is presented in References 1 and 2.

$LaNi_5$ reacts with hydrogen to form a non-stoichiometric hydride according to the reaction

$$LaNi_5 + \frac{x}{2} H_2 \rightleftharpoons LaNi_5H_x \quad . \tag{1}$$

The maximum value of x is 6, i.e., the hydrogen saturated compound is $LaNi_5H_6$. The reaction is reversible. The equilibrium vapor pressure of hydrogen $LaNi_5H_x$ is shown in Figure 2. The equilibrium vapor pressure is accurately described by the following empirical expression:[3]

$$p_{H_2} = \exp\left(-\Delta H/RT + \Delta S/R\right)$$

where R is the universal gas constant, T is the absolute temperature and ΔH and ΔS are empirical parameters equal to 30.1 kJ/mol and -108 J/mol. The hydrogen vapor pressure is relatively independent of the amount of absorbed hydrogen. This behavior is displayed in Figure 3 where the hydrogen vapor pressure above $LaNi_5H_x$ is shown for varying values of x at several temperatures. The significance of this behavior is that the hydrogen desorption rate will be a function of temperature and independent of the amount of hydrogen in the hydride.

The kinetics of hydrogen desorption have been measured and fit by Mayer et al.[4] to an empirical equation. Their expression for the hydrogen mass desorption rate $\dot{m}$ is:

$$\dot{m} = C_d \exp\left(\frac{E_d}{RT}\right) \frac{P_e - P_{eq}}{P_{eq}} \rho_s \tag{2}$$

where C_d and E_d are empirical constants equal to 16.473 kJ/mol and 9.57 s^{-1}, respectively, P_e is the ambient hydrogen pressure, P_{eq} is the equilibrium hydrogen pressure of LaNi$_5$H$_x$, and ρ_s is the hydride bed density.

A critical factor in the operation of the hydride bed is the ability to transfer heat into the bed. Upon heating, hydrogen will be depleted from portions of the bed. Heat balance and temperature will depend on the rate of heat of transfer into undepleted portions of the hydride bed. LaNi$_5$H$_x$ is synthesized as a powder and has low thermal conductivity. Jemni et al.[5] choose a value of 0.012 W/cm K for a LaNi$_5$H$_x$ bed thermal conductivity in their simulations of heat and mass transfer. For this conductivity the thermal diffusion penetration depth in 10 s, a typical vehicle engagement time, is equal to 0.35 cm. To balance a heating rate of 100 W/cm^2, hydrogen must be desorbed to a depth of 0.78 cm. Without modification the hydride bed would be rendered ineffective due to rapid temperature rise in hydrogen depleted areas. This difficulty is resolved by blending the LaNi$_5$H$_x$ with high conductivity materials such as copper (3.94 W/cm K) or K-1100 graphite fiber from Amoco Performance Products Inc. (11 W/cm K). These materials must be added in a long fiber form with the LaNi$_5$H$_x$ powder uniformly dispersed between the fibers to produce high thermal conductivity in the bed.

The addition of thermal conducting additive to the hydride bed involves a tradeoff between the bed capacity and thermal conductivity. Bed dilution decreases the bed heat absorption capacity and increases the required thermal penetration depth. Only 50/50 mixtures of LaNi$_5$H$_x$/additive will be considered here. Future work will address bed formulation optimization.

AERODYNAMIC HEATING RANGES

The application of this cooled window concept is to optical sensing and tracking from hypersonic vehicles in the endoatmosphere. An estimate of the magnitude of aerodynamic heating such as vehicles will experience is appropriate. Figure 4 shows aerodynamic heat loads as a function of altitude for vehicle velocities between 3 and 5 km/s for a window placed at the vehicle surface.

The values shown in Figure 4 were generated using a generic turbulent the heating rate obtained in Reference 6 for 25 km altitude and 4 km/s velocity and scaling it by density and velocity-cubed to obtain heating rates at other conditions. Although this procedure is approximate, the results are representative of anticipated heating rates. The heating rates are very high, several hundred of W/cm^2, at low altitude where turbulent flow occurs. At 3 km/s the heating rate is below 200 W/cm^2 over the 20 to 40 km range. At 25 km and 4 km/s, the conditions examined in Reference 6, the heating rate is about 200 W/cm^2. A reasonable estimate is that these are the most stressing conditions for optical sensing anticipated for engagement scenarios. An appropriate range of heating rates is thus 100 to 200 W/cm^2.

MODEL SIMULATIONS

Calculations were performed using the PSI composite materials thermal response code to simulate the thermal response of a finite thickness hydride bed heated on one surface. The code simulates the thermal response of a multicomponent system with one ablating species and heat transfer by conduction and ablation. Simulations were performed for heating rates of 100 and 200 W/cm^2 over 10 to 20 s time intervals. All calculations were one-dimensional with the hydride bed having infinite lateral extent. Hence edge effects due to finite bed effects are not

79

accounted for. The hydride bed was modeled as a continuous structure without viewing ports as shown in Figure 1. Although simplified, this model is instructive in that its predicted response to thermal loads provides a demonstration of the feasibility of passive window cooling using metal hydrides.

The simulations were performed in the following fashion. At t < 0, the hydride bed was assumed to be at room temperature in equilibrium with hydrogen. At t = 0, the bed container was opened and a heat flux of 100 or 200 W/cm² was applied to the surface. Calculations were performed for different values of ambient pressures between 0 and 1 atm. The computed temperature profiles were totally insensitive to the choice of ambient pressure and subsequent calculations were performed at p_e = 0.1 atm in Eq. (2). Two bed compositions were considered: 50/50 mixture of $LaNi_5H_x$/Cu and 50/50 $LaNi_5H_x$/K-1100 graphite fiber. The respective bed thermal conductivities were taken to be 1.97 and 5.0 W/cm K.

RESULTS

The thermal response of a $LaNi_5H_x$/Cu bed heated at 100 W/cm² is shown in Figure 5. The simulation assumes that the bed is initially at 300 K in equilibrium with hydrogen. At t = 0, the bed is opened to the ambient at 0.1 atm pressure and heating of the bed surface commences. The bed temperature is controlled by two opposing factors. When the bed is opened to the ambient, hydrogen is released to balance the hydrogen pressure with that of the ambient. This causes the bed temperature to fall to a value where hydrogen desorption ceases. Opposing this is the heat flux to the surface which tends to increase the surface temeprature. For a heating rate of 100 W/cm², the cooling of the heat bed by hydrogen desorption dominates the temperature variation. At the bed surface, the temperature drops from 300 K at t = 0 to about 260 K where it

80

remains until t = 5 s. The initial rise above 300 K at t = 0 is a numerical artifact. Beyond t = 5 s, the surface temperature slowly rises reaching 285 K at t = 10 s. At 0.5 cm below the bed surface, the temperature drops to about 240 K after 5 s and rises to about 260 K after 10 s. Deeper in the bed, the temperature drops to about 220 K, a value low enough so that hydrogen desorption is shut off.

For comparison, the thermal response of reference material with equal thermal conductivity to 100 W/cm^2 heating is shown in Figure 6. The calculations were performed for a 10 cm thick material. The surface temperature rises rapidly, reaching 540 K after 10 s heating. The cooling effect of the hydride bed is clearly shown by comparison of Figures 5 and 6.

The thermal response of a hydride subjected to 200 W/cm^2 heating is shown in Figure 7. These calculations were performed for a 6 cm thick hydride bed. The bed temperature drops initially and the surface reaches a minimum value after 1.5 s. Beyond 1.5 s the surface temperature increases almost linearly reaching 470 K after 10 s. At 0.5 cm below the surface, a minimum temperature of 260 K occurs after 2 s. At later times the temperature increases linearly reaching 420 K after 10 s. The thermal wave does not reach to the bottom of the bed and the thermal response at 6 cm depths is similar to the in-depth response of the 100 W/cm^2 case.

The computed surface temperature rise in Figure 6 is due to the rate of heat transfer into the hydride bed. As the bed is heated, hydride near the surface is depleted and the bed temperature rises. To access virgin bed, heat must be transferred further into the bed. At high heating rates, the surface temperature is controlled by the bed thermal conductivity. This is illustrated in Figure 8 where the thermal response to 200 W/cm^2 heating of a LaNi$_5$H$_x$/K-1100 graphite fiber bed with k = 5 W/cm K is shown. In this case the bed surface temperature remains below 300 K for 5 s of heating. The behavior is qualitatively similar to the case shown in

81

Figure 7. However, as the surface region is depleted the temperature rise is much less steep and the surface temperature remains below 350 K after 10 s.

In summary, these calculations demonstrate that passive cooling using mixtures of transition metal hydrides and high thermal conductors can maintain optical windows at or below 300 K under realistic heating conditions. The critical materials parameter is the thermal coductivity of the hydride bed.

SUMMARY AND CONCLUSIONS

A concept for passively cooled optical windows has been presented. This concept utilizes the high heat of desorption of hydrogen from metal hydrides to cool. The metal hydrides have the unique property of being low temperature, high energy ablators. This property allows the maintenance of windows near room temperature under high heating conditions.

Calculations were presented for the thermal response of hydride beds subjected to realistic endoatmospheric heating between 100 and 200 W/cm^2. Beds formulated with mixtures of $LaNi_5H_x$ and Cu with k = 1.97 W/cm K maintained surface temperatures below 300 K for heating periods of 10 s. $LaNi_5H_x$/K-1100 graphite fiber beds maintained surface temperature below 300 K for 5 s and below 350 K for 10 s for 200 W/cm^2 heating. These calculations demonstrate that hydride beds can cool optical windows on endoatmospheric hypervelocity vehicles.

ACKNOWLEDGMENT

REFERENCES

1. Libowitz, G.G., *J. Phys. Chem. Solids*, Vol. 55, 1994, p. 1461.

2. Dantzer, P., "Metal Hydride Technology: A Critical Review," in *Topics in Applied Physics*, edited by Wipf, Vol. 73, Springer Verlag, Berlin, 1997.

3. Van Mal, H.H., "Stability of Ternary Hydrides and Some Applications," *Phillips Research Reports Supplements*, Vol. 1, 1978.

4. Mayer, U., Groll, M., and Supper, W., *J. Less-Common Metals*, Vol. 131, 1987, p. 235.

5. Jemni, A. and Nasrallah, S. Ben, *Int. J. Hydrogen Energy*, Vol. 20, 1995, p. 881.

6. Loral Infrared and Imaging Systems, Inc., "Optical Seeker/Window Technology Program," Final Technical Report, Sept. 1992.

FIGURES

1. Schematic of passive window cooling concept.

2. Equilibrium hydrogen pressure above $LaNi_5H_x$ as a function of temperature.

3. Pressure-composition isotherms at 40, 60, 100, 120, and 140°C for $LaNi_5H_x$ (from

    Reference 3).

4. Heating rate, $\dot{q}$, versus altitude, H, for several vehicle velocities. Vechicle nose radius is

    0.2 in. and cone angle is 15 deg.

5. Thermal response of $LaNi_5H_6$/Cu to 100 W/cm^2 heating: k = 1.97 W/cm K, bed

    thickness = 4 cm.

6. Thermal response of a non-pyrolyzing material to 100 W/cm^2 heating. Thermal

    conductivity is 1.97 W/cm K.

7. Thermal response of $LaNi_5H_6$/Cu bed to 200 W/cm2 heating: k = 1.97 W/cm K, bed

    thickness = 6 cm.

8. Thermal response of LaNi5H6/K-1100 graphite fiber bed to 200 W/cm2 heating:

    k = 5.0 W/cm K, bed thickness = 10 cm.

84

ΔH from
Atmospheric Heating

H₂ Release into
Boundary Layer

Window Containing
Bed of Transition Metal
Hydride and Thermal
Conductor

D-0710

Optical Ports *

Gelb

85

Figure 1

Figure axis labels: → H_2 Pressure (atm), → Hydrogen Concentration (at. H/mole LaNi$_5$)

140°C

120

100

60

40

LaNi$_5$

D-9792

Gelb
Figure 3

D-1301

Gelb
Figure 4

Temperature (K)

400
375
350
325
300
275
250
225
200
175
150

Surface
0.5 cm
1 cm
1.5 cm
2 cm
3 cm

0   1   2   3   4   5   6   7   8   9   10

Time (s)

D-3186

Gelb
Figure 5

D-1437

Gelb
Figure 6

Gelb
Figure 7

D-9794